Memristive magnetic memory for spintronic synapses

Marco Mansueto

▶ **To cite this version:**

Marco Mansueto. Memristive magnetic memory for spintronic synapses. Micro and nanotechnologies/Microelectronics. Université Grenoble Alpes [2020-..], 2020. English. NNT : 2020GRALT082 . tel-03236443

HAL Id: tel-03236443
https://theses.hal.science/tel-03236443

Submitted on 26 May 2021

HAL is a multi-disciplinary open access archive for the deposit and dissemination of scientific research documents, whether they are published or not. The documents may come from teaching and research institutions in France or abroad, or from public or private research centers.

L'archive ouverte pluridisciplinaire **HAL**, est destinée au dépôt et à la diffusion de documents scientifiques de niveau recherche, publiés ou non, émanant des établissements d'enseignement et de recherche français ou étrangers, des laboratoires publics ou privés.

Université Grenoble Alpes

THÈSE

Pour obtenir le grade de

DOCTEUR DE L'UNIVERSITÉ GRENOBLE ALPES

Spécialité : NANO ELECTRONIQUE ET NANO TECHNOLOGIES

Arrêté ministériel : 25 mai 2016

Présentée par

Marco MANSUETO

Thèse dirigée par **Bernard DIENY,**
IGR, CEA - Spintec
et
codirigée par **Liliana BUDA-PREJBEANU,**
Enseignante chercheuse, Grenoble INP

préparée au sein du **Laboratoire Spintronique et Technologie des Composants**

dans **l'École Doctorale Electronique, Electrotechnique, Automatique, Traitement du Signal (EEATS)**

Mémoire magnétique memristive pour synapses spintroniques

Memristive magnetic memory for spintronic synapses

Thèse soutenue publiquement le **17 / 12 / 2020**,
devant le jury composé de :

Monsieur Ahmad BSIESY
Professeur, Grenoble INP, Président de jury

Madame Alina M. DEAC
Directrice de recherche, Helmholtz-Zentrum Dresden-Rossendorf, Rapportrice

Madame Julie GROLLIER
Directrice de recherche, Unité Mixte de Physique CNRS-Thales, Rapportrice

Monsieur Dafiné RAVELOSONA
Directeur de recherche, CNRS, C2N, Examinateur

Abstract

In the context of a technological era in which the amount of data is exponentially increasing, the development of brain-inspired softwares allows a fast and smart management of information. However, the massive parallelization of neurons interconnected through synapses, emulated by these approaches, leads to a drastic power consumption when runned on conventional computers. From this, it arises the need of dedicated hardwares that, contrarily to the Von Neumann architecture, interconnect at large scale processing units and memory units as, respectively, neurons and synapses. For this reason, the realization of nano-sized devices able to mimic the functionalities of neurons and synapses represents the main challenge for the integration of large scale neuromorphic chips. The purpose of this work is to realize memristive devices, i.e. non-volatile multilevel memories that play the role of synapses, exploiting the advantages of the MRAM technology. In this thesis two main concepts have been proposed, realized and characterized.

The first device investigated in this thesis is based on the conductance variation of an in-plane magnetized magnetic tunnel junction as function of the relative direction of the magnetizations of the storage and reference layers. Being able to stabilize intermediate resistance states between the minimum and maximum resistance values of the magnetic tunnel junction requires the realization of a medium able to stabilize its magnetization along different in-plane directions. We obtain such isotropic properties using a ferromagnet/antiferromagnet/ferromagnet structure in which the antiferromagnetic layer thickness is chosen low enough to not provide any exchange bias but rather enhanced coercivity. We integrated this composite layer in an in-plane magnetic tunnel junction and, after a nano-patterning process, we retrieved the same property of isotropic coercivity. The device is able to monotonously increase or decrease its resistance in response to positive or negative voltage pulses (in ns range) because of the spin transfer torque coming from an additional out-of-plane polarizer. We demonstrate the stabilization of at least 21 resistance levels in devices of 100nm of diameter. We also model the device with a macrospin code implementing the Landau Lifshitz Gilbert equation with an additional dissipative term analog to a dry friction term in the Newton's law. With this, we retrieve all the results obtained experimentally with quite good agreement.

The second concept investigated in this work is based on a perpendicularly magnetized tunnel junction whose free layer presents a granular structure similar to the one used for recording media. The realization of such layer led to the realization of grains with a diameter around 3nm and, therefore, paramagnetic at room temperature. Such layer is integrated in magnetic tunnel junctions with diameters between 100nm and 300nm. The electrical measurements performed at 150K demonstrate that a very large number of resistance states can be achieved with a gradual field-driven switching of such grains. Moreover, the use of voltage pulses confirms that the spin transfer effect can be exploited for the probabilistic reversal of the grains magnetization.

Résumé

Dans le contexte d'une ère technologique où la quantité de données augmente de façon exponentielle, le développement de logiciels inspirés du fonctionnement du cerveau permet une gestion rapide et intelligente de l'information. Cependant, la parallélisation massive de neurones interconnectés via des synapses, émulée par ces approches, conduit à une consommation d'énergie drastique lorsqu'ils sont exécutés sur des ordinateurs conventionnels. De là, naît le besoin de matériels dédiés qui, contrairement à l'architecture de Von Neumann, permettent d'interconnecter à grande échelle des unités de traitement et des unités de mémoire représentant respectivement les neurones et les synapses. Pour cette raison, la réalisation de dispositifs de taille nanométrique capables de mimer les fonctionnalités des neurones et des synapses représente le principal défi pour l'intégration de puces neuromorphiques à grande échelle. Le but de ce travail est de réaliser des dispositifs memristifs, c'est-à-dire des mémoires multiniveaux non volatiles qui jouent le rôle de synapses, exploitant les avantages de la technologie MRAM. Deux concepts de memristor spintronique à base de jonctions tunnel magnétiques ont été proposés, réalisés et caractérisés.

Le premier concept fonde ses principes de fonctionnement sur la variation de conductance d'une jonction tunnel magnétique aimantée dans le plan, en fonction de la direction relative des aimantations des couches de stockage et de référence. La clé de ce concept repose sur la mise au point d'un matériau magnétique capable de stabiliser son aimantation selon différentes directions dans le plan menant ainsi à une multitude d'états de résistance intermédiaires. On obtient de telles propriétés isotropes en utilisant une structure ferromagnet / antiferromagnet / ferromagnet dans laquelle l'épaisseur de la couche antiferromagnétique est choisie suffisamment faible pour ne pas conduire à l'existence d'une anisotropie d'échange mais plutôt d'une coercivité accrue. Nous avons intégré cette couche composite dans une jonction tunnel magnétique dans le plan et, après un processus de nanostructuration, nous avons conservé la même propriété de coercivité isotrope. Dans une telle jonction tunnel, on peut augmenter ou diminuer de manière monotone la résistance en réponse à des impulsions de tension positives ou négatives (dans la gamme ns) grâce au couple de transfert de spin provenant d'un polariseur suuplémentaire aimanté hors plan. Nous démontrons la stabilisation d'au moins 21 niveaux de résistance dans des jonctions tunnel de taille latérale de 100nm. Nous modélisons également le fonctionnement du dispositif avec un code macrospin implémentant l'équation de Landau Lifshitz Gilbert avec un terme dissipatif supplémentaire analogue à un terme de frottement solide dans la loi de Newton. Par ces simultations, nous interprétons tous les résultats obtenus expérimentalement avec un bon accord.

Le deuxième concept étudié dans ce travail est basé sur une jonction tunnel aimantée perpendiculairement dont la couche libre présente une structure granulaire similaire à celle utilisée pour les supports d'enregistrement magnétique. La réalisation d'une telle couche a conduit à la formation de grains d'un diamètre d'environ 3nm et donc paramagnétiques à température ambiante. De telles couches ont été déposées et intégrées dans des jonctions tunnel de taille latérale de 100nm à 300nm. Les mesures électriques effectuées à 150K démontrent qu'un très grand nombre d'états de résistance peut être obtenu avec une commutation graduelle par champ de ces grains. De plus, l'utilisation d'impulsions de tension confirme que l'effet de transfert de spin peut être exploité pour l'inversion probabiliste de l'aimantation des grains.

Table of Contents

List of Figures

List of Tables

List of Abbreviations

AF	Antiferromagnet(ic)
AI	Artificial intelligence
AL	Analyzer layer
AL	Anisotropic magnetoresistance
ANN	Artificial neural network
CIP	Current in plane
DOS	Density of states
DW	Domain wall
FL	Free layer
FM	Ferromagnet(ic)
FMR	Ferromagnetic resonance
GMR	Giant magnetoresistance
IBE	Ion beam etching
LLG	Landau-Lifshitz-Gilbert
MOKE	Magneto-optical Kerr effect
MRAM	Magnetic random access memory
MTJ	Magnetic tunnel junction
OPP	Out-of-plane precession
PCM	Phase change memory
PHE	Planar Hall effect
PMR	Perpendicular magnetic recording
POL	Perpendicular polarizer
RIE	Reactive ion etching
RKKY	Ruderman-Kittel-Kasuya-Yosida
RRAM	Resistive random access memory
RT	Room temperature
SAF	Synthetic antiferromagnet(ic)
SEM	Scanning electron microscopy
SHE	Spin Hall effect
SOT	Spin-orbit torque
STT	Spin-transfer torque
TMR	Tunnel magnetoresistance
VLSI	Very large scale integration
VSM	Vibrating sample magnetometry

List of Symbols

A	Exchange constant	J m^{-1}
e	Electron charge	$1.6 \times 10^{-19} As(C)$
$\boldsymbol{f}$	Force	kg m s^{-2} (N)
$\boldsymbol{H}$	Magnetic field	A m^{-1}
$\boldsymbol{H_{eff}}$	Effective field	A m^{-1}
J	Current density	A m^{-2}
K_{eff}	Effective anisotropy constant	J m^{-3}
K_u	Uniaxial anisotropy constant	J m^{-3}
$\boldsymbol{m}$	Reduced magnetisation vector	
M_s	Saturation magnetisation	A m^{-1}
N	Demagnetizing tensor	
t_X	Thickness of material X	m
$\boldsymbol{T}$	Torque	s^{-1}
α_G	Gilbert damping	
β	Dry friction parameter	rad s^{-1}
γ	Gyromagnetic ratio	Hz T^{-1}
$\hbar$	Plank constant	$1.05457 \times 10^{-34} Js$
μ_0	Vacuum magnetic permeability	Chosen equal to $4\pi \times 10^{-7}$ T A^{-1} m

Introduction

The need of storing information led, along the centuries, to the creation of more and more advanced media depending on the quality and the quantity of the data. The advent of writing, the first book, the magnetic tape and the first Hard Disk Drive (HDD) are all signs of an evolution of the knowledge always linked to the human needs along its history. Since half of the 20^{th} century, we are living one of the biggest ever technological revolutions: the information age. In fact, the advent of the digital electronics, associated with the development of the Metal-Oxide-Semiconductor Field Effect Transistor (MOSFET), marked the beginning of an increadible race towards the miniaturisation of this technology with the aim of increasing the storage density. In 1965, the Moore's law predicted the doubling of the number of transistors in an integrated circuit every two years [1]. In parallel to this, the digitalization of the knowledge and, overall, the advent of Internet, provided an exponentially increasing amount of data that, according to Data Age 2025 [2] [3], is not expected to stop. In the next five years, the size of the Global Datasphere is expected to reach 175 ZB (10^{21} bytes) (much larger than the one estimated in 2018 around 33 ZB) as shown in Fig. I a.

Linked to this, the need of a faster and smarter way of extrapolating usefull information out of such massive amount of data led to the development of brain-inspired algorithms. In fact, since the ability of the brain of performing very complex tasks in a relatively short time comes from the complex parallelization of the computation (where each of the 10^{11} neuron has around 7000 synapses), the implementation of algorithms with a similar structure begun. These systems, such as Artificial Neural Networks (ANN), are characterized by a network of processing units (neurons) organized in layers and massively interconnected through memory units (synapses) (Fig. I b). In the simplest model, each neuron receives as input the sum of the signals coming from the previous layer of neurons, weighted by their corresponding synaptic weights and, after a processing step (that depends on the model used), it sends out a signal going towards the next layer of neurons. The impressive results were immediately evident from simple tasks, such as patterns recognition, to more complex ones such as the famous Alpha Go [4] [5]. The algorithm, developed by Google, was able to win the match of Go against the world champion with a final result of 4 to 1. Despite this, the final analysis, at the end of the match, revealed that the Google machine consumed around 1MW against the 20W of the human brain. In fact, this big difference is addressable to the computer architecture that is widely used in digital electronics theorized by Alan Turing and later developed by John Von Neumann. In this kind of architecture, the separation of the memory unit from the processing one creates an important transfer of information between the two units. At the beginning, the information processing represented the main limit in term of computational speed and power consumption. This stopped to be true few years ago, when the processing speed became larger than the memory access one. When this happens, the system undergoes the so called Von Neumann bottleneck. The strategies used to overcome the problem include the creation of a memory hierarchy where different technologies are exploited in order to be more or less frequently accessed (as the classical hierarchy used in Central Processing Units CPUs). The other solution involves the parallelization of the computational tasks as, for example, in a Graphical Processing Unit (GPU). Despite the impressive computational power demonstrated by these systems, their Von Neumann nature does not actually solve the bottleneck issue. This becomes more and more obvious when very complex algorithms, such as ANN, are run over them. This kind of algorithm,that emulates the massive parallelized computation of the brain (where each of the 10^{11} neuron has around 7000 synapses), is clearly not adapted to an hardware whose main problem is the data transfer between

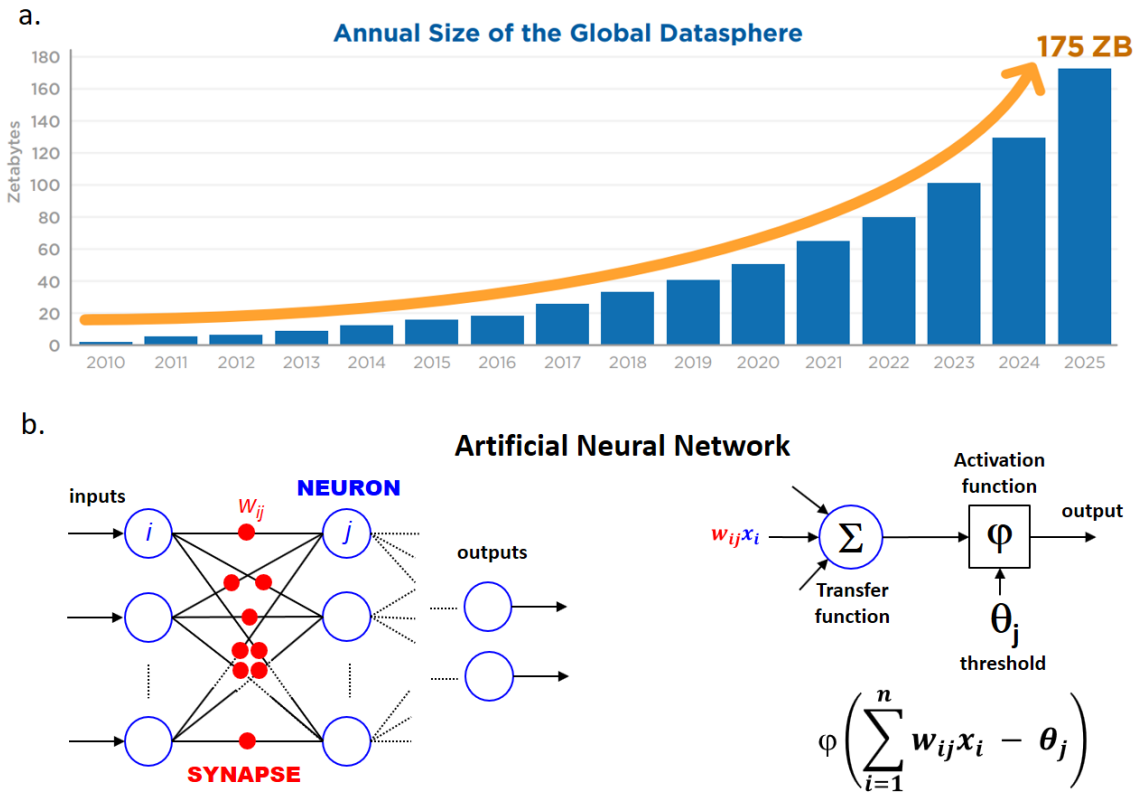

Fig. I | Global datashpere and ANN | a. Histogram of the Global Datasphere along the last decade and prediction for the next 5 years. **b.** Artificial Neural Network schematic and working principle.

the processing unit and the memory [6] [7].

In this sense, the creation of a dedicated hardware adapted to the functionalities of these algorithms and, therefore, brain-inspired too, is under the attention of the scientific community since several years. Some of the most famous attempts, such as SpiNNaker or TrueNorth, use still CMOS technology for Very Large Scale Integration (VLSI) systems. The SpiNNaker system [8] is based on 57600 VLSI chips with a very complex communication infrastructure between them. This allows to simulate very large neural models up to a billion of neurons with programmable connectivities and learning models. Despite the increadible flexibility, the Von Neumann architecture used in each of the core leads to some limitation as, for example, the reducing number of implementable elements due to their increasing complexity. In TrueNorth [9], instead, developed by IBM, a spiking neural network is implemented in a completely new architecture. It consists of 4096 cores of spiking neural networks. Each core has 256 "integrate and fire" neurons and 256×256 programmable synaptic connections. In this way, each neuron can communicate with a maximum of 256 other neurons. This is limiting if compared with the SpiNNaker but, the better spacial distribution of memory and processing units allows a very good tolerance to error (classical of the neural networks) and a reduced power consumption. Despite these promising advancements, the CMOS based technology used to implement such complex structure leads to a very large chip area ($4.3cm^2$) and poor density efficiency since, depending on the application, a part of the synaptic circuit is not used at all. In both cases, the dedicated hardware demonstrates the huge potentiality of the Artificial Intelligence (AI). Althought this, it is evident that the Von Neumann bottleneck is not fully overcome in none of the two solutions [10]. A complete solution would be a fully interconnected system where memory and data process coexist spacially in the same circuit. Indeed a real in-memory computing system, where the processing is localized where the data are stored, would be the suitable solution [11] [12]. Moreover, the use of new elements whose functionalities are closer to the neuron/synapse ones could lead to an important increase of the computational power and, at the same time, to a reduction of the energy consumption and of the areal density. In this context, memristive devices (analog or

multi level resistive memories) seem to well emulate the synaptic functionalities [13] [14]. The most promising ones are based on non-volatile emerging technologies such as resistive RAM (RRAM), phase change memory (PCM) and spin-transfer torque magnetic RAM (STT-MRAM) [15] [16]. The first ones are based on capacitor-like structure where the dielectric layer (usually an oxide as TiO_2, HfO_2, Ta_2O_5, etc.) can let the oxygen ions migrate under a relatively intense electric field. Depending on the material characteristics the resistance variation of the device can be more or less abrupt leading to a binary or analog switching. The memristive behavior can be achieved for relatively high applied voltages for which a relevant Joule heating occurs. This is believed to have a critical role in the switching dynamics but it represents also the main drawback since it affects significantly the endurance and the reliability of the device. In PCM, the property of chalcogenides, such as $Ge_2Sb_2Te_5$, of changing structure from crystalline to amorphous depending on the temperature is exploited to vary the final resistance. Also in this case, the memristive characteristic can be achieved through an accurate control of the applied pulses. Similarly to the RRAM, the SET/RESET current is relatively high. Moreover, the slow switching due to the relatively low temperature dynamics and the reliability issues do not make this device the best candidate for a memristor. Concerning the STT-MRAM technology, it has several advantages, such as high endurance and reliability, since the resistance variation does not imply any physical material transformation. Despite this, the binary nature of this technology does not allow a straightforward transition towards a memristive device [17] [18].

In this thesis the advantages of the MRAM technology have been exploited to obtain a multilevel memory device with high reliability, scalable and easily integrable. Such device is a key element for a very large scale integration in a chip like the ones described above in order to achive the increased computational power, the reduced energy consumption and areal density expected from a memristive circuit.

The aim of this thesis is, therefore, the investigation and the realization of novel and original concepts of spintronic memristor in order to realize compact single nano-pillar devices. The innovation relies in the integration of peculiar active magnetic layers in the magnetic tunnel junction stack. The material development is carried on through the deposition of full sheet film samples and their magnetic and electrical characterization. After multiple optimization steps, the patterning of arrays of nanodevices is done with a nanofabrication process developed in the Plateforme Technologique Amont (PTA) [19]. Finally, these devices are characterized with an electrical setup. In parallel, the magnetic properties of the devices are simulated numerically and through the development of a macrospin model for a better interpretation and understanding of the experimental results.

Outline This thesis is divided into four chapters, a conclusion chapter and an appendix. Lists for all figures, tables, symbols and abbreviations are provided. All links (figures, equations, chapter and section names, references) are clickable. The manuscript is organised as follows:

Chapter 1: Spintronics This chapter is meant to introduce the basic concepts used in spintronics. The main physical effects exploited in this thesis and, in general, in the MRAM technology are briefly described before a short overview on the advantages and disadvantages of this last. Those advantages have been exploited for the realization of memristive devices some of which will be shortly introduced. Finally, the analysis of pros and cons of those devices will lead to the description of the new concepts developed in this work.

Chapter 2: Experimental techniques: fabrication and characterization This chapter describes the experimental techniques used in this thesis. The standard procedure includes a deposition step followed by magnetic and electrical characterization at full sheet film level and a nano-fabrication process followed by magnetic and electrical characterization at device level. Each of the steps presented in this chapter is the result of an optimization.

Chapter 3: Memristor based on the angular variation of TMR In this chapter we propose a new concept of memristive device suitable for scalable and large scale integration applications. A full macrospin model describes the device functionalities and working regions thanks to an additional dissipative term in the LLG equation. The materials development section describes the challenges in the realization of the device and the final results are shown in the electrical characterizations section.

Chapter 4: Memristor based on a granular structure of the free layer In this chapter the working principles of a memristive device based on a granular free layer in an MTJ structure are described. The material development and the electrical results are detailed before a conclusive section.

Conclusions and perspectives The main results of this work are summarized and some ideas for the further investigations are described.

Appendix This chapter details the calculation steps to obtain the analytical results described in Chapter 3.

Chapter 1

Spintronics

Contents

This chapter is meant to introduce the basic concepts used in spintronics. The main physical effects exploited in this thesis and, in general, in the MRAM technology are briefly described before a short overview on the advantages and disadvantages of this last. Those advantages have been exploited for the realization of memristive devices some of which will be shortly introduced. Finally, the analysis of pros and cons of those devices will lead to the description of the concepts developed in this work.

1.1 Introduction to magnetism

The first reference to a magnetic material dates around 600 b.c., when the ancient Greeks noted the strange attraction force between lodestones and iron [19]. Several centuries later, in China, they were using the magnetic properties of lodestones first, and magnetized iron needle later, to improve their navigation skills through the use of a compass. In Europe, the first description of a compass arrived only in the 12^{th} century. Despite the wide use of those materials, the first documented studies date back to the 16^{th} century with William Gilbert that used first term "electricity" [20]. The firsts hints of electromagnetism came much later, at the beginning of the 19^{th} century, when Ørsted noted that an electric current passing through a wire generates a magnetic field and Ampère showed that two parallel wires feel an attractive or repulsive force depending on the relative direction of the electric current passing through them [21]. Few years later, Faraday was demonstrating and explaining the electromagnetic induction and Maxwell was giving a complete description of the classical electromagnetism in the famous set of equations [22].

The modern understanding of magnetism started at the end of the 19^{th} with the theory of Weiss based on the existence of an internal molecular field proportional to the magnetization given by the average of several micromagnets (Weiss domains) [23]. In the same period, Curie was experiencing the temperature dependence of the remanent magnetization that over a critical value (Curie temperature) becomes zero giving rise to a paramagnetic state.

The advent of quantum mechanics at the beginning of the 20^{th} century gave a better explanation to those phenomena with a description including the motion and interaction of electrons. In the quanto-mechanical framework, the electron dynamics can be described with a set of four eigenvalues of operators that commute with the Hamiltonian, usually called quantum numbers, for which the Schrödinger equation have a solution. The first three, the principal, the azimuthal and the magnetic quantum numbers describe respectively the energy level, the orbital angular momentum and the projection of this last along a specific axis. The last of those is called spin and describes the intrinsic angular momentum of the electron that, seen in a semi-classical picture, would correspond to the existence of a magnetic dipole. Since the electron angular momentum is quantized in $S = \pm\hbar/2$, also the magnetic moment results quantized in a quantity $\mu_S = -g_S\mu_B S/\hbar \approx \mu_B$, where g_S is the spin g-factor whose value is 2 and μ_B is called Bohr magneton.

At atomic level then, the sum of those momenta gives a total magnetic moment characteristic for each material. Following the Pauli's exclusion principle and the Hund's rules, the net magnetic moment is different from zero only in the case of electron shells partially filled. This means that the majority of the materials in the periodic table is supposed to be magnetic. This changes when passing from the isolated atom to the solid state.

At this level, by computing the density of states (DOS) of a material, it comes out that a shift in energy can occur between the band structure for spin up and spin down (referred to as $S = +\hbar/2$ and $S = -\hbar/2$) due to the presence of d-electrons close to the Fermi level (as described for example in the Stoner model [24], [25]). As shown in a simplified draw in Fig. 1.1a, the energy shift can create a big difference between the two spin populations only if the d-electrons band structure (much more concentrated in terms of energy since they are more localized than s-electrons) is across the Fermi level. For this reason the real magnetic materials are mainly the transition metals such as Fe, Co and Ni as well described by the Slater Pauling curve (similarly, this happens for the f-electrons in the lanthanides) [26]. An example of a real band structure for the two spin populations is shown in Fig. 1.1b for Co. The total magnetic moment can be computed by $\mu_{TOT} = (N_\uparrow - N_\downarrow)\mu_B$, where $N_{\uparrow(\downarrow)} = \int_0^{E_F} DOS_{\uparrow(\downarrow)}(E)\,\mathrm{d}E$.

A ferromagnet can be defined as a material with non-zero magnetic moment (meaning $N_\uparrow \neq N_\downarrow$) measured in A m^2. Its magnetization $\vec{M}$ is defined as the magnetic moment volume density and measured then in A m^{-1}. The maximum value that $|\vec{M}|$ can take is called spontaneous magnetization M_S and occur when the magnetic dipoles are perfectly aligned.

The model described in this section can be also useful to understand the transport-related phenomena. In fact, since in solid state metals the electrons actually playing a role in transport

are the ones close to the Fermi level (depending on the applied voltage), the important difference of DOS at Fermi level between the two spin populations (in red in Fig. 1.1) can be quantified by spin polarization

$$P = \frac{DOS_{\uparrow}(E_F) - DOS_{\downarrow}(E_F)}{DOS_{\uparrow}(E_F) + DOS_{\downarrow}(E_F)} \tag{1.1}$$

and it is at the basis of spin-dependent transport phenomena that will be described later in this chapter.

With those notions, a brief description of the magnetic energies that play a meaningful role in the description of the magnetic state of a ferromagnet is given in the next paragraphs in order to have a better understanding of the properties of the magnetic stacks presented in this work.

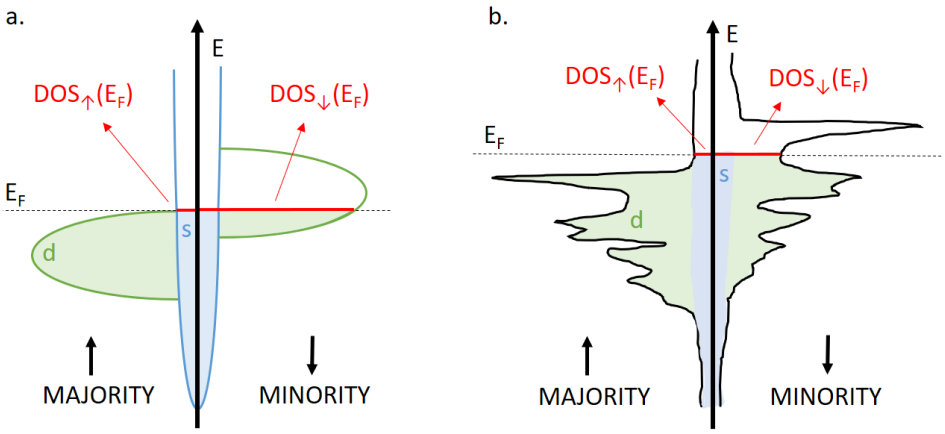

Fig. 1.1: Spin dependent DOS | **a.** Schematic of sd-bands electron model with spin dependent DOS for magnetic transition metal. **b.** Example of a realistic spin dependent DOS for Co [27].

1.1.1 Gibbs free energy

In the framework of micromagnetism, developed by Brown [28], a ferromagnetic material can be described by an ensemble of domains with uniform magnetization separated by domain walls in which the magnetization varies (concept developed by Weiss [23]). The magnetization can be defined as a continuous function with an amplitude M_S, dependent on temperature as described by Pierre Curie, and a unit vector dependent on space and time $\vec{m}(\vec{r},t)$ so that $\vec{M} = M_S(T)\vec{m}(\vec{r},t)$. For the description of the stable magnetic configuration of a certain body, it is necessary to know the Gibbs energy and find its minimum. To do this, a brief description of the various contributions to the total energy is briefly given in the next paragraphs.

1.1.1.1 Zeeman energy

The Zeeman effect, named after Pieter Zeeman, describes the tendency of a local magnetization $\vec{M}$ to align along an external field $\vec{H}_{ext}$ applied to it. The Zeeman energy can be written as a volume integral of this local effect as

$$E_{Zeeman} = -\mu_0 \int_V \vec{m} \cdot \vec{H}_{ext}\, \mathrm{d}V \tag{1.2}$$

where μ_0 is the vacuum magnetic permeability.

1.1.1.2 Exchange energy

Discovered by Heisenberg [29], the exchange interaction is a short-range quantum-mechanical effect that occurs between two indistinguishable particles according to exchange symmetry. In case of electrons in a solid, it originates from the Coulomb repulsion that is spin dependent according to

Pauli exclusion principle. In a localized magnetism model (mostly valid for rare earth materials), the associated Hamiltonian is given by

$$H_{ex} = -\sum_{i<j} J_{ij} \vec{s}_i \cdot \vec{s}_j \tag{1.3}$$

where J_{ij} is the exchange constant between two neighboring spins $\vec{s}_i$ and $\vec{s}_j$, summed over the nearest neighbors. The exchange constant sign determines whether the magnetic ordering is ferromagnetic or antiferromagnetic, for which two neighboring spins are respectively aligned or anti-aligned. The value of the exchange constant determines the quantity of energy that is needed to destroy the magnetic ordering that, in terms of temperature ($k_B T$), corresponds to the Curie temperature for a ferromagnetic material or to the Neel temperature for an antiferromagnetic one.

In the case of itinerant magnetism which is more appropriate to describe the magnetism of transition metals based compounds, the energy associated to the exchange energy can be defined as

$$E_{ex} = \int_V A_{ex}[(\nabla m_x)^2 + (\nabla m_y)^2 + (\nabla m_z)^2]\,\mathrm{d}V \tag{1.4}$$

where A_{ex}, the exchange stiffness, depends on material parameters such as lattice parameter and number of atoms per unit cell.

1.1.1.3 Demagnetizing energy

In a ferromagnetic material, the magnetic order, created by the exchange interaction, generates a magnetic field whose lines will close as described in the Gauss law. This field can interact with other magnetic objects including the ferromagnet itself.

In the case of an interaction with a second magnetic object, it can be defined as a dipolar field $\vec{H}_{dip}$ that acts on the magnetization of the other object exactly as described by the Zeeman formula 1.2.

In the other case, when the field interacts with the same ferromagnet that generates it, the field direction results to be opposite to the magnetization. In this way, while the exchange interaction tends to align the magnetization in a parallel way on a short range, the field created will tend to anti-align the magnetization on a longer range. The balance (energy minimization) between those two contributions yields the creation of magnetic domains with uniform magnetic configuration separated by domain walls in which the magnetization varies progressively in space. This field is usually called demagnetizing field $\vec{H}_{dem}$ since it tends to reduce the total magnetization. In a formal way, in uniformly magnetized bodies, the demagnetizing field constitutes a contribution to the effective field, existing inside the ferromagnet, whose amplitude and direction depends on the total magnetization and on the geometry of the ferromagnet itself. It is expressed in the formula

$$\vec{H}_{dem} = -\bar{N} \cdot \vec{M} \tag{1.5}$$

where $\bar{N}$ is called the demagnetizing tensor. This tensor depends on the geometry of the magnetic body and it has the form of a diagonal tensor whose elements N_{ii}, called the demagnetizing coefficients, follow the relations $0 < N_{ii} < 1$ and $N_{xx} + N_{yy} + N_{zz} = 1$. In the cases of simple geometries, those factors have exact analytical expressions as, for example, for an infinite thin film in the x-y plane ($N_{xx} = N_{yy} = 0$ and $N_{zz} = 1$) or for a sphere ($N_{xx} = N_{yy} = N_{zz} = 1/3$) [30], [31]. Finally, the demagnetizing energy is given by

$$E_{dem} = -\frac{1}{2}\mu_0 \int_V \vec{m} \cdot \vec{H}_{dem}\,\mathrm{d}V \tag{1.6}$$

1.1.1.4 Magnetocristalline anisotropy

In a crystalline ordered material, the distribution of charges around each nucleus creates a static electric field that interacts with the angular moment of the electrons. This coupling, generally named

spin-orbit, is at the origin of a spacial variation of the energy characterized by minima of energy along certain preferencial crystalline directions. These directions are called easy axes of magnetization. In this case, the magnetization tends to align along these crystalline axes. Correspondingly, the directions of highest energy are called hard axis. The energy landscape can have a single axis of minimum energy that is then called a uniaxial anisotropy. In the most common case of uniaxial anisotropy (e.g. hexagonal and tetragonal crystals) along a direction $\vec{u}$, the energy can be described as

$$E_{an} = \int_V K_u[1 - (\vec{u} \cdot \vec{m})^2] \, \mathrm{d}V \tag{1.7}$$

and it can be approximated to a second order expression as $E_{an} = K_u sin^2\theta$, where θ is the angle between $\vec{M}$ and $\vec{u}$. In some situations, even in the case of uniaxial anisotropy, higher order anisotropies must be taken into account, for instance, to describe a easy-cone anisotropy.

1.1.1.5 Interfacial anisotropy

Another kind of anisotropy, widely used nowadays, arises from the interface between a non magnetic material with high spin-orbit coupling and a ferromagnet. This anisotropy, predicted by Nèel [32], can have different origins, such as broken inversion symmetry at the interface, magnetostriction or orbital hybridization. In a large number of cases, it has an energy minimum in a direction perpendicular to the plane [33] [34] [35]. In these cases, this perpendicular magnetic anisotropy (PMA) is usually in competition with the shape anisotropy created by the demagnetizing field which is an easy-plane bulk anisotropy. As a result of this competition between perpendicular interfacial anisotropy and bulk easy plane anisotropy, for films thickness below a critical value, the surface anisotropy components prevails on the shape one so that the net effective anisotropy is out-of-plane. To take into account this contribution, it is possible to substitute to the K_u in eq. 1.7, a term that considers the two contributions

$$K_{eff} = K_u + \frac{K_S}{t} \tag{1.8}$$

where t is the thickness of the ferromagnetic layer.

This anisotropy has been found in different systems including metal/ferromagnet, such as Pt/Co or Au/Co [36] [37], and oxide/ferromagnet multilayers such as Fe/MgO [38] [39].

1.2 Spin-dependent transport phenomena

The theory describing the spin-dependent transport in ferromagnetic transition metals, suggested by Mott [40], considers a simple model for the electrical conductivity for the two spin populations that will be noted as $\uparrow$ for majority and $\downarrow$ for minority one. In a ferromagnetic material, the total electrical resistivity is expressed as

$$\rho_{TOT} = \frac{\rho_\uparrow \rho_\downarrow + \rho_{\uparrow\downarrow}(\rho_\uparrow + \rho_\downarrow)}{\rho_\uparrow + \rho_\downarrow + 4\rho_{\uparrow\downarrow}} \tag{1.9}$$

where $\rho_{\uparrow\downarrow}$ is the spin mixing resistivity describing the moment transfer between the two populations due to spin-flip scattering events. In the low temperature approximation, where $T << T_C$, this last term can be considered negligible giving the final expression of

$$\rho_{TOT} = \frac{\rho_\uparrow \rho_\downarrow}{\rho_\uparrow + \rho_\downarrow}. \tag{1.10}$$

In this case, the ferromagnetic material resistivity results as the parallel of the two spin population resistivity as described in the two current model (Fig. 1.2a).

According to the Drude-Sommerfeld model [41], the resistivity can be modeled as

$$\rho_{\uparrow(\downarrow)} = \frac{m_{\uparrow(\downarrow)}}{n_{\uparrow(\downarrow)} e^2 \tau_{\uparrow(\downarrow)}}. \tag{1.11}$$

where m, τ and n are respectively the effective mass, the relaxation time and the density of states at the Fermi level for majority (minority) spin population. Considering that the density of states at the Fermi level for a ferromagnetic material is different for majority and minority spin populations as explained in the previous section, it turns out that the resistivities are also different (in this case the $\rho_{\uparrow} < \rho_{\downarrow}$) (Fig. 1.2a). This is due to the fact that, at Fermi level, the s-electrons (conduction ones) have more probability to be scattered on d-electrons (localized). That means that in a ferromagnetic material uniformly magnetized, the majority spin electrons (the ones aligned with the magnetization) experience a number of scattering events lower than the minority ones as shown in Fig. 1.2b. The experimental results obtained later by Fert and Campbell on iron-based and nickel-based alloys demonstrated that the spin-dependent transport can be effectively described by this model [42], [43], [44].

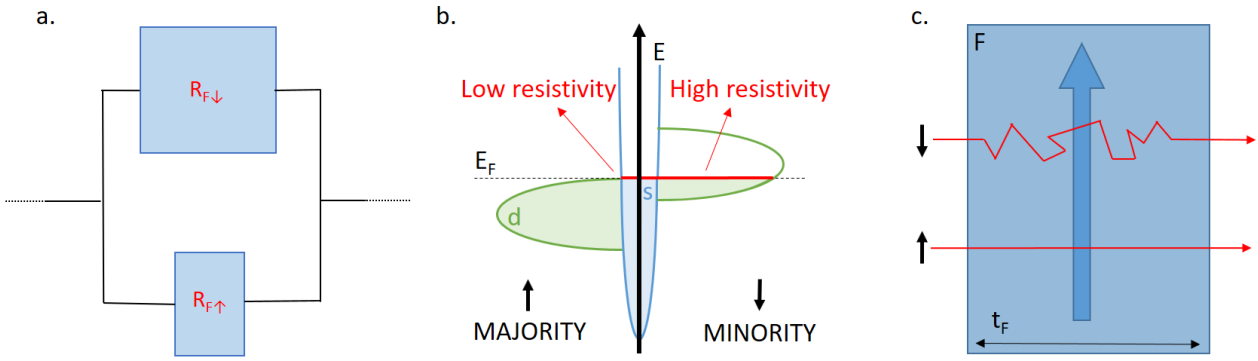

Fig. 1.2: Spin dependent transport | **a.** Resistance scheme in a two current model approach. $R_{F\uparrow(\downarrow)} = \rho_{\uparrow(\downarrow)} t/A$ where t and A are thickness and area of the ferromagnetic layer. **b.** Schematic of spin dependent DOS. **c.** Schematic of spin dependent transport for majority and minority spin populations.

This free electron model can be then used to easily describe and understand other phenomena related to the spin-dependent transport. One of those is the magnetoresistance effect associated to the variation of the resistance of a magnetic object dependently on the direction of the applied field with respect to the current direction. It was observed for the first time by Lord Kelvin in the far 1856 on Fe and Ni samples whose resistivities were varying as function of the direction of the current with respect to the magnetization. [45]. Later this effect was called anisotropic magnetoresistance (AMR) [46]. Other magnetoresistance effects known nowadays are the giant one (GMR), the tunneling one (TMR), the colossal one (CMR) [47] and the extraordinary one (EMR) [48] named from the smallest to the biggest. The AMR is a relatively small effect (a few % at RT), the CMR has not still being observed at room temperature and EMR is actually an AMR effect which is artificially enhanced by playing with the geometry of the samples and the position of the electrical contacts but does not really enhance the signal to noise ratio of the device. Therefore, the most used magnetoresistive effects in the spintronic community are GMR and TMR. In the next paragraphs, the two effects will be shortly described toghether with the spin transfer torque to give an overview of the reading and writing mechanisms used in spintronics and, in particular, in MRAM.

1.2.1 Giant magnetoresistance GMR

The giant magnetoresistance effect was discovered in 1988 independently by the groups of Albert Fert at University of Paris-Sud and Peter Grünberg in Forschungszentrum Jülich (both awarded the Nobel Prize in Physics in 2007) [49] [50]. Generally, considering a trilayer structure of two ferromagnets sandwiching a non-magnetic metallic spacer, the effect expresses the resistance variation of the sample depending on the relative orientation of the magnetization of the two magnetic layers. It is found that for antiparallel configuration of the magnetizations the resistance is higher than for

the parallel case. The effect is measured in percentage considering the formula

$$GMR = \frac{R_{AP} - R_P}{R_P} \times 100 \tag{1.12}$$

where R_{AP} and R_P are respectively the resistance measured in the antiparallel and parallel state. In the Fert experiment, the multilayer structure Fe(001)/Cr(001) grown by Molecular Beam Epitaxy (MBE) was used to perform resistance measurements at 4.2K where a GMR effect around 50% was found. In the case of Grünberg, a trilayer structure similar to the previous Fe(110)/Cr(110)/Fe(110) was measured at room temperature finding a GMR around 3%. Later in 1990 Parkin et al. demonstrated the existence of GMR effect also in multilayer structures deposited with sputtering techniques opening the doors to applications [51]. The experiments described up to now were performed in the so-called current in-plane geometry (CIP) but later it was found that in the current perpendicular to plane (CPP) configuration the GMR effect is larger.

A first description of the effect was done considering the two current model based on the free electron description of the spin dependent transport in ferromagnetic metals (1.2). Each spin population experiences the scattering events in the two ferromagnets and in the spacer as in Fig. 1.3. This can be described as a series of three resistances, two of which are spin-dependent as in eq. 1.11, for each spin channel. The two spin channel resistances are then put in parallel according to the two current model in eq. 1.10. The results are shown in Fig. 1.3 for the cases of parallel and antiparallel magnetization directions.

Considering a general case with a trilayer F1(t_{F1})/S(t_S)/F2(t_{F2}), in the parallel case it can be written that the resistances experienced by the majority and minority spin populations are respectively

$$R_{P\uparrow} = \frac{\rho_{F1\uparrow} t_{F1} + \rho_S t_S + \rho_{F2\uparrow} t_{F2}}{A} \tag{1.13}$$

$$R_{P\downarrow} = \frac{\rho_{F1\downarrow} t_{F1} + \rho_S t_S + \rho_{F2\downarrow} t_{F2}}{A} \tag{1.14}$$

where t and A are the thickness and the area of the ferromagnets (F1 and F2) and the spacer (S). Considering now the simplest case in which the two ferromagnets are identical (F1 = F2 = F), the two resistances become

$$R_{P\uparrow} = \frac{2\rho_{F\uparrow} t_F + \rho_S t_S}{A} \tag{1.15}$$

$$R_{P\downarrow} = \frac{2\rho_{F\downarrow} t_F + \rho_S t_S}{A} \tag{1.16}$$

The total resistance in the parallel case then is

$$R_P = \frac{R_{P\uparrow} R_{P\downarrow}}{R_{P\uparrow} + R_{P\downarrow}}. \tag{1.17}$$

Similarly, in the antiparallel case

$$R_{AP\uparrow} = R_{AP\downarrow} = \frac{\rho_{F\uparrow} t_F + \rho_S t_S + \rho_{F\downarrow} t_F}{A} = \frac{R_{P\uparrow} + R_{P\downarrow}}{2} \tag{1.18}$$

ending up with a total antiparallel resistance

$$R_{AP} = \frac{R_{AP\uparrow} R_{AP\downarrow}}{R_{AP\uparrow} + R_{AP\downarrow}} = \frac{R_{P\uparrow} + R_{P\downarrow}}{4}. \tag{1.19}$$

Following the GMR equation 1.12, its final value is

$$GMR = \frac{(R_{P\uparrow} - R_{P\downarrow})^2}{4 R_{P\uparrow} R_{P\downarrow}}. \tag{1.20}$$

In this last equation, it is clear that the GMR effect is highly dependent on the asymmetry of spin-dependent resistivity. Note that this model is valid for $\rho_S t_S << \rho_F t_F$. This means that a large GMR value can be obtained when the scattering events occur in the two ferromagnetic materials and/or at the ferromagnet/spacer interfaces rather than in the non-magnetic spacer, enhancing its spin dependence. The best way to realize this is to use non-magnetic metallic spacer materials with large mean free path (low ρ_S) and reduce the spacer thickness down to values much lower than this mean free path.

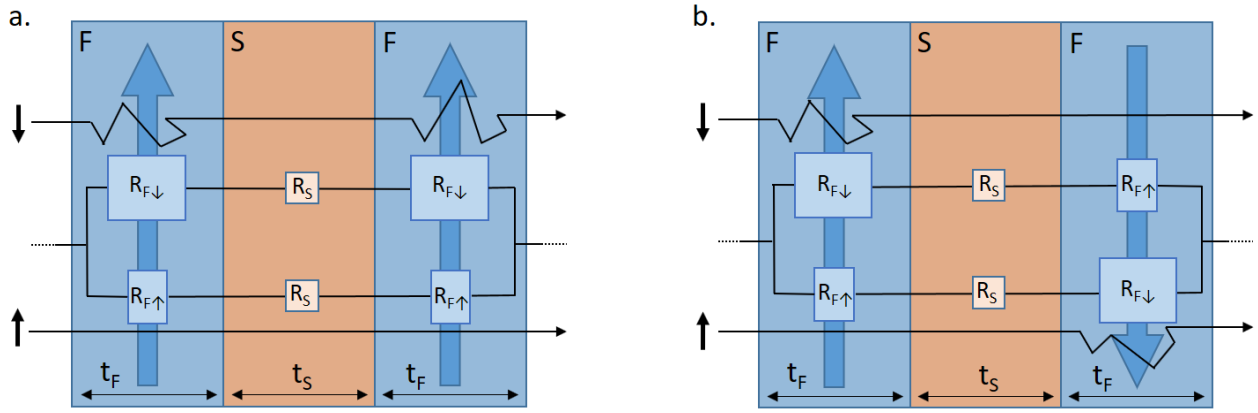

Fig. 1.3: Giant Magnetoresistance | **a.** Schematic of spin dependent transport in a trilayer in parallel configuration and relative resistance scheme in a two current model approach. **b.** As in a. but in antiparallel configuration. $R_{F\uparrow(\downarrow)} = \rho_{F\uparrow(\downarrow)} t_F/A$, $R_S = \rho_S t_S/A$.

Several other models have been created to better describe the phenomenon. Camley and Barnas used a two currents free electron model and developed a semi-classical approach based on Boltzman theory of transport [52] [53]. In a quantum mechanical description using the Kubo formalism, Levy et al. achieved results in good agreement with the semi-classical model and the experimental values [54]. An other simple expression was derived in a phenomenological model developed by Dieny et al. [55]. This last group finally exploited the phenomenon to realize the first spin valve [56], a device that, thanks to the pinning of one of the two ferromagnetic layer, became the first spintronic magnetic field sensor used as read head in hard disk drives and later used as a binary spintronic device leading the way towards the MRAM technology.

1.2.2 Tunnel magnetoresistance TMR

The TMR effect, discovered by Julliére in 1975 [57], involved, similarly to the GMR case, a trilayer sample consisting of two ferromagnetic materials separated by an insulating layer. This stack was later called magnetic tunnel junctions (MTJs). The magnetoresistance found was around 14% at 4.2K and it did not attract much attention up to the 90's when, after the GMR discovery, two independent groups, in Japan and USA, measured the effect at room temperature in AlOx based MTJs [58] [59].

The first explanation, given by Julliére, included the spin polarization of the two ferromagnetic materials. As previously explained in Sec. 1.1, the transport involves the electrons around the Fermi level and in a ferromagnet the two spin populations present a significant difference in the DOS as shown in the schematic in Fig. 1.4. The spin polarization of a ferromagnetic material can then be described as in eq. 1.1. Considering that the tunneling probability (red arrows in Fig. 1.4) depends on the density of the final available states while the number of electrons candidate to tunneling depends on the density of initial filled states and, Julliére estimated the TMR effect as

$$TMR = \frac{R_{AP} - R_P}{R_P} \times 100 = \frac{2P_{F1}P_{F2}}{1 + P_{F1}P_{F2}} \times 100 \tag{1.21}$$

where P_{F1} and P_{F2} are the spin polarization respectively of the ferromagnet F1 and F2 as in Fig. 1.4.

At the beginning, MTJs based on amorphous Al_2O_3 reached TMR values of few tens percent. This value improved significantly thanks to the optimization of the composition of the ferromagnetic materials, with polycrystalline CoFe and amorphous CoFeB, and thanks to improvement in the quality of the tunnel barrier reaching values of 60% 70% [60] [61]. The introduction of a post-deposition annealing also improved the quality of the barrier and, correlatively, the TMR amplitude [62]. In Julliere model, the amplitude of the TMR is defined by the spin-polarization of the magnetic electrode next to their interface with the barrier. Later, the importance of the tunneling barrier itself started to attract the attention of the spintronic community since De Teresa et al. demonstrated that the composition of the barrier material influences the TMR amplitude [63]. In particular, higher TMR values were predicted for highly textured materials and experimentally found by Bowen et al. on a single crystal Fe/MgO/FeCo(001) [64]. Immediately after, a series of studies were announcing increasingly higher values of TMR value found in MgO based MTJ ([65] [66] [67]) up to a trilayer grown with sputtering technique that, combining amorphous CoFeB and crystalline MgO (001), remains, nowadays, the best materials combination (with the highest TMR value ever measured of 604 % at room temperature [68]). The reason for this was previously predicted thanks to various theoretical works that took into account the evanescent DOS in the barrier [69] [70] [71]. In systems such as Fe/MgO, thanks to the almost identical crystalline symmetry of the Bloch states of the two materials, it was found that the evanescent wave in the barrier decays much faster for some electronic bands (namely Δ_2 and Δ_5) than for others (Δ_1). This means that the tunneling events of Δ_1 electrons are much more probable than for Δ_2 and Δ_5. Moreover, it turns out that both majority and minority states of Δ_2 and Δ_5 symmetries are existing at the Fermi energy (from eq. 1.1, this means that the polarization is relatively low). This does not happen for the Δ_1 symmetry that, having only one spin population at the Fermi level, has a spin polarization of 100% at Fermi level. All these features, in a trilayer structure with two ferromagnets and a relatively thick tunnel barrier, yield expected value of TMR above 1000% at room temperature [72]. Unfortunately, such values have never been observed probably due to imperfections of the crystalline structure. Also, by lowering the thickness of the tunnel barrier, the contribution of electrons with Δ_5 symmetry becomes relevant. This, due to the lower spin polarization of these electrons, leads to a lower value of TMR.

Finally, the TMR effect, due to its large amplitude at RT associated with resistance values compatible with the CMOS electronics (resistance of MTJs of the order of a few $k\Omega$), is the most used in spintronics and, in particular, in MRAM.

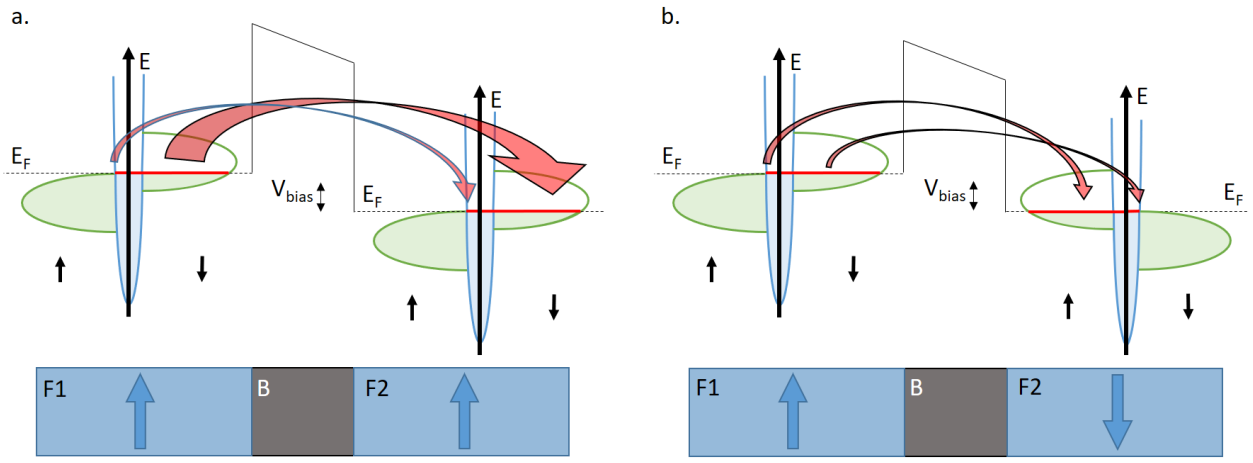

Fig. 1.4: Tunnel Magnetoresistance | **a.** Schematic of a spin dependent tunneling in a trilayer system (two ferromagnets F1 and F2 and the tunnel barrier B) in parallel configuration. The red arrows indicate the tunneling probability. **b.** As in a. but for the antiparallel configuration.

1.2.3 Spin transfer torque STT

This effect, predicted in 1996 by Slonczewski and Berger [73] [74], describes the interaction of a spin-polarized current with the local magnetization. It relies on the conservation of the total angular momentum for which the electronic spin and the local magnetization exert a reciprocal torque in opposite direction. This effect is used in trilayer structures such as the ones described previously for GMR and TMR. In the schematics shown in Fig. 1.5, let us consider the magnetization of F1 fixed, while the one of F2 is free to move. When a non-polarized current flows in a direction from F2 to F1, the electrons flow from F1 to F2 as in Fig. 1.5a. In this case, the non-spin-polarized electrons interact first with the local magnetization of F1. The local interaction tends to make the spins (in black) aligned with the magnetization direction (in blue), ending up with a spin-polarized current. This current interacts then with the non-magnetic layer for which tunneling or diffusion occur in case of insulating or metallic spacer respectively. When the spin-polarized current reaches the ferromagnet F2, the local interactions tend to align the spin to the local magnetization as it happened for F1. In this case, contrarily to the interaction with F1, the angular momentum carried by the conduction electrons is different from zero. This means that, for the conservation of the total angular momentum, the electrons tend to align their spin to the magnetization direction (the spin in black becomes the spin in light gray) and, at the same time, a torque acts on the local magnetization and tends to align it to the initial spin direction (the magnetization in blue becomes the one in light blue), i.e. the direction of F1 magnetization. In a formal way, this transfer of angular momentum from F1 to F2 can be expressed as a sum of an adiabatic $\tau_{\parallel}$ and a non-adiabatic torque $\tau_{\perp}$

$$\tau_{STT} = \frac{\partial \vec{m}}{\partial t} = \tau_{\parallel} + \tau_{\perp} = -\gamma a_{\parallel} V \vec{m} \times (\vec{m} \times \vec{p}) + \gamma a_{\perp} V^2 \vec{m} \times \vec{p} \tag{1.22}$$

where $\vec{p}$ is the direction of the polarizer magnetization (in this case the one of F1), V is the applied voltage, $a_{\parallel}$ and $a_{\perp}$ contain the material parameters to take into account [75]. In the case of an MTJ, as it is for the work presented in this thesis, the non-adiabatic term, also called field-like term, results to be negligible with respect to the other one (known also as damping-like term) [76] [77] [78]. For this reason, from now on, only the $\tau_{\parallel}$ contribution will be considered. This last depends both on the magnetic and transport properties of the materials involved. In particular, the value of $a_{\parallel}$ can be expressed as

$$a_{\parallel} = \frac{\hbar}{2e} \frac{\eta}{R \times A} \frac{1}{t M_S} \tag{1.23}$$

where η and $R \times A$, respectively the STT efficiency (dependent on the spin polarization) and the resistance*area product, define the quality of the tunnel barrier, while the thickness t and M_S are the parameters of the ferromagnetic layer on which the STT is acting.

Using the same formalism, the effect of an opposite current direction can be considered as in Fig. 1.5b. In this case, the current is spin-polarized by F2 magnetization and diffuses towards F1. At the interface with F1, the electrons whose spin is antiparallel to the magnetization of F1 are retro-diffused again towards F2. In this way, F2 feels a torque that tends to align its magnetization in a direction antiparallel to the F1 magnetization. This means that the current direction can be used, through the application an high enough torque, to switch the magnetization of the layer F2 in a parallel or antiparallel configuration with respect to F1. The torque generated through STT has to overcome the one of the damping, resulting in a critical current value I_{C0} that, at a temperature of 0K, can be written as [79]

$$I_{C0} = \frac{2e}{\hbar} \frac{\alpha_G}{\eta} \mu_0 M_S V H_{eff} \tag{1.24}$$

where α_G is the Gilbert damping. This concept has been described for a fixed magnetization of F1 but it is also valid in other cases by considering, for each current direction, the mutual STT of trasmitted and reflected electrons on both magnetic layers. Moreover, being a local interaction, the effect exponentially decreases with the thickness of the magnetic layer to switch [80].

Experimentally, the STT effect was observed in 1998 when resistance variations were measured accordingly to the direction of the injected current [81]. The first complete switching of a ferromag-

net was observed in 2000 [82], leading later to the switching in an Al_2O_3 based MTJ in 2004 [83] and in an MgO one in 2005 [84] [85] [86].

Nowadays, the writing mechanism of the most commonly developed of MRAM relies on STT and, therefore, it is called STT-MRAM.

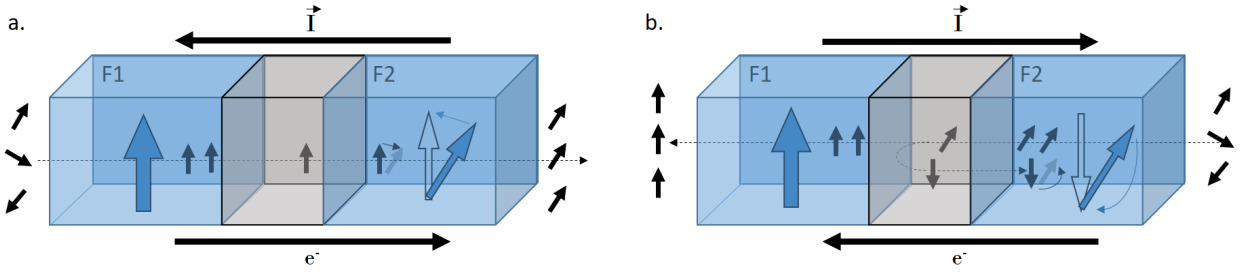

Fig. 1.5: Spin Transfer Torque | **a.** Schematic of the spin transfer torque effect in a trilayer for a current direction. **b.** Schematic of the spin transfer torque effect in a trilayer for a current direction opposite to the case shown in a.

1.3 Magnetization dynamics

In presence of a field, the equilibrium state of the magnetization occurs exclusively when the two vectors are collinear. In a magnetic body, all the energies, previously described, can be summed up to form an effective field that results from its minimization

$$\vec{H}_{eff} = -\frac{1}{\mu_0 M_S V}\frac{\delta E_{TOT}}{\delta \vec{m}} \tag{1.25}$$

where V is the volume and E_{TOT} the total energy.

If the magnetization is not in an equilibrium state, a complex dynamics starts depending on material properties and external conditions (field, temperature, etc.). This is described by a partial differential equation briefly detailed in the next paragraph.

1.3.1 Landau Lifshitz Gilbert Slonczewski equation LLGS

The description of the magnetization dynamics was formalized by Landau and Lifshitz in 1935 (eq. 1.26) and later, in 1955, it was reviseed by Gilbert with an equivalent formulation (eq. 1.27) [87] [88].

$$\frac{\partial \vec{m}}{\partial t} = -\mu_0\gamma\vec{m}\times\vec{H}_{eff} - \lambda\vec{m}\times(\vec{m}\times\vec{H}_{eff}) \tag{1.26}$$

$$\frac{\partial \vec{m}}{\partial t} = -\mu_0\gamma\vec{m}\times\vec{H}_{eff} + \alpha_G(\vec{m}\times\frac{\partial \vec{m}}{\partial t}) \tag{1.27}$$

where γ is the gyromagnetic ratio and λ an effective damping parameter that can be related to the α_G, the Gilbert damping, with the formula $\lambda = \alpha_G\gamma/(1+\alpha_G^2)$.

The first term in both equations describes the precessional motion of the magnetization around the effective field (also known as Larmor equation). This term describes a conservative motion of the magnetization around the effective field that persists without never reaching a stable state as shown in Fig. 1.6a. In opposition to this, the second term, as in Fig. 1.6b, accounts for the energy dissipation with a viscous approach, i.e. proportionally to the magnetization variation in time (this concept will be detailed in the next chapter). The dimensionless parameter α_G describes phenomenologically the dissipation dependently on the material characteristics and on other phenomena still under discussion [89].

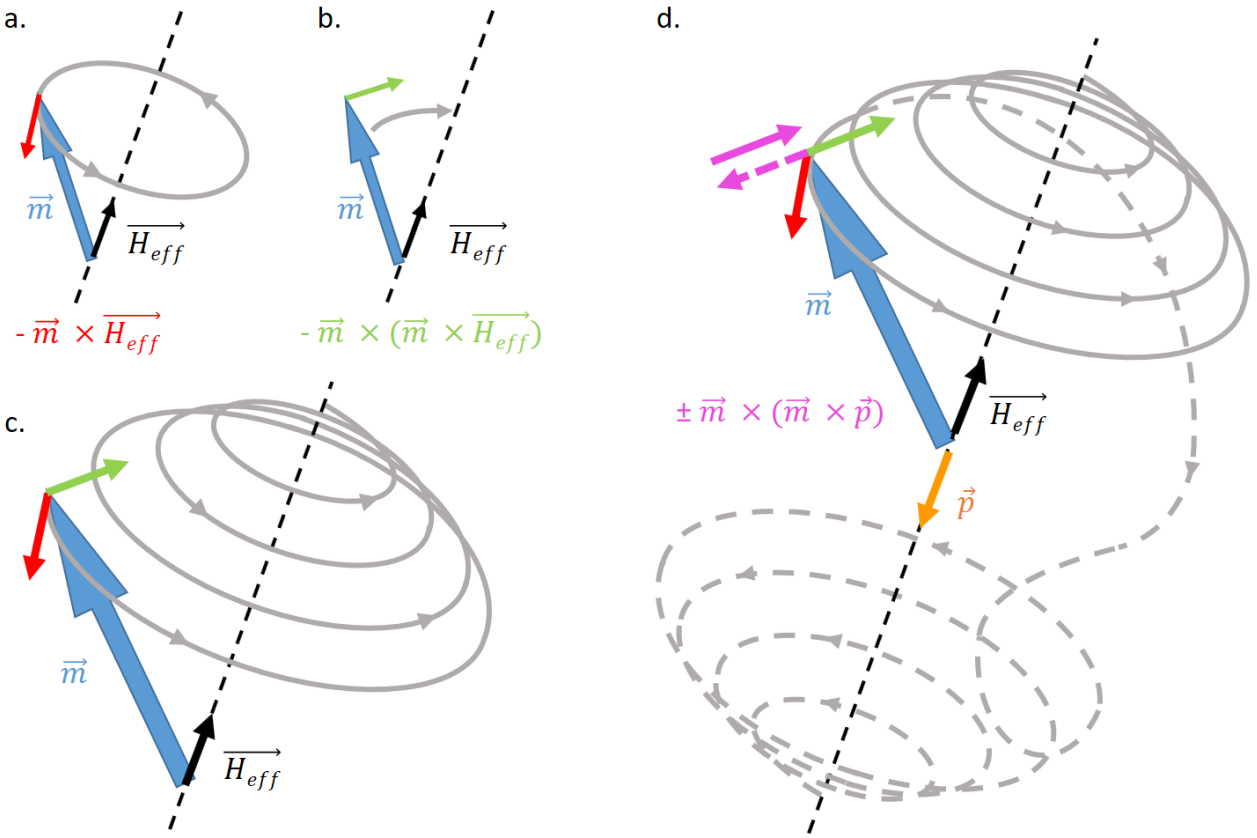

Fig. 1.6: Magnetization dynamics | **a.** Larmor precession trajectory (in gray) of the magnetization (in blue) around the effective field direction (in black) induced by the torque vector (in red). **b.** Trajectory of the magnetization induced by a damping torque (in green). **c.** Trajectory of the magnetization induced by the two terms present in the LLG equation as in 1.26. **d.** Trajectories of the magnetization induced by the LLGS equation as in 1.28 with the adiabatic term of spin transfer torque $\tau_{\parallel}$ (in pink) for current direction favoring parallel or antiparallel configuration (respectively in dashed and continuous line).

Finally, the two terms toghether describe a damped motion of the magnetization vector as shown in Fig. 1.6c. The precession, ruled by the Larmor equation, is damped down by the second term with a velocity dictated by the Gilbert damping α_G.

After the formalization of the STT effect, in 1996 as previously described, the STT term was included in a more complete formulation of the LLG equation. The torque $\tau_{\parallel}$, so called because the it lies in the plane formed by the magnetization $\vec{m}$ and the polarizer $\vec{p}$, was added to eq. 1.27 to form the Landau Lifshitz Gilbert Slonczewski equation (LLGS)

$$\frac{\partial \vec{m}}{\partial t} = -\mu_0 \gamma \vec{m} \times \vec{H}_{eff} + \alpha_G (\vec{m} \times \frac{\partial \vec{m}}{\partial t}) - \gamma a_{\parallel} V \vec{m} \times (\vec{m} \times \vec{p}). \tag{1.28}$$

As described in the previous section, the adiabatic torque can both favor the parallel or antiparallel alignment of the magnetization with the polarizer depending on the direction of the current.

This formulation will be extended in the next chapter and used to simulate the magnetic behavior of the device under field and STT.

1.4 Magnetic random access memory (MRAM)

In the so-called Von Neumann architecture, the most used one in electronics nowadays, the physical separation between processing unit and memory unit is the crucial characteristic at the base of a bottleneck effect. The limitation in terms of computational speed comes mainly from the slow information exchange between the two units. The way found to optimize this is to create a memory hierarchy as shown in Fig. 1.7a. The memories at the top of the hierarchy are the most frequently accessed and for this reason they are physically placed closer to the processing unit than the ones at the bottom of the hierarchy. Because of this, the characteristics required for memories such as RAM and cache are high speed, low retention and low memory capacity. Contrarily, the memories at the bottom of the hierarchy, with many less access and then placed far from the processor, do not need fast performances but they require very high retention time and memory capacity. In terms of power consumption, the bottom part of the pyramid is characterized by non-volatile memory technologies for which the system consumes power only for the writing-reading occurrences while, in the top part, volatile memories, that consume power even in stand by, are exploited in order to obtain the fast performances required. In the last years, alternative technologies with comparable speed and non-volatility have been investigated in order to replace the top part of the pyramid. Between those, magnetic random access memories (MRAM) are attracting the attention of the big manufacturers because of its characteristics. This kind of technology bases its memory cell on a trilayer structure called magnetic tunnel junction (MTJ), as in Fig. 1.7b - e. The two magnetic layers, separated by a tunnel barrier, are respectively a reference layer with a fix magnetization direction and a free layer. The magnetization of the latter is free to switch between two stable states in direction parallel or antiparallel to the reference magnetization. The energy barrier E_b separating the two states is an important parameter that represents the thermal stability $\Delta = E_b/(k_B T)$. The required value of Δ (typically higher than 60) depends on several parameters such as integration capacity or operating temperature. From this parameter it is possible to extract the retention, i.e. the time for which the device is supposed to retain its bit value.

As explained in section 1.2.2, the parallel and antiparallel magnetization configurations can be read as a low and high resistance values. In this way, the TMR effect is used as reading mechanism by associating the low and high resistance values respectively to the logic value 0 and 1.

Concerning the writing mechanism, both field-driven and current-driven switching effects have been used during the years in the different MRAM generations [90].

- **Stoner Wolfarth MRAM** | In the first generation each MTJ was integrated between two perpendicular current lines (bit and word line) as in Fig. 1.7b [91]. The switching mechanism is based on a field-driven effect generated by the current passing into those lines. The field, generated by the current passing through one of the two lines, acts on the magnetization of the free layer but it is not sufficient to switch it. Only when both lines generate a synchronized field on the same junction, its magnetization is able to switch (principle of Stoner Wolfarth astroid). This mechanism of selection is effective at the level of single cell but due to dot to dot variability, has high writing error rate at chip level. Therefore, this technology did not reach the market.

- **Toggle MRAM** | The missing element to the previous one was added by [92]. The use of a synthetic antiferromagnet as free layer was exploited in the Toggle MRAM that was the first one to officially get commercialized [93] [94] [95]. An integration similar to the previous one and a proper design of the current pulses allows the creation of a rotating field that acts on the free layer thus switching it. The endurance of those field-written technologies was very high since no degradation of the MTJ was induced by the field. Despite this, the creation of the field with current pulses requires rather large current of a few mA which yields a high power consumption and limits the downsize scalability and the memory capacity due to electromigration in the field lines.

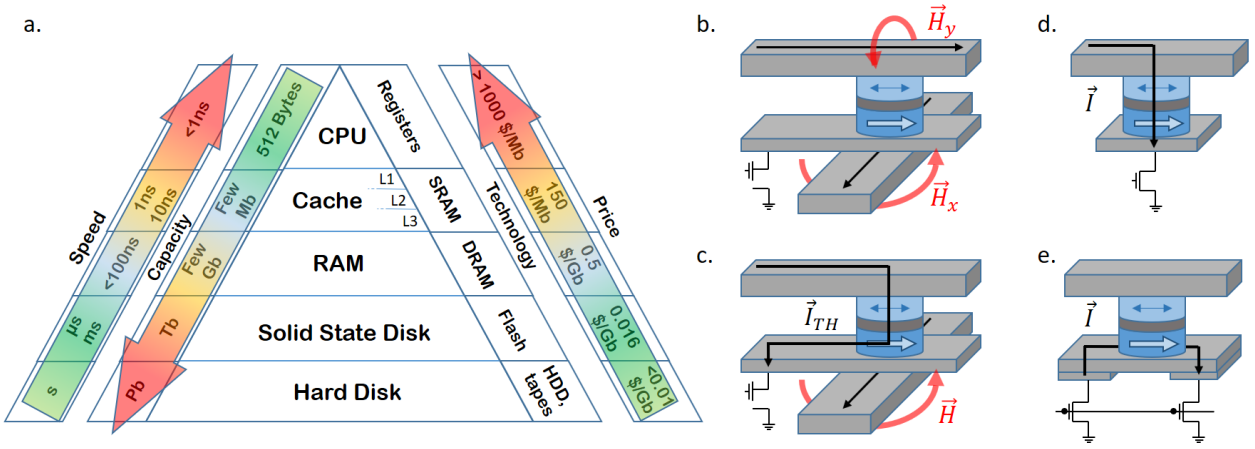

Fig. 1.7: Memory hierarchy and MRAM | **a.** The memory hierarchy represented in the triangle with performances (speed and capacity), the currently used technology and their price. The arrows indicate an increasing value for such characteristics. **b.** Integration scheme for Stoner Wolfarth and Toggle MRAM. The two fields (in red), induced by the currents in the two wires (in black), are responsible for the switching of the magnetization of the free layer. **c.** Integration scheme for the Thermally Assisted (TA) MRAM. The current I_{TH} create a temperature-induced reduction in the energy barrier of the storage layer magnetization that is switched with the field in red. **d.** Integration scheme for the STT MRAM. The magnetization switching occurs for currents $\vec{I}$ higher than a critical value $\vec{I_C}$. The reading path is the same as for the writing one. **e.** Integration scheme for the SOT MRAM. The magnetization switching occurs for currents $\vec{I}$ higher than a critical value $\vec{I_C}$. The writing path does not pass through the device.

- **Thermally Assisted MRAM (TA MRAM)** | The last field-driven generation was the one of Thermally Assisted MRAM. The principle of this technology was to create a free layer with a very high energy barrier in standby that, at the moment of the field-induced switching, was reduced thanks to the Joule heating around the tunnel barrier created by an injected current throughout the MTJ (Fig. 1.7c). The magnetic stack was exploiting two antiferromagnetic materials with different Neel temperatures to exchange bias the reference and the free layer. The temperature reached during the current pulse was higher than the blocking temperature of the antiferromagnet used for the free layer, but lower than the one used for the reference. In this way, the lowering of the energy barrier during the writing process was ensuring good power consumption, better selectivity and at the same time the retention time was incredibly high. This technology reached the market but, despite the impressive performances, it was immediately replaced by the first MRAM technology with current induced switching [96] [97].

- **Spin Transfer Torque MRAM (STT MRAM)** | The STT MRAM generation is the most advanced technology in this field. The writing mechanism, based on the STT effect (described in section 1.2.3) allows a low power consumption and a much higher density integration due to the fact that the current path is the same for writing and reading (Fig. 1.7d). The integrability was further improved by passing from the in-plane magnetized MTJs (that required an elliptical shape) to the perpendicularly magnetized devices (p-STT-MRAM) [98]. This technology is now commercialized by the big microelectronics companies (Samsung, TSMC, INTEL, Global Foundries). In table 1.1, STT MRAM is compared to other emerging technologies and to the ones currently used [99] [100] [101] [102] [103] [104] [105]. Among the emerging technologies of non-volatile memories, STT MRAM turns out to have the best performances together with phase change memories (PCM). While the first has a big advantage in terms of write endurance (that can reach 10^{16} cycles), the second one has a smaller cell size and therefore a higher density. A disadvantage of the STT MRAM technology is the price significantly higher than for PCM. Despite this, the predictions for the scalability are definitely in favor of the STT MRAM technology that is expected to reach the 12nm node in the next 4 years with

	Emerging technologies			Standard technologies	
	STT-MRAM	**PCM**	**RRAM**	**DRAM**	**Flash NAND**
Non-volatile	YES	YES	YES	NO	YES
Endurance (# cycles)	$>10^9$ (10^{16})	10^7	10^6	10^{15}	10^5
Bit density per die	1Gb	128Gb	8Mb	16Gb	1Tb
Cell size (F2)	6-30	4/2L	6-30	6-8	4/96L
Speed	10ns	10-100ns	100ns	10ns	100000ns
Switching power	Medium/Low	Medium	Medium	Low	High
Price (in 2019)	10-100$/Gb	<0.3$/Gb	100-1000$/Gb	0.5$/Gb	0.016$/Gb

Table 1.1: Technologies comparison. Optimal, intermediate and negative aspects are marked respectively in green, orange and red. The data are taken from Yole report 2020.

respect to the limit of 28nm for the PCM. STT-MRAM are first being used in replacement of embedded FLASH memory since the scalability of eFLASH is limited to the 28nm node due to their complexity of fabrication. Indeed the fabrication of eFLASH requires between 15 and 20 levels of masks which make it very expensive. In comparison, STT-MRAM only require 3 levels of masks to be integrated in CMOS technology. For these applications, STT-MRAM has also the advantage of much longer write endurance than eFLASH. The second goal that companies try to achieve with STT-MRAM is SRAM replacement. The advantage of STT-MRAM over SRAM is their much smaller footprint ($20F^2$ versus $200F^2$ where F is the feature size i.e. the technology node). However, progress in STT-MRAM development still need to be realized to increase the write endurance at short write pulse width ($\approx 1ns$). A better candidate for this application may be the SOT MRAM described below at the cost of an increase cell footprint but still smaller than conventional SRAM. For DRAM application, the density of STT-MRAM would have to be significantly increased. Here, the remaining difficulty is that of etching the magnetic stack at small feature size and small pitch. Concepts of hybrid DRAM with a part of DRAM in CMOS technology and another part in STT-MRAM technology is being considered.

- **Spin Orbit Torque MRAM (SOT MRAM)** | A more recent MRAM generation is based on spin orbit torque (SOT) switching. This mechanism involves the integration of a three terminal device that, for this reason, has a bigger cell size with respect to the previous one (Fig. 1.7e). Despite this, the switching time, much shorter than for the STT, and its higher endurance, due to the fact that the writing current does not pass through the MTJ, makes this device an interesting candidate to be integrated in L1 or L2 cache [106] [107] [108].

Finally, the STT MRAM technology with all its pros and cons turns out to be the most interesting emerging technology of non volatile memory. Its market is expected to grow significantly with a compound annual growth rate higher than 42%. For this reason, exploiting this technology for the development of new non-volatile and low power consumption devices for neuromorphic applications seems promising. In the next sections, the first and more significant attempts to the realization of a multi-level memory device (memristor) using spintronics will be described. The analysis of advantages and disadvantages of those will finally lead to the description of the innovative concepts developed in this thesis.

1.5 Spintronic memristors: state of the art

Since the publication in 2008 of Strukov et al. [109], in which they claimed to have created the first memristor, the interest of the scientific community begun to be redirected towards neuromorphic computing and possible hardware implementations. In few years, excellent results were achieved in this sense by using different kind of technologies. In particular, in spintronics, the pioneering work of the group in Thales (Paris) using spin torque nano-oscillators led to impressive results. In fact, the analogy between neurons and oscillator functionalities, where the synaptic weights are played by the interactions between devices, have been demonstrated in several publications [110] [111] [18] [112] [113]. Despite this, a simpler and more reliable realization of a more complex neuromorphic circuit would rely on the use of multi level memory devices for the role of synapses. Since the aim of this work is to propose new concepts for its realization, a brief overview of the existing devices will follow. It was investigated the possibility to realize such device using different technologies exactly as for the binary memory devices. An overview of the recent and most meaningful results is given in reference [16]. In spintronics, several interesting attempts have been pursued too. Here below follows a brief description of pro and cons.

- **Domain wall based memristors** | The first concept developed to achieve the multilevel resistance states was based on domain wall nucleation and motion in the free layer of a magnetic tunnel junction [114]. The general idea was to exploit the ratio between parallel and antiparallel configurations separated by the domain wall, to achieve intermediate values of TMR (Fig. 1.8). Moreover, the injection of a current into the MTJ would act on the domain wall as STT resulting in a displacement. Several pinning sites, both artificial and natural, can allow the stabilization of the domain wall leading to a stable intermediate resistance in static conditions. The first realization of this device in [115] marked the beginning of a generation of devices based on domain wall motion. Despite the results achieved in the last years, this kind of device presents some limitations directly linked to the concept. In general, the creation of a stable domain wall requires a lateral size of the device comparable or relatively bigger than the one of a state of the art STT MRAM (<40nm of diameter). Moreover, the

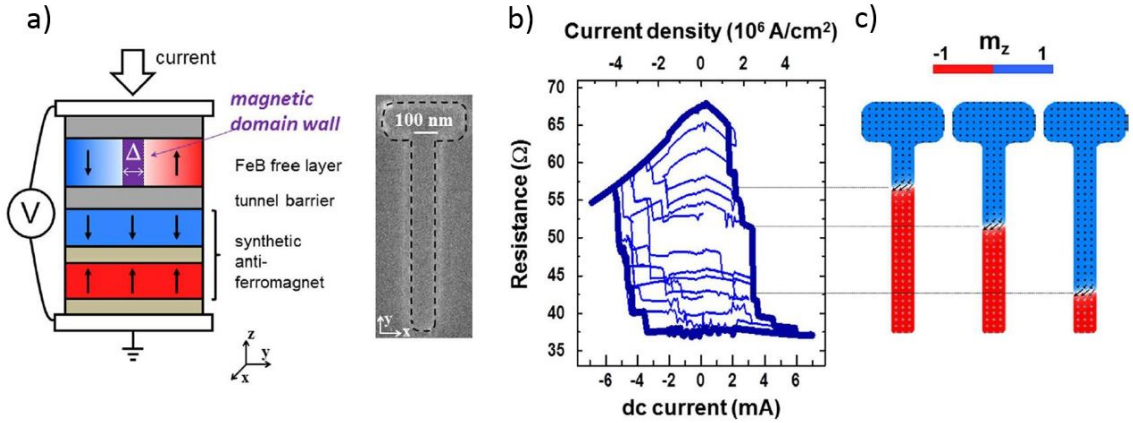

Fig. 1.8: Memristor based on Domain Walls motion and pinning | **a.** Schematic of the device side view and SEM image of the top view. **b.** Resistance loop as function of dc current with an out-of-plane field of Hz=85Oe. **c.** Micromagnetic simulations of the domain wall displacement in the device. [115]

number of intermediate resistance states depends on the pinning sites distribution in the magnetic medium. This means that bigger lateral sizes would favor not only a higher number of resistance states but also a better stability of those. In the MTJ structure developed in [115], the optimized shape and lateral size are in the few hundreds of nanometers range. Similarly, the DW displacement in a Hall cross was optimized to give incredibly stable resistance levels [116]. Also in this case the lateral size of the device is in μm range. Other interesting works

in this area describe the DW dynamics in structures conceived for racetracks memories such as nanostrips or nanowires [117] [118] or in three terminal devices [119]. In this case, the hard integrability of these structures would difficultly allow the reproducibility of those results in a real circuit.

- **Ferroelectric memristors** | A similar phenomenon was exploited also in a ferroelectric material integrated in a ferroelectric tunnel junction. In this kind of device, the spontaneous magnetization arising in an insulating material (as for example $BaTiO_3$) can be manipulated through the application of an electric field (Fig. 1.9). The total resistance can vary by a few orders of magnitude giving an On/Off ratio much larger than for MRAM. Few works show that between the two saturated states, several intermediate resistances are achievable because of the different domain configurations in the ferroelectric junction [120] [121] [122] [123]. Apart of the relatively big size needed for this device, the main disadvantage is the destructive reading mechanism that requires a writing-after-reading process.

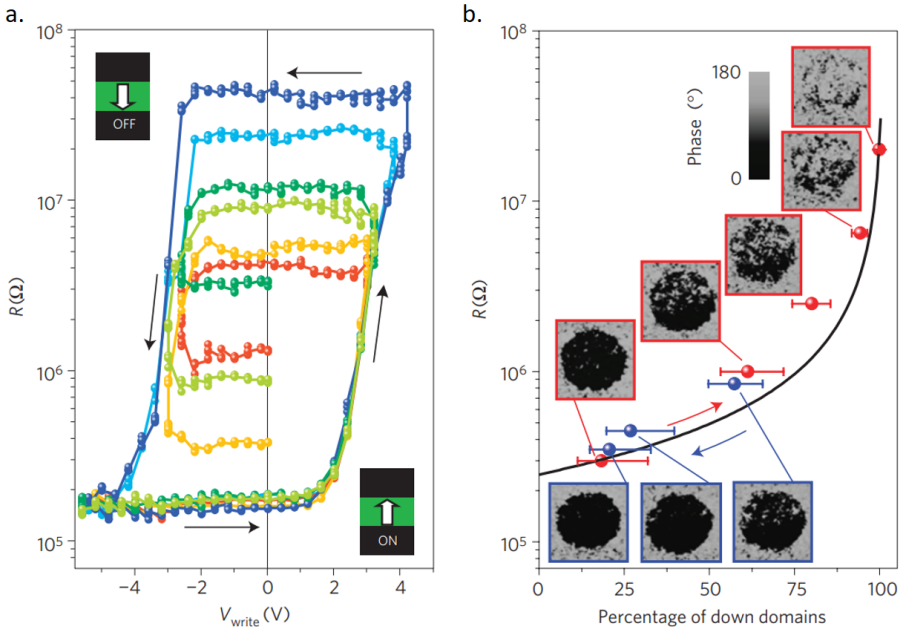

Fig. 1.9: Memristor based on ferroelectric materials | **a.** Resistance loop as function of current pulses amplitude. **b.** Resistance variation as function of the relative fraction of up and down domains from Piezoresponse Force Microscope (PFM) phase images. [123]

- **Memristor based on exchange biased ferromagnetic layer** | Another concept, developed at Tohoku University, is based on the coupling between an out-of-plane magnetized layer and an antiferromagnetic layer [124]. They studied the reversal of the ferromagnetic layer by injecting current through the antiferromagnetic layer exploiting its high spin-orbit interaction (Fig. 1.10). The results showed up a gradual switching of the ferromagnet due to a multi-domain reversal of the magnetization. More interestingly, in a recent work it is shown how, with the same principle, they are able to reproduce the neuron functionalities, with small sizes (few hundreds of nm) and binary switching, and synaptic functionalities with bigger sizes (μm range) and gradual switching [125]. These impressive results are however balanced by the relatively large lateral size of the device (μm range), and by the use of the antiferromagnet material that can limit the temperature working range.

- **Hybrid RRAM - MRAM memristors** | An interesting solution for the realization of a memristive device consists in the creation of a hybrid technology between MRAM and RRAM [126] [127]. The device is based on a classical MTJ with an MgO barrier. The application of high voltages is used to drive the oxygen migration in the barrier in order to

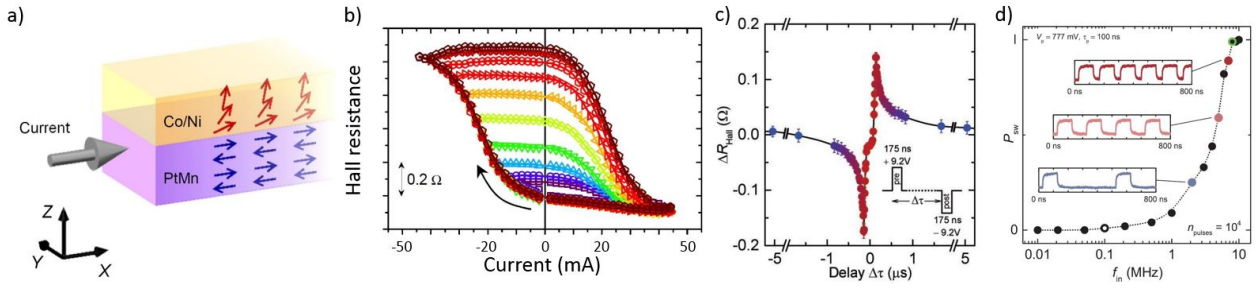

Fig. 1.10: Memristor based on SOT switching of an exchange biased layer | **a.** Schematic of the device. **b.** Resistance loops as function of current pulses. **c.** Resistance variation dependence on the delay between pre and post synaptic pulses as in the inset. **d.** Switching probability dependence on the frequency of the input train of pulses. [124] [125]

obtain a resistance variation typical of RRAM (Fig. 1.11). At the same time, the STT effect can act on the magnetization of the two electrodes by varying furthermore the resistance. The interplay of the two effects can be exploited in the same device to behave as a synapse, by exploiting the gradual resistive switching, or as neuron, using the STT effect. With this technology, feature such as spike timing dependent plasticity (STDP) has been successfully reproduced [128]. The main disadvantage of this technology relies on the poor endurance typical of the RRAM as well as in dot to dot variability since these phenomena of atomic migration are purely statistical. In fact, the use of ion migration through the barrier limits the number of possible cycles and degrades one of the strong points of the MRAM which is its write endurance.

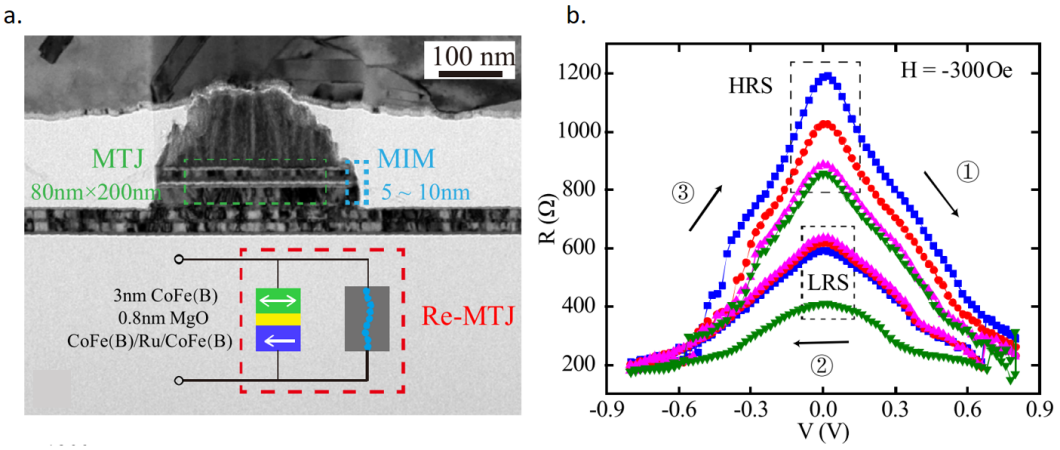

Fig. 1.11: Memristor based on hybrid MRAM and RRAM technology | **a.** TEM cross section of the device and relative electrical model. **b.** Resistance variation dependence on the voltage pulses amplitude. [127]

- **Multi - MTJs memristors** | A further idea to achieve a multi level resistor consists in the use of several binary devices interconnected in series or in parallel. In the case of MTJs connected in series, some experimental works show the resulting memristive behavior obtained from the injection of current pulses [129] (Fig. 1.12). For a chain of N identical MTJs, a maximum number of N+1 resistances can be achieved. Moreover, the device variability, known to be a relevant problem in the fabrication of MTJs, can be exploited to achieve an higher number of intermediate states. In fact, by resetting with field the full chain before each pulse, the statistical switching of different MTJs allows to reach other resistance values up to a maximum of 2^N. In a similar way, the parallel connection has been investigated with similar purpose. In this case, the array can be gradually switched with STT or SOT, as in the case of ref [130], through the injection of current pulses designed to statistically switch part of the device. The

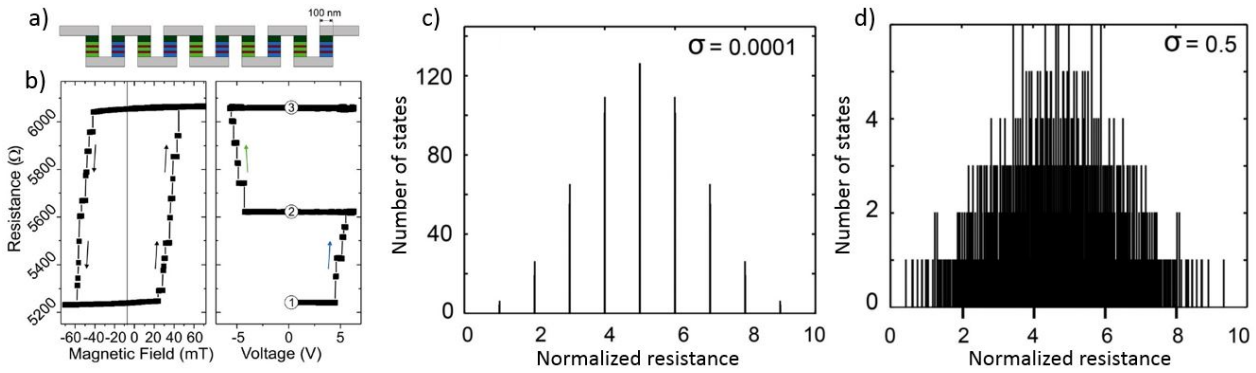

Fig. 1.12: Memristor based on interconnection of MTJs | **a.** Schematic of the device. **b.** Resistance states as function of magnetic field (left) and voltage pulses (right). Resistance states distribution with small **c.** and higher **d.** MTJ variability (with standard deviation σ respectively of 0.0001 and 0.5). [129]

switching probability curve can be exploited for this. In both cases, the number of intermediate states is linked to the number of MTJs present in the device. Despite the advantages of those devices, directly linked to the state of the art MRAM technology, the integration of several MTJs represents the main limitation in terms of lateral size and scalability.

- **Skyrmion based memristors** | A last concept, very fascinating from the physics point of view, is based on the creation annihilation and motion of skyrmions. These magnetic objects, widely investigated in the last years, are used to tune the resistance of a MTJ structure in different ways. In ref [131], the authors show how the resistance varies monotonously with the current polarity because of injection and ejection of skyrmionic bubbles in the device. Despite the excellent results, the device size is rather big (few μm lateral size) and difficult to integrate. Another idea is based on the size variation of the bubble due to voltage controlled anisotropy or RKKY variation in an SAF induced by a piezoelectric material (Fig. 1.13) [132] [133]. Those devices imply the creation of a magnetic bubble in the free layer of a MTJ. Despite the interesting concepts, those have not been yet experimentally realized.

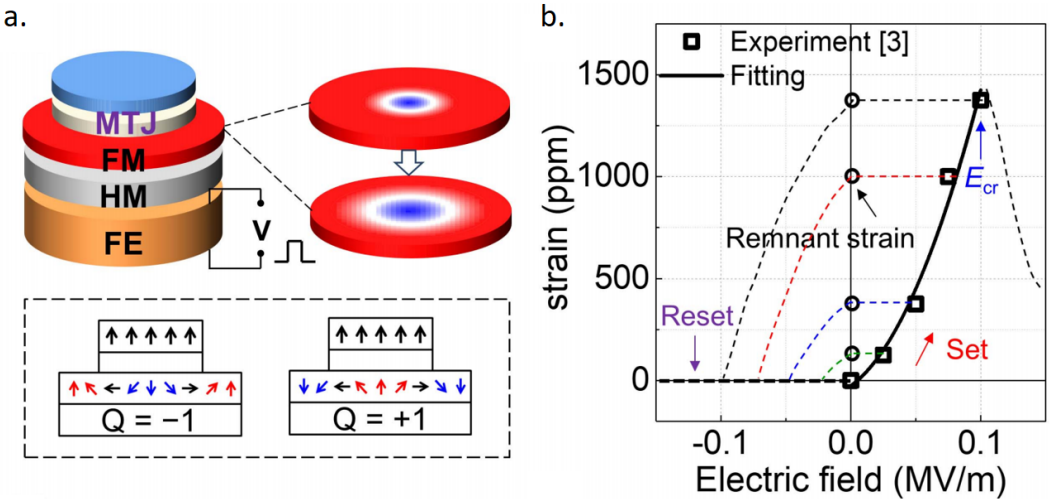

Fig. 1.13: Memristor based on skyrmion dynamics | **a.** Schematic of the device as in ref [132]. **b.** Strain evolution dependence on the electric field.

The main concepts developed in spintronics for the realization of a multilevel memory device present interesting physical phenomena that for different reasons are hardly implementable in a compact and easily scalable device. Those requirements are fundamental for a possible integration in a real

neuromorphic circuit and, more generally, for a device that could satisfy the industrial standards. For this reason, in the next section, other new concepts are proposed to address and solve those problems.

1.6 New memristor concepts

The objective of this thesis is to conceive and develop memristive devices based on new concepts in order to favor scalability, integrability and, more generally, closer to the industrial requirements. For this reason, the devices described in this study are based on a single nano-sized pillar to reduce the cell size and favor the scalability. Moreover, their working principles rely on strong concepts developed in the spintronic community along several years. Here below, a short overview of the two main concepts investigated in this thesis is given together with the basic spintronic effects exploited.

1.6.1 Memristor based on angular variation of TMR

As already described in Sec. 1.2.2, the TMR effect is associated with variations in the relative orientation of the magnetization of the free layer with respect to the one of a reference layer. In a binary device the configurations in which those are parallel (P) or antiparallel (AP) give the minimum and the maximum resistance value of the magnetic stack. It was demonstrated that, between the minimum and maximum values, other intermediate resistances can be measured as function of on the angle (between 0° and 180°) between the two magnetization directions as in Fig. 1.14b [134] [135]. It is found that the conductance varies as a cosinus function of this angle. This feature can be exploited in an in-plane MTJ, comprising an analyzer of fixed magnetization and a free layer(respectively AL and FL in Fig. 1.14a), to achieve several intermediate resistance states as required for a memristor. To do this, the magnetization of the free layer has to be stable along all the in-plane directions. Only in this case, stable intermediate resistance states can be realized. The realization of such magnetic media represents the first big challenge for the realization of such device. The writing mechanism is based on the STT effect coming from a second magnetic layer with fixed out-of-plane magnetization (POL in Fig. 1.14a). In ref. [136], it was indeed demonstrated that

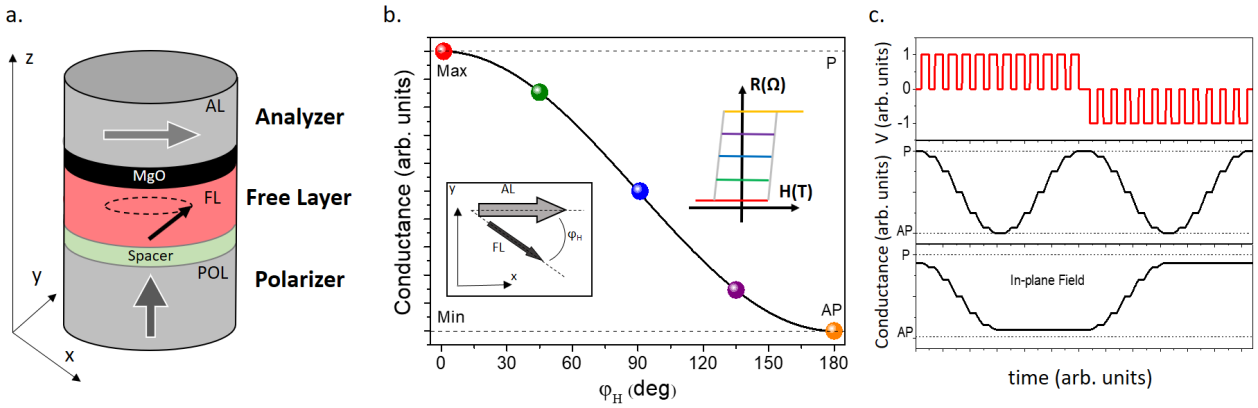

Fig. 1.14: Memristor based on the angular variation of TMR | **a.** Schematic of the device. **b.** Angular variation of the conductance. **c.** Ideal conductance variation of the device due to a train of pulses (as in the top panel) without and with an in-plane transverse field (respectively central and bottom panel).

if the magnetization of such polarizer is perpendicular to the plane, the STT coming from this POL acts on the in-plane free layer as an in-plane torque that makes the FL magnetization precess around the perpendicular direction. Clockwise and anticlockwise precessions are obtained with positive or negative polarity of the voltage. In this way, instead of applying a dc current to obtain precession, it would be possible to discretely rotate the magnetization in both directions through the application of current pulses properly designed in amplitude and duration. In particular, if the pulse length

t is set to be a fraction of the precession period T, the magnetization is supposed to rotate by a corrisponding angle $\alpha \approx t/T * 2\pi$. With this approach, starting from a configuration where the FL and AL have parallel magnetization, by applying voltage pulses of the same polarity, the resistance will increase up to reach its maximum in the antiparallel configuration then it will start decreasing if we keep on sending pulses of same polarity (as in the central panel of Fig. 1.14c). This non-monotonous behavior of the resistance variation with the voltage polarity is not compatible with the requirements for a memristive behavior. To obtain the monotonicity, a local in-plane field can be applied in a direction perpendicular to the in-plane AL magnetization direction. In this way, the magnetization rotation will be limited to the half plane between the parallel and the antiparallel configuration and the memristive functionalities can be achieved (bottom panel of Fig. 1.14c).

In Chapter 3 the development of this device will be detailed. In a first part, the free layer with isotropic properties will be modeled with a modified LLG equation. This will be inserted in a macrospin model for the whole device demonstrating numerically the memristive functionalities under field and current. In a second part, the experimental realization of the free layer will be described and compared to the model. A brief description of the material development for the other parts of the magnetic stack will follow. Finally, the electrical results obtained from the complete device will be analyzed for different cases.

1.6.2 Memristor based on a granular structure of the free layer

The second idea to achieve multiple resistance states relies on the realization of an MTJ whose free layer presents a granular structure (Fig. 1.15a). This feature could be exploited to gradually switch the free layer grain by grain using STT or SOT effects. To do this, an analysis of the switching probability must be done as function of the voltage pulse characteristics (an example is given in Fig. 1.15b from ref [137]). Generally, for a switching probability lower than one, the same percentage of the free layer is expected to reverse its magnetization. In this way, the TMR, used as reading mechanism, would give a series of intermediate values depending on the ratio of the free layer magnetization in parallel/antiparallel configuration as shown in Fig. 1.15c. In chapter 4, we

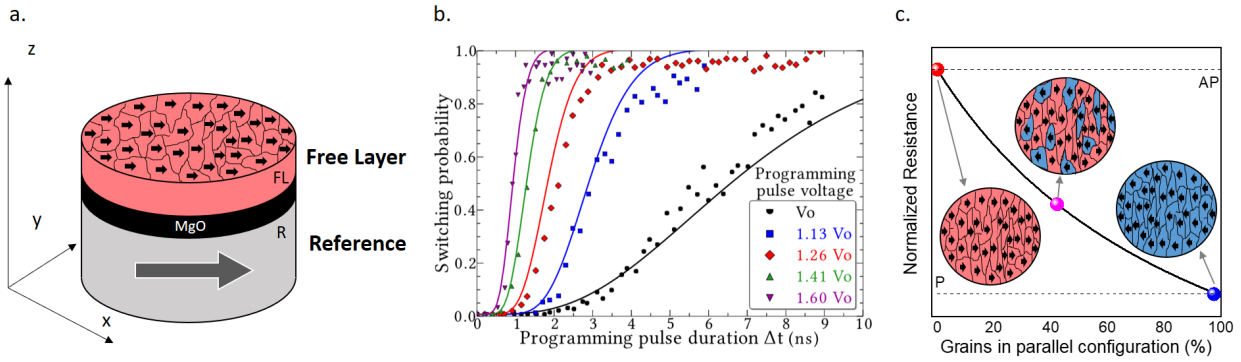

Fig. 1.15: Memristor based on granular free layer | **a.** Schematic of the device. **b.** .Example of switching probability for an in-plane magnetized MTJ (from ref [137]). **c.** Variation of the resistance with the gradual switching of the grains.

detail the realization of a structure composed of ferromagnetic grains surrounded by non-magnetic boundaries (preferably insulating). This structure, similar to the one that have been developed for a long time for magnetic recording media and integrated with a reference layer in an MTJ structure, would be comparable to an array of MTJs connected in parallel. Also in this case, the STT or SOT effect could be used to statistically switch a certain number of grains so that the TMR would be again dependent on the ratio between parallel and antiparallel grains.

The material development and the electrical results will be detailed in chapter 4 for both kinds of devices.

Chapter 2

Experimental techniques: fabrication and characterization

Contents

This chapter describes the experimental techniques used in this thesis. The standard procedure includes a deposition step followed by magnetic and electrical characterizatioon at full sheet film level and a nano-fabrication process followed by magnetic and electrical characterization at device level.

2.1 Magnetic stack deposition

The set of the samples described in this thesis was deposited at Spintec by Stephane Auffret with a magnetron sputtering technique. This particular physical vapor deposition technique is based on the induction of a plasma with heavy and inert materials such as Ar or Xe. After the creation of an high vacuum (between 10^{-6} and 10^{-9} mbar), a controlled pressure system let the gas enter in the chamber with a pressure in a range of 10^{-3} mbar. An high voltage applied between a cathode, usually placed behind the target, and an anode, usually grounded to the chamber, allows the ionization of the gas. In this way, the heavy material ions, attracted towards the cathode, collide with the target material allowing its particles to be ejected into the vacuum with a controlled kinetic energy in order to reach the substrate. The peculiarity of this technique stands in the magnetic field (in this case DC) applied into the chamber that confines the electrons in relatively small area close to the target. This allows the creation of a denser plasma (increasing the deposition rate), and improves the quality of the deposited films by avoiding the interference of the electrons with the substrate or with the target particles during the deposition.

The machine used for the samples described in this manuscript is shown in Fig. 2.1a. It presents a loadlock chamber (LL) connected to the exterior to insert the substrates (maximum 25 wafers of 4 inches size), a main chamber (MC) for the material deposition and a treatment chamber (TC) for oxidation and etchings steps. Between them, a chamber containing the main robotic arm allows the transfer of the substrates between the three chambers. All the chambers work at RT and two cryopumps ensures the vacuum around $8x10^{-8}$ mbar. The treatment chamber is used to oxidize the deposited materials in a controlled environment and without taking out the sample from the machine. The realization of the oxide layers (as for example MgO) are made by depositing the metallic film (Mg) in the main chamber and then controlling the oxygen pressure in the treatment chamber. The main chamber presents 12 separated targets of 125mm of diameter and a secondary mechanical arm to move the sample under each of them. The separation between targets does not allow the co-sputtering of two materials at the same time. Moreover, while the deposition of a uniform thin film (with a non-uniformity of 10% to 15% on the borders of a 4-inches wafer) is made by placing the sample right below the target with a rotating holder (see Fig. 2.1b), the deposition of wedges of materials is made possible by slightly displacing the sample off axis and stopping the rotation (see Fig. 2.1c). With this technique, it is possible to let the thickness of a layer varying across the wafer by a maximum factor of two. This technique is widely used to analyze the magnetic properties variation with the thickness of a layer in a fast and efficient way.

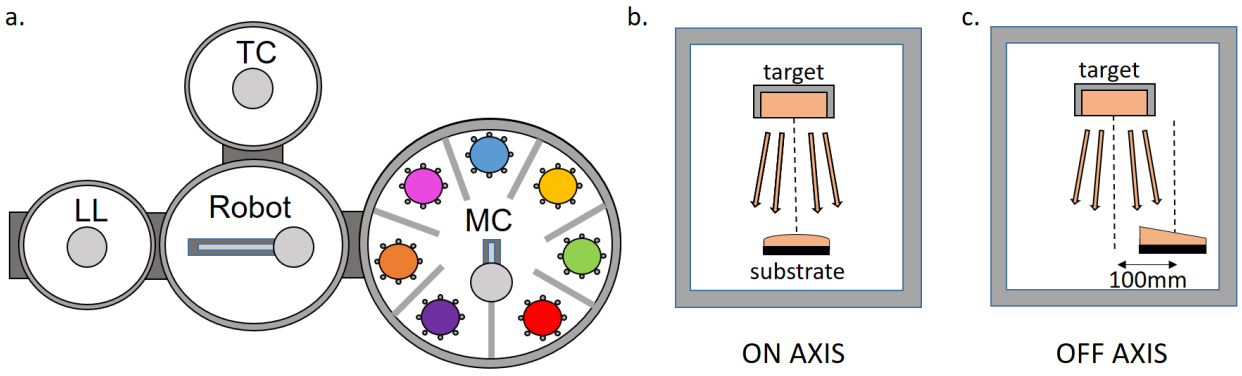

Fig. 2.1: Magnetron sputtering tool | **a.** Scheme of the tool with the loadlock (LL), main chamber (MC) and treatment chamber (TC). **b.** Scheme of the on axis deposition. **c.** Scheme of the off axis deposition for creation of wedges.

2.2 Magnetic material and transport characterizations at wafer level

The material optimization for the magnetic stacks is performed through the characterization of full sheet films deposited as in the previous section. Here it follows a brief description of the working principles of the two main tools used for this purpose.

2.2.1 Vibrating Sample Magnetometer (VSM)

This tool, widely used in the spintronic community, bases its working principle on the Faraday's law for which a variation of the magnetic flux in a circuit creates an electromotive force. In the case of a VSM, the magnetized sample is placed in a constant magnetic field and it is put in a vibrating motion at constant frequency along the z direction (see Fig. 2.2a). The variation created in the magnetic flux induces a voltage in the nearby pick-up coils that is measured with a lock-in circuit using the vibrating frequency as reference. A magnetic field sweep is used to realize measurements of full magnetic hysteresis loops.

The tool used for the measurements presented in this manuscript is from MicroSense®. With a sensitivity of 10^{-6} emu, this technique allows a quite accurate determination of magnetic parameters such as saturation magnetization, anisotropy field and coercive field. The possibility of rotating the sample holder creating a certain angle with respect to the field direction allows to perform hysteresis loops out-of-plane, in-plane and at different intermediate polar and azimuthal angles. This property is widely used in Chapter 3.

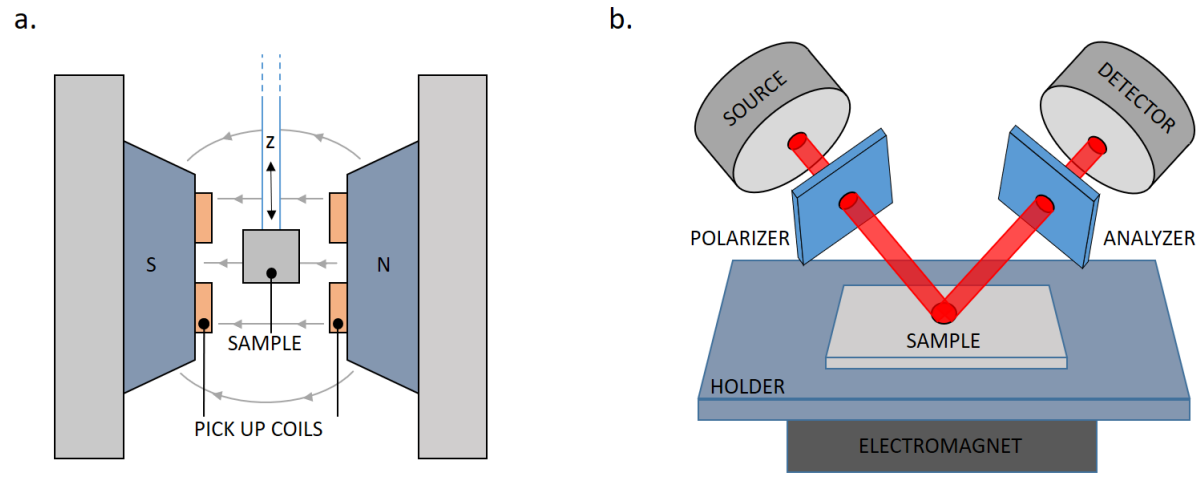

Fig. 2.2: Schematics of VSM and MOKE tools | **a.** Schematic of a vibrating sample magnetometer tool. **b.** Schematic of a magneto-optical Kerr effect tool.

2.2.2 Magneto-optical Kerr effect

The Kerr effect, discovered in 1876 [138], describes the polarization and intensity variation of a light beam reflected on a magnetized sample. A laser source emits a light that is linearly polarized with a proper polarizer. The reflection of this light on a magnetized surface can have three main effects or a combination of them: the polarization becomes elliptic (Kerr ellipticity), the plane containing the polarization is rotated (Kerr rotation) and the polarized amplitude varies. The reflected beam then passes through an analyzer filter before reaching a detector. Depending on the nature of the magnetized sample, three kinds of Kerr effect can take place. Respectively polar, longitudinal and transversal for out-of-plane, in-plane with field applied along the plane of incidence of light and in-plane with field applied perpendicular to the plane of incidence. From an analysis of

the three parameters it is possible to get information on the magnetization of the sample. The use of an electromagnet allows to perform magnetic hysteresis loops.

The tool used for this thesis is a NanoMOKE3® from Durham Magneto Optics. A simple schematics of the tool is presented in Fig. 2.2b. The laser has 660nm of wavelength with 300μm spot and the maximum applied field is 400mT. The presence of an automatized sample holder and the relatively short time needed for the measurement (much shorter than for the VSM) allow to perform wafer mapping of the magnetic properties. Despite the poorer precision in the extraction of the magnetic parameters, this tool is widely used in chapter 4, where single or double wedges of materials are deposited in order to find the suitable magnetic properties.

2.2.3 Current in-plane tunneling magnetoresistance(CIPTMR)

This technique is widely used in the MRAM community to test the transport properties of the magnetic stack without the need to pattern it. The working principle consists in a simple four probe measurement of the resistance of the sample in which the external probes send a current through the full sheet film stack and the two internal probes measure the resulting voltage as in Fig. 2.3a. It turns out that the final resistance depends on the physical spacing between the probes as shown in Fig. 2.3b. In particular, for relatively small distances between them, the current passes in the top metallic magnetic electrode (T) measuring then its resistance (R_T). By increasing the distance between probes, the current starts gradually to tunnel through the oxide barrier up to the moment in which, for larger spacing, the current flows in the top (T) and in the bottom (B) electrodes in proportion to their respective sheet resistances (the two sheet resistances are in parallel). The analysis of the resistance variation versus the distance between probes gives as result a quite precise determination of the tunneling rate through the oxide barrier (which is measured by its resistance*area product $R \times A$), of the top electrode sheet resistance (R_T) and of the bottom electrode sheet resistance (R_B). This can be used, thanks to the use of an additional electromagnet, to determine the TMR of the stack by measuring the change in $R \times A$ product in the case in which the two magnetizations are parallel and antiparallel. With this system, it is possible to extract the $R \times A$ product at wafer level that is extremely useful to check the quality of the stack before starting the tedious patterning process.

The tool used in this work is a CIPTech® M200 of CAPRES. Several kinds of probes can be mounted depending on the needs. The saturation field is 19mT and 150mT respectively for in-plane and out-of-plane components. This tool was used for the material development sections of the devices presented in this manuscript.

2.2.4 Transport measurements under rotating field

In this kind of measurements the quasi-static variation of magnetization direction is detected by measuring the planar Hall resistance on a full sheet film. The planar Hall effect (PHE) describes the anisotropic magnetoresistance variation caused by an external magnetic field in a Hall geometry [46]. In this way, the resistance reaches its maximum when the current is flowing parallel to the magnetization direction and gradually decreases for intermediate angles giving rise to an oscillatory behavior.

A schematic of the setup used in this work is shown in Fig. 2.3c. The sample is mounted on a holder and inserted between the poles of an electromagnet so that the field direction results in the plane of the sample. The sample holder can rotate with frequencies up to 10Hz of a maximum angle of 3π. To measure the resistance, four wires are bonded on the sample in a way to send a current through two contacts and measure the voltage on the other two.

Generally, the magnetization direction results from its particular dynamics under the influence of applied field, its anisotropy field, its damping. If the field is much larger than the anisotropy field, then the magnetization can be considered as aligned with the field. The magnetization direction forms an angle ϕ_M with the current direction. By mechanically rotating the sample holder, the field direction and therefore the magnetization direction varies yielding a change of resistance due to the

planar Hall effect of the film (which is associated with its anisotropic magnetoresistance). It turns out that the resistance follows a dependence given by

$$R_{PHE} = \frac{\Delta R}{2} sin(2\phi_M) \tag{2.1}$$

where ΔR is the PHE magnetoresistance [139]. An example of a resulting resistance measurement is shown in Fig. 2.3d.

This method will be used in chapter 3 and compared to a similar measurement done at device level.

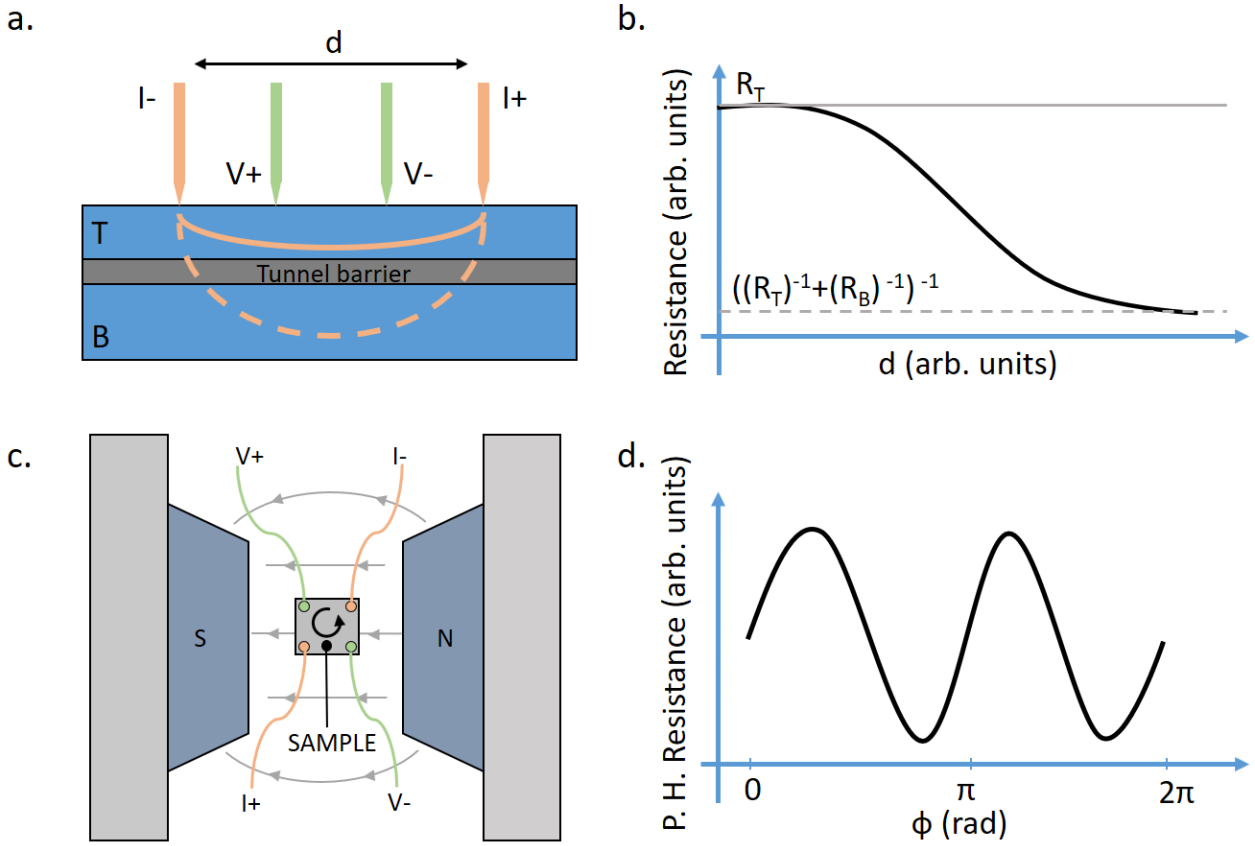

Fig. 2.3: Schematics of CIPTMR and PHE tools | **a.** Schematic of a CIPTMR measurement principle. **b.** Example of resistance variation with the distance between probes. **c.** Schematic of a planar Hall effect tool. **d.** Example of planar Hall resistance dependence on the angle ϕ.

2.2.5 Lorentz TEM

The Lorentz mode of standard Tunneling Electron Microscopy (TEM) is widely used to image magnetic domains and domain walls down to a resolution of 2nm to 20nm. The working principle is based on the Lorentz force F_L the the electron beam feels when passing through the magnetic medium. In fact, the magnetic field $\vec{B}$ and/or the electric field $\vec{E}$ locally created in the material act on the electron beam with a force $F_L = -e(\vec{E} + \vec{v} \times \vec{B})$, where $\vec{v}$ is the velocity of the electron. This deflection of electrons can then be detected mainly in two different modes. In the Foucault mode, as in Fig. 2.4a, the aperture is displaced while mantaining the focus, so to favour the transmission of only one of the two deflected beams. In this way, the image obtained reflects the configuration of the domains in the structure. Despite the good resolution of such technique, the application of a varying exernal field in order to observe the domain structure evolution, influences relevantly the beam making very hard the imaging of the same spot. In the Fresnel mode, instead, the aperture allows the transmission of both the deflected electron beams. In this way, in case

of in-focus as in Fig. 2.4b, the two beams perfectly match originating a zero contrast image. In order to obtain information in this mode, the beam is defocused (over or under-focused) in a way to obtain a displacement of the two images (Fig. 2.4c). This creates, close to a domain wall, a contrast due to the overlapping or the spacing of the two beams. The resulting image maps the domain walls structure in the sample. Differently from the Foucault mode, it is possible to image with an important contrast the evolution of the magnetic configuration due to an external field but, due to the defocus of the beam (necessary to obtain a contrast), the overall resolution results lower than the one in Foucault mode. Interestingly, from the imaging with this technique it is possible to reconduce quantitatively to the direction of the magnetization through the use of the transport of intensity equation (TIE) [140].

These techniques will be used in Chapter 3 to have a better understanding of the magnetic behavior of the free layer.

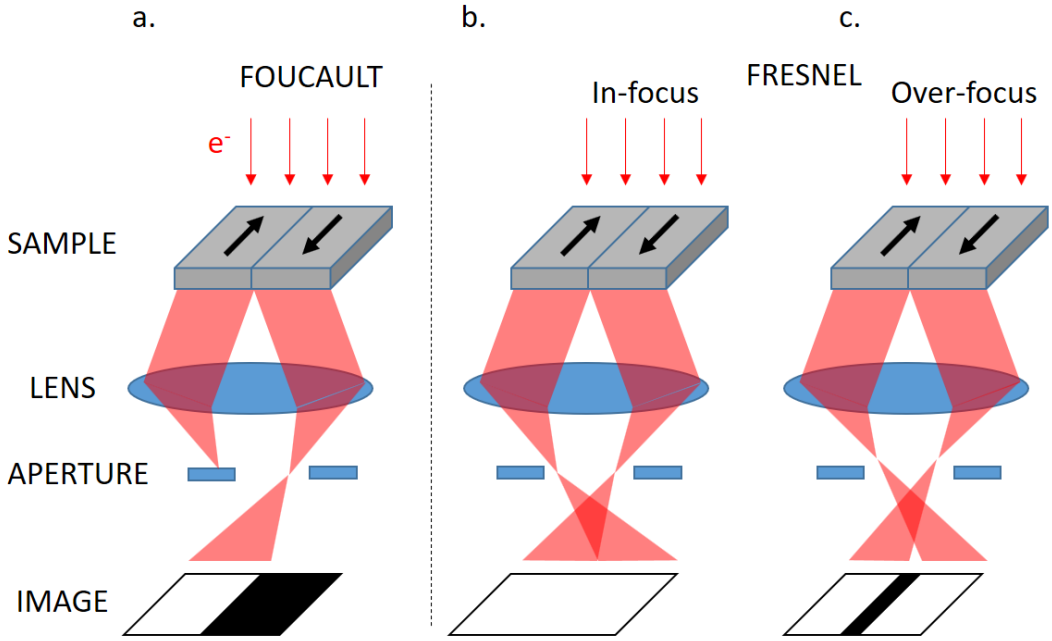

Fig. 2.4: Schematics of Lorentz TEM | **a.** Schematic of Focault mode. **b.** Schematic of Fresnel in-focus mode. **c.** Schematic of Fresnel over-focus mode.

2.3 Nano-fabrication process

The nano-fabrication process used in this thesis was previously developed in the MRAM group at Spintec and always under improvements or modifications according to the status of the cleanroom tools. It is based on a 4-step lithography process including a first step of e-beam lithography and 3 of optical lithoghraphy. Its purpose is to create an array of nano-sized pillars connected on top and bottom to metallic electrodes shaped into much bigger pads in order to be easily contacted.

The bottom contact material and the total magnetic stack is deposited on a 2" or 4" wafer of SiO_2 as shown in the schematic of Fig. 2.5a. The sample is annealed at optimized conditions to improve the magnetic properties (more detailed description of the material development can be found in the next chapters since it is specific to different cases). A 150nm thick layer of Ta is then deposited on the top of the stack.

The first lithographic step purpose is to draw the pillar shape into diameters between 20nm and 300nm (depending on the needs) (Fig. 2.5b). Such small features are defined with an e-beam tool that creates an array of 168 pillars per die. A deposition of 20nm of Cr (Fig. 2.5c) and a following lift-off create a Cr pattern on the Ta layer as in Fig. 2.5d. This is used as mask in the following reactive ion etching step (RIE) in which a combination of SF_6 and Ar plasma etch both physically

and chemically the Ta layer. A thin Ru layer is used as etch stopper by following a signal coming from a reflectometer. The result is the formation of a Ta nano-sized pillar as in Fig. 2.5e. Its form, very sensitive to under and over-etching, is fundamental for a good shaping of the magnetic stack since it is used as physical mask in the successive ion beam etching step (IBE). The tool exploits an Ar-based plasma to physical etch the magnetic stack. The angle of incidence of the ion beam on the substrate turns out to be fundamental to obtain a good shape, to avoid the re-deposition of the etched materials on the pillar walls and to avoid degrading the magnetic properties of the stack. For this reason, the recipe for this step is in continuous evolution to try to obtain the best results depending on the magnetic stack. The etching step, followed through a secondary ion mass spectrometer (SIMS), is stopped when reaching the bottom contact material as in Fig. 2.5f.

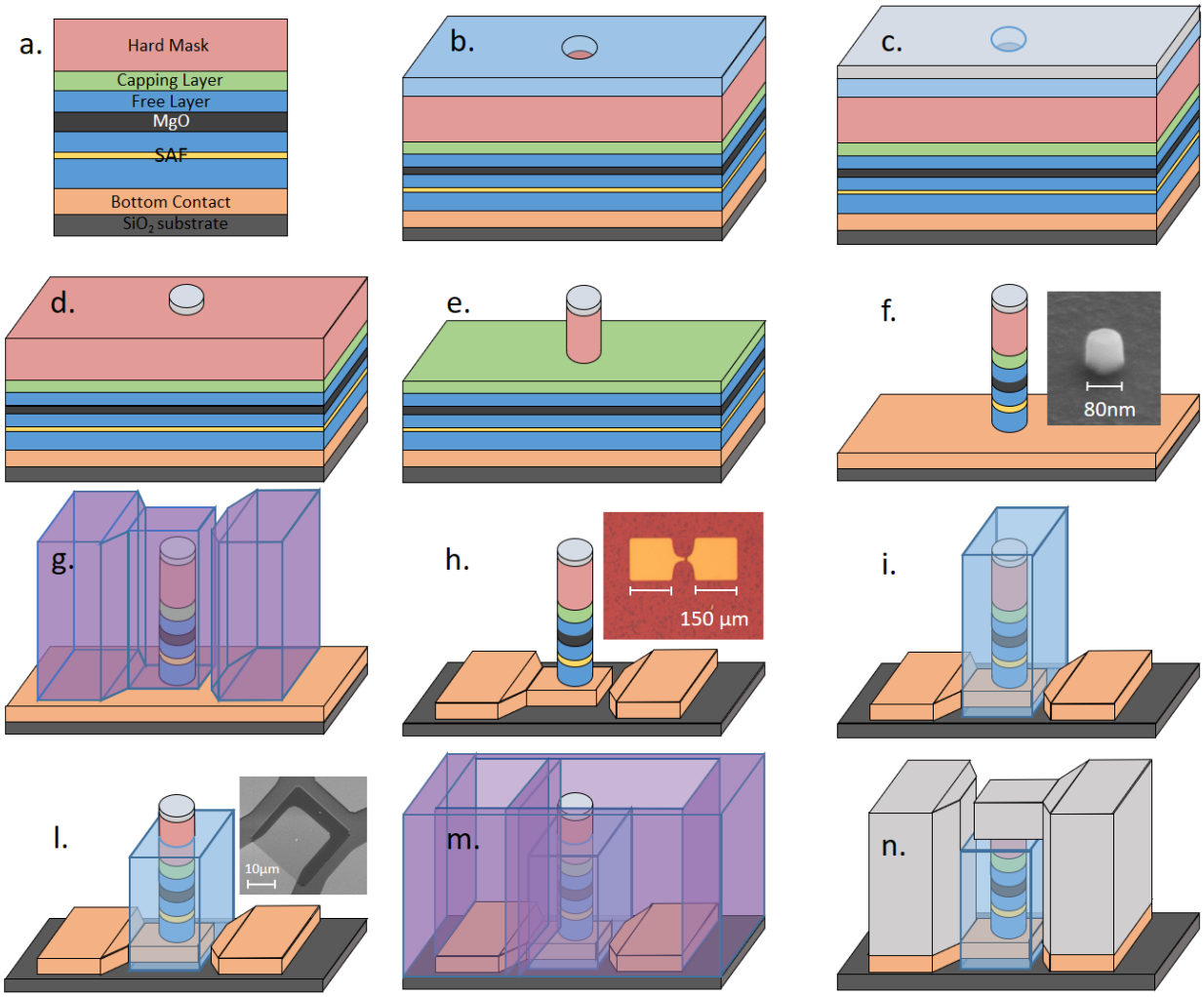

Fig. 2.5: Nano-fabrication steps | **a.** Schematic of a classical magnetic stack deposited for fabrication. **b.** E-beam lithography result after development. **c.** Depositon of 20nm of Cr by evaporation technique. **d.** Cr pattern after lift-off. **e.** Ta pillar resulting from an RIE etching. **f.** Full magnetic pillar resulting from an IBE etching and SEM image in the inset. **g.** UV lithography result after development. **h.** Bottom electrode resulting after an RIE etching and optical microscope image in the inset. **i.** Accuflo patterning after UV lithography and RIE etching. **l.** Thinning of the Accuflo layer with RIE etching ans SEM image in the inset. **m.** UV lithography result after development (with negative resist). **n.** Final device after deposition of the top electrode of 300nm of Al and following lift-off.

A second lithography aims to shape the bottom contact in a 150μm side pad. To do this, an UV lithographic tool is used with a positive resist to create the shape in Fig. 2.5g (note that the scale is not realistic on purpose since the size of the pad is much bigger than the pillar one). The

bottom contact is the etched in a subsequent RIE step giving a result shown in Fig. 2.5h.

At this point, an insulating polymer Accuflo [141] is deposited on the sample with the double purpose of protecting the pillar from external damaging or oxidation and separate the bottom contact from the top one. With an additional step of optical lithography and RIE etching, the polymer is shaped as in Fig. 2.5i. To create the contact between the pillar and the top electrode, an additional step of RIE is used to thin down the polymer and reach ideally the situation in Fig. 2.5l where only part of the top Ta layer is exposed. This step is delicate since an over-etching of the polymer could create a short contact between top and bottom electrode while an under-etching could create an open contact. For this reason the etching rate is carefully calculated from the previous RIE step and used to etch the needed quantity of polymer.

A final step of UV lithography defines the top electrode form. On this step, a negative resist is used as in Fig. 2.5m. In this way, after the deposition of 300nm of Al as top contact, the lift-off gives as result the final device as in Fig. 2.5n.

The entire process is done in Plateforme Technologique Amont (PTA) [142].

2.4 Device characterisation

The finalized devices are electrically characterized with an electrical prober already built and optimized since several years. In this section, the setup and the measurement techniques used in this work are briefly described.

2.4.1 Measurement setup

The setup schematics is shown in Fig. 2.5. The top and bottom electrodes of the device are contacted with two microprobes connected to a bias tee. On the dc part of the bias tee, a combination of a sourcemeter and a digital multimeter allows respectively the emission of a bias current and the measurement of the voltage for the measurement of the resistance of the device. On the ac side of the bias tee is set a pulse generator able to send pulses with 200ps raise time. The train of pulses is designed by an arbitrary waveform generator that is triggered with the digital multimeter. The same waveform generator is used to send a signal to the power supply of an electromagnet placed closed to the device. In this way, field sweeps perpendicular and in the plane of the wafer allows the measurements of resistance loops (up to 0.3T).

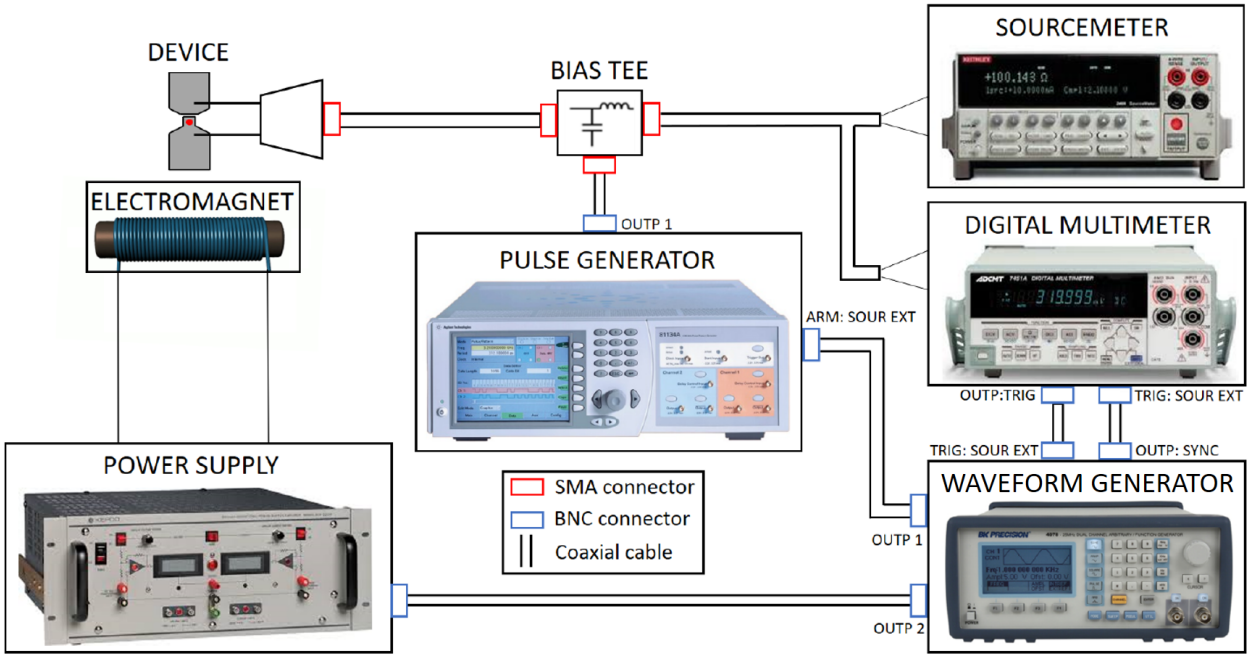

Fig. 2.6: Electrical characterization setup |

Finally, an automatized sample holder allows the measurements of the few thousands of devices present in a standard wafer. The whole setup is controlled with matlab codes for the implementation of different kinds of measurements.

2.4.2 Yield measurement

The first measurement usually performed on a wafer consists in the estimation of the magnetic parameters for the totality of the devices. The resistance measurement during the field sweep shows up as an hysteresis loop from which values like TMR, coercive field and field offset are extracted. Those are compared to the characteristics of the magnetic stack previously studied in full sheet film to try to identify possible problems which might have occurred during the fabrication process. For example, by analyzing the resistance value with respect to the pillar size and the relative TMR it is possible to understand if any re-deposition occurred during the IBE etching step creating shunt resistances. Fig. 2.7 a and b show a classical example of TMR and coercive field mappings of a 4-inches wafer. Each point represents a device plotted in the x-y plane of the wafer. This kind of spacial mapping is useful to identify variations of the magnetic properties as a function of the location on the wafer. In particular, in presence of a wedge, the location of the devices with respect to the expected magnetic properties can be easily identified.

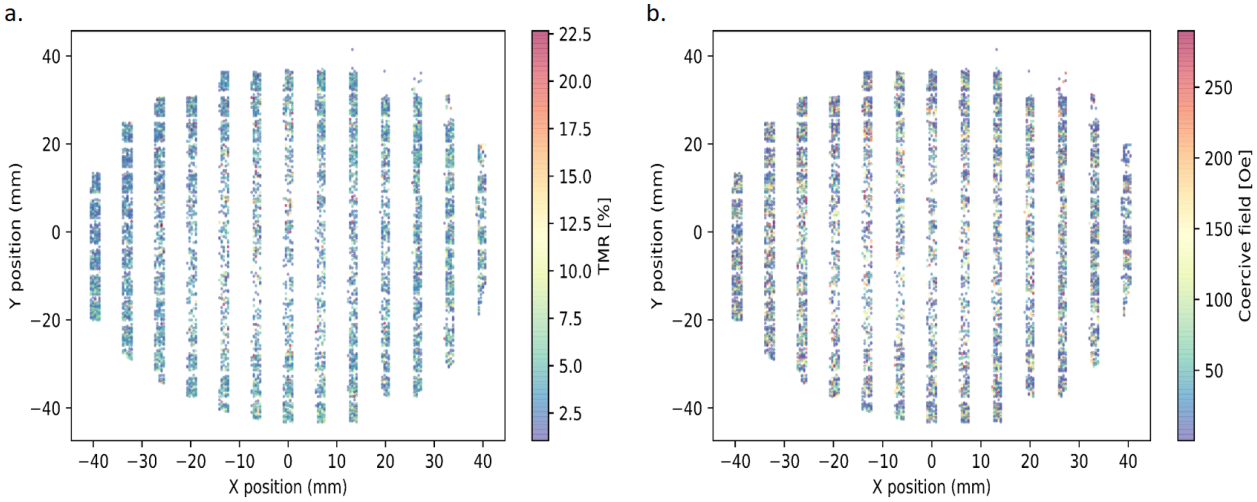

Fig. 2.7: TMR and Coercive Field mappings | **a.** Mapping of the TMR values of the devices in a 4-inches wafer **b.** Mapping of the coercive field values of the devices in a 4-inches wafer.

2.4.3 Measurements under field : angular dependence and rotating field

For the case of in-plane magnetized MTJs, a set of four coils surrounds the device so that the two pairs of coils generate a field in two perpendicular directions in the plane. This system is usually used to measure easy and hard axis in binary in-plane MTJs by connecting only a couple of coils per time (each couple has its own power supplier). In this work the all four coils are exploited to perform hysteresis loops at different in-plane angles. This is done just by playing with the x and y components of the field generated by the two pairs of coils. To generate a field of amplitude A along an in-plane angle α, the couple of coils generating the field along the x direction is supplied with a current to produce a field H_x=A cos(α) and the y coils to produce a field H_y=A sin(α). The amplitude A is then swept to generate the field loop.

With the same system and by introducing a time dependent variation of the field amplitude in each couple of coils, it is possible to apply a rotating field of constant amplitude A. The two synchronized signals, produced by the waveform generator, are respectively H_x=A cos(ωt) and H_y=A sin(ωt) where t is the time and ω is the angular velocity so that the frequency of the rotating field is f = $\omega/2\pi$. The main limitation in terms of frequency (maximum 5Hz) comes from

the overheating of the coils that makes the total field amplitude to be reduced. Those kind of measurements are used in Chapter 3 to test the in-plane isotropic magnetic properties at device level and to compare them to the ones performed at wafer level.

2.4.4 Measurements under STT

A classical measurement to test the STT efficiency of an MRAM cell is the phase diagram where the device is continuously switched by varying field and pulse parameters. Despite this, the complexity and the non-binary nature of the devices presented in this work does not allow an easy comprehension of the resulting diagram. For this reason, the STT effect is mainly observed in those devices thanks to the application of train of pulses specifically designed. In this way, the effect of such pulses on the device can be understood from the time evolution of the resistance. For each experiment described in the next chapters, the parameters relative to train of pulses will be detailed.

2.5 Conclusions

In conclusion, all the experimental methods shortly presented here have been used all along the work described in this manuscript. In the following chapters, the results relative to material optimization, nanofabrication process and electrical characterization will be presented for each of the devices studied.

Chapter 3

Memristor based on the angular variation of TMR

Contents

In this chapter we propose an original concept of memristive device suitable for scalable and large scale integration applications. A full macrospin model describes the device functionalities and working regions thanks to an additional dissipative term in the LLG equation. The materials development section describes the challenges in the realization of the device and the final results are shown in the electrical characterization section.

3.1 Introduction

As already anticipated, the first memristor concept investigated in this thesis relies on the TMR dependence on the relative angle between the magnetization of a free layer and of a fixed reference layer in an in-plane MTJ. In this case, the ability to stabilize the magnetization of the free layer of such MTJ along different in-plane directions with respect to the fixed analyzer magnetization, is the key to achieve the multilevel resistance device. The main challenge is to realize such magnetic medium and to integrate it in a complete magnetic stack. Furthermore, the STT effect coming from an additional perpendicular polarizer is introduced to discretely rotate the magnetization of such isotropic free layer though the application of properly designed pulses.

In section 3.2 of this chapter, the isotropic properties of the free layer are simulated with a macrospin code implementing the LLG equation with an additional dissipative term. The STT contributions from both in-plane analyzer and out-of-plane polarizer are first studied separately and then combined in order to find the proper working regions of the device to be exploited for memristive applications.

In section 3.3, the material development for the realization of the isotropically coercive free layer first, and then the other parts of the magnetic stack, is described and the results compared to the expected ones from the simulations. The full magnetic stack is finally presented.

In section 3.4, the electrical characterization results are shown for patterned devices. Both field-driven and current-driven experiments are performed to fully understand the functionalities of the device.

A short section 3.5 is dedicated to the effect of operating temperature on the device properties, while in section 3.6, a second full magnetic stack is presented in order to exploit a different working region. The material development and the electrical results of this last device are described in the same section.

Finally in section 3.7, the results are summarized to give a full overview of the device properties.

3.2 Macrospin model based on a dry friction - like term

In classical mechanics, the concepts of viscous and dry frictions are frequently used in the general equation of motion. According to Newton's law, the position $\vec{r}$ of a body of mass m under the action of a force $\vec{f}$ follows the equation

$$m\ddot{\vec{r}} = \vec{f} - \alpha\dot{\vec{r}} - \beta\frac{\dot{\vec{r}}}{|\dot{\vec{r}}|} \tag{3.1}$$

where α and β are positive damping constants. The viscous friction is a term proportional to the velocity of the body $\dot{\vec{r}} = \frac{\partial\vec{r}}{\partial t}$. The dry friction term, independent of the velocity and against the motion, is often used to describe the friction between solids. Similar to mechanics, the dynamics of magnetization $\vec{m}$ in ferromagnets also involves various mechanisms of energy dissipation. In the LLG equation 1.3.1, usually written as

$$\frac{\partial\vec{m}}{\partial t} = -\gamma(\vec{m}\times\mu_0\vec{H}_{eff}) + \alpha_G(\vec{m}\times\frac{\partial\vec{m}}{\partial t}) \tag{3.2}$$

the second term, the Gilbert dissipative term, is dependent on the "magnetization velocity" as a viscous friction in mechanics. The LLG Eq. 3.2 is extensively used to perform micromagnetic simulations [143]. In some cases, an extra source of dissipation can be added to the system by introducing specific defects such as pinning sites or local variation of material parameters (such as anisotropy or magnetization). Another approach consists in introducing in the LLG equation a velocity-independent damping that, as in mechanics, accounts for the presence of distributed defects (for instance, associated with a distribution of anisotropy axes or of exchange interactions). The LLG equation then contains an extra dry friction term

$$\frac{\partial\vec{m}}{\partial t} = -\gamma(\vec{m}\times\mu_0\vec{H}_{eff}) + \alpha_G(\vec{m}\times\frac{\partial\vec{m}}{\partial t}) + \beta\frac{\vec{m}\times\frac{\partial\vec{m}}{\partial t}}{|\vec{m}\times\frac{\partial\vec{m}}{\partial t}|} \tag{3.3}$$

In the frame of this modified LLG equation, Kittel and Galt [144] and Malozemoff and Slonczewski [145] studied the pinning of domain walls during their motion in continuous thin films. With similar purposes, Baltensperger and Helman [146] used the additional dry damping to explain the phenomenon of hysteresis, that is linked to dissipation but not through the magnetization velocity. This model allowed studying the influence of magnetic friction on the linewidth of ferromagnetic resonance (FMR) [147]. More recently the model has been implemented in micromagnetic simulations to study the field and current-driven domain wall motion in nanostrips with defects [148] [149] [150]. In the usual LLG Eq. 3.2, the magnetization stops moving when the magnetization vector is aligned with the effective field $\vec{H}_{eff}$ since in this case, there is no more torque acting on the magnetization $|\gamma(\vec{m}\times\mu_0\vec{H}_{eff})| = 0$. In contrast, the additional dry friction term in Eq.3.3 generalizes this static equilibrium condition to

$$|\gamma(\vec{m}\times\mu_0\vec{H}_{eff})| < \beta \tag{3.4}$$

The dynamics of the magnetization itself is affected and is described by a dynamic effective damping $a = \alpha_G + \frac{\beta}{v}$ with $v = |\frac{\partial\vec{m}}{\partial t}| = |\vec{m}\times\frac{\partial\vec{m}}{\partial t}|$. Hereafter, we used the modified LLG Eq.3.3 including a dry friction term to analyze the magnetization dynamics of an isotropic magnetic thin film under either a static (3.2.1) or an in-plane rotating magnetic field (3.2.2). The analytical predictions are compared with the results obtained by numerical integration of the LLG equation.

The simulations shown in this chapter use the parameters as in Table 3.1.

3.2.1 Static equilibrium under in-plane field

The system considered in this study is a ferromagnetic thin film of thickness l lying in the x-y plane. The magnetization is supposed to be uniform and subject only to the demagnetizing field and a static in-plane applied field. The effective field in the LLG Eq.3.3 is simply given by

M_S	K_u	α_G	l	T
$10^6 A/m$	$0 J/m^3$	0.04	$4nm$	$0K$

Table 3.1: Simulation parameters

$$H_{eff} = [H_{app}cos(\varphi_H) \qquad H_{app}sin(\varphi_H) \qquad - M_S cos(\theta_M)] \tag{3.5}$$

where $\theta_{M,H}$ and $\varphi_{M,H}$ are, respectively, the polar angle and the azimuthal angle of the magnetization (M) and the external field (H). Considering an in-plane initial magnetization ($\theta_M = \pi/2$) and a motion within the x-y plane, the equilibrium condition Eq.3.4 reduces to

$$|sin(\varphi_H - \varphi_M)| < \frac{\beta}{\gamma \mu_0 H_{app}} \tag{3.6}$$

Both the applied field amplitude and the dry friction coefficient define the limit angle of a sector in which the magnetization can be stable at equilibrium. Without dry friction, the magnetization is perfectly aligned with the applied field as expected. In contrast, with dry friction, two regimes are identified with respect to a threshold field value $H_{TH} = \frac{\beta}{\gamma \mu_0}$, as shown in Fig. 3.1a (where $\phi = \varphi_H - \varphi_M$) in which, for each value of the applied field, the limit angle of this sector of stability of the magnetization is plotted. For low applied fields $H_{app} < H_{TH}$, the amplitude of the torque acting on the magnetization is not large enough to initiate the motion (mathematically, the value of the right-hand term of Eq.3.6 is larger than 1). In this case, the magnetization is stable along any in-plane direction (Fig. 3.1b, left).

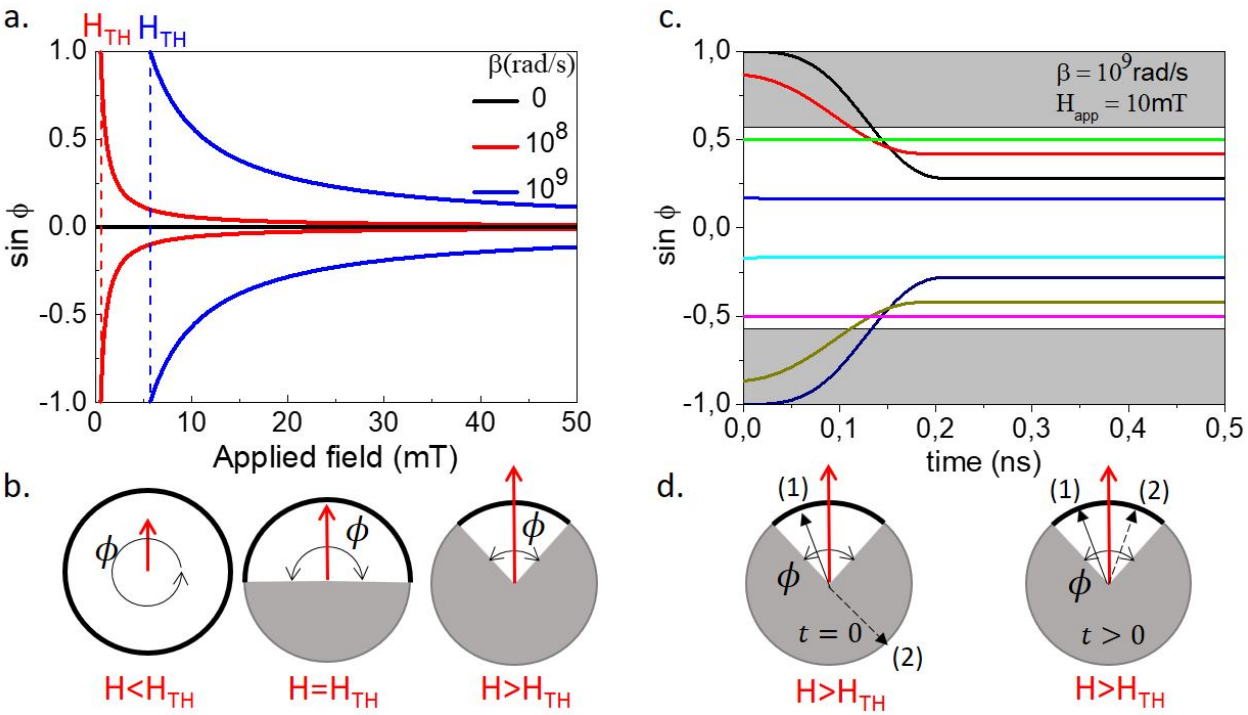

Fig. 3.1: Static equilibrium under in-plane field | **a.** Analytical limit of the sector of stability under in-plane static field for several values of dry friction coefficient β. **b.** Schematics of the evolution of the stability region (in white) with field amplitude. **c.** Macrospin time evolution of magnetization with different initial angles under a static magnetic field. The white region corresponds to the analytical sector of stability. **d.** Schematics of initial (left) and final (right) positions of magnetization for initially stable and unstable cases (respectively, 1 and 2).

At the critical field H_{TH}, the torque created by the field is balanced by the friction within the whole half plane around the field direction (white region in Fig.3.1b the center for which the right-hand term of Eq.3.6 is equal to one). This sector of stability then reduces upon increasing the field amplitude (Fig. 3.1b right for which the right-hand term of Eq. 3.6 is less than 1). In Fig. 3.1c, the time evolution of magnetization for different initial angles is shown for an applied field of 10 mT and $\beta = 10^9 rad/s$. Inside the stability sector (white region in Fig. 3.1c), whatever the direction of the magnetization, Eq.3.6 is valid and no motion of the magnetization can occur. This means that if the initial magnetization is already inside the stability sector (whose amplitude depends on the applied field as shown by Eq.3.6) it will remain stable (as the green, blue, cyan, and magenta cases in Fig. 3.1c and case (1) in Fig. 3.1d). In the opposite case, when the initial magnetization is outside the stability sector (in gray in Figs. 3.1c and 3.1d), the magnetization feels a torque greater than the friction for which it initiate a relaxation towards the limits of the cone as for the other cases in Fig. 3.1c and case (2) in Fig. 3.1d. The exact final position depends on the relative initial magnetization angle with respect to the field angle. The larger the initial angle with respect to the field direction, the larger the torque, the higher the initial angular velocity of the magnetization, and the closer the final position of the magnetization will be to the field. The macrospin simulations confirm that the stability limit between the torque of a static field and the dry friction is given by Eq.3.6.

Finally, note that the effect described in this paragraph does not depend on the absolute initial direction of the magnetization. In fact, the images in Fig. 3.1 are represented as a function of the difference between the field angle and the magnetization angle to emphasize that the results are invariant under rotation of magnetization and field in the plane. In particular, despite the absence of any anisotropic term in the different energy terms involved, the threshold field due to the dry friction results in a coercive field exhibiting isotropic characteristics in the x-y plane. For any in-plane initial magnetization direction, the same field amplitude in the opposite direction is needed to induce magnetization motion.

3.2.2 Magnetization dynamics under in-plane rotating field

A second case of interest consists of applying an in-plane rotating field of amplitude H_{rot}, angular velocity ω_{rot} , and initial direction at t=0 given by φ_{rot}. This field can induce an in-plane rotation of the magnetization provided the torque due to the field is larger than the dry friction torque. The effective field from Eq. 3.3 becomes

$$H_{eff} = [H_{rot}cos(\omega_{rot}t + \varphi_{rot}) \qquad H_{rot}sin(\omega_{rot}t + \varphi_{rot}) \qquad - M_S cos(\theta_M)] \tag{3.7}$$

In the absence of dry friction, the magnetization would follow the direction of the rotating field after a transient regime with a small delay dependent on the values of the Gilbert damping, the field amplitude, and the frequency of the rotating field. The effect of the dry friction term shows up, similar to the previous case, as a significant increase of the threshold field $H_{rot_{th}} = \frac{\beta}{\gamma\mu_0} + \frac{\alpha_G\omega_{rot}}{\gamma\mu_0}$ separating two regimes: the low field regime where the torque is not sufficient to overcome the friction, and the high field regime for which a stationary rotation of the magnetization is induced. In the first case, the torque induced by the rotating field is balanced by the dry friction torque resulting in a stable magnetization state in any position in the plane. In the second case, for fields higher than a threshold, the magnetization, after a transient regime, starts to follow the rotating field (Fig. 3.2a) with a drag angle different from zero (Fig. 3.2b).

In this dynamic stationary condition, where $\varphi_H = \omega_{rot}t + \varphi_{rot}$ and $\varphi_M = \omega_{rot}t + \varphi_{rot} - \phi$, the final drag angle can be written as

$$sin(\varphi_H - \varphi_M) = sin(\phi) = \frac{\beta}{\gamma\mu_0 H_{rot}} + \frac{\alpha_G\omega_{rot}}{\gamma\mu_0 H_{rot}} \tag{3.8}$$

As in the previously discussed static case, this angle is linearly dependent on the dry friction parameter β and inversely proportional to the amplitude of the rotating field. To this, a correction is added due to the Gilbert damping that is proportional to the dynamic parameters ω_{rot} and

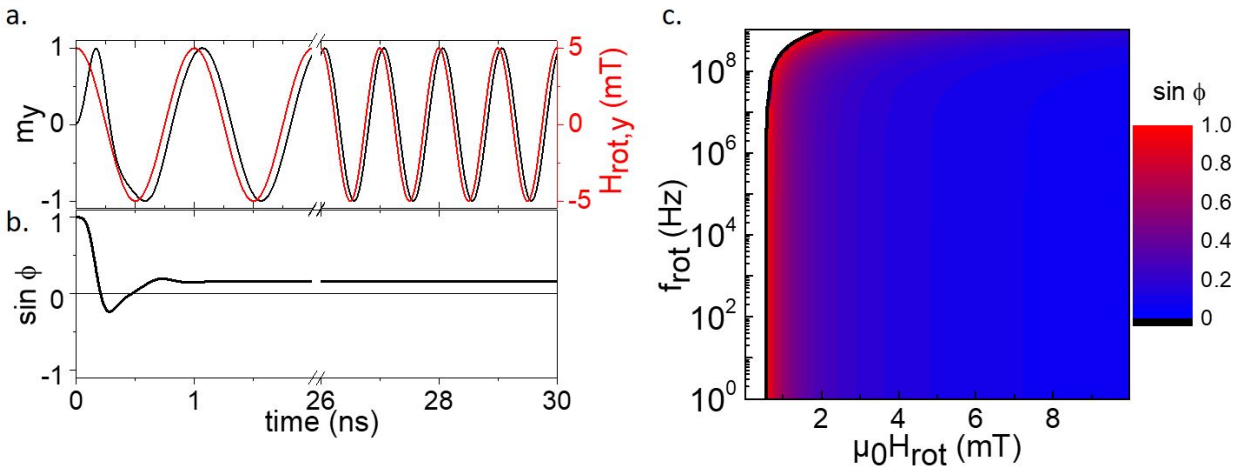

Fig. 3.2: Magnetization dynamics under in-plane rotating field | **a.** Time evolution of rotating field of 5 mT at 1 GHz and the response of an in-plane component of the magnetization for $\beta = 10^8 rad/s$. **b.** Time evolution of the drag angle between field and magnetization. **c.** Field amplitude-field frequency mapping of the stationary angle between field and magnetization. The black line is the analytical expression of the threshold field.

α_G. The two cases treated above (static and rotating field) clearly show how the dry friction term in the LLG equation affects both the static and dynamic behaviors of the magnetization. In the next paragraph, we show that such a dry friction can be brought out in ferromagneticy-antiferromagnetic-ferromagnetic sandwiches and analyze their dynamic magnetic behavior in light of the model presented above.

3.2.3 Spin transfer torque

As a further step towards the realization of a memristor based on the angular variation of the tunnel magnetoresistance of MTJs, the influence of the STT due to an additional perpendicular polarizer (P) on such an isotropically coercive in-plane magnetized free layer was investigated by simulation. This perpendicular configuration has been widely studied for spin torque nano oscillators and for fast switching precessional MRAM [136] [151] [152] [153] [154] [155] (Fig 3.3a). As described by Ebels et al. [136], under dc current, the influence of the STT from the perpendicular polarizer on the in-plane free layer is to slightly pull the magnetization of the free layer out of plane, which then starts precessing around its demagnetizing field. In the steady state regime, the out-of-plane angle as well as the precession frequency linearly increase with the applied dc current up to a point where the magnetization gets saturated out of plane and stops precessing. Now, if instead of dc voltage, successive voltage pulses are applied to the device, one can expect small in-plane step-by-step angular jumps of magnetization (depending on the amplitude and duration of the pulse), thus enabling the stabilization of intermediate levels of resistance between R_{min} and R_{max} depending on the sequence of voltage pulses. This is what we show below by numerical simulations.

3.2.3.1 Perpendicular polarizer STT-driven dynamics under dc current

From modeling point of view, Eq. 3.3 is modified by including the torque $T_{perp} = \gamma a_{||perp} V \vec{m} \times (\vec{m} \times \vec{p})$ where $p = [0 \quad 0 \quad 1]$ is the spin-polarization unitary vector, $a_{||perp}$ is the coefficient in the Slonczewski term [73] given by $a_{||perp} = \hbar/(2e)[\eta_{perp}/(lM_S R \times A)]$ where η_{perp} is the spin polarization, l is the layer thickness, V is the voltage across the tunnel barrier separating the perpendicular polarizer and the free layer, and $R \times A$ is the resistance-area product. The value used in this work is $a_{||perp} = 6mT/V$, corresponding to $\eta_{perp} = 0.3$, $R \times A = 5\Omega\mu m^2$, and $l = 4nm$. When the dry friction is considered, two regimes can occur that are separated by a threshold current density (Fig. 3.3b).

$$J_{perp} = V_{th}/(R \times A) = \frac{\beta 2 e l M_S}{\gamma \hbar \eta_{perp}} \tag{3.9}$$

For voltages lower than this threshold, the friction is stronger than the STT leading to an in-plane stable state of the magnetization. In contrast, above the threshold, the free layer magnetization is slightly pulled out of plane and the precession starts, initially with a relatively low frequency, then increasing linearly with the current density. In this last case, in the steady precession state, the precession frequency is given by

$$\omega_M = -\frac{\gamma a_{||perp} V}{\alpha_G} - \frac{\beta}{\alpha_G sin(\theta_M)} \frac{\omega_M}{|\omega_M|} \tag{3.10}$$

and the out-of-plane normalized component is

$$cos(\theta_M) = \frac{a_{||perp} V}{\alpha_G M_S} + \frac{\beta}{\alpha_G \gamma sin(\theta_M)} \frac{\omega_M}{|\omega_M|} \tag{3.11}$$

where $\frac{\omega_M}{|\omega_M|}$ indicates that the precession occurs in opposite directions (clockwise versus anti-clockwise) and the out-of-plane component of magnetization changes sign or opposite polarities of the voltage in Eqs. 3.10 and 3.11.

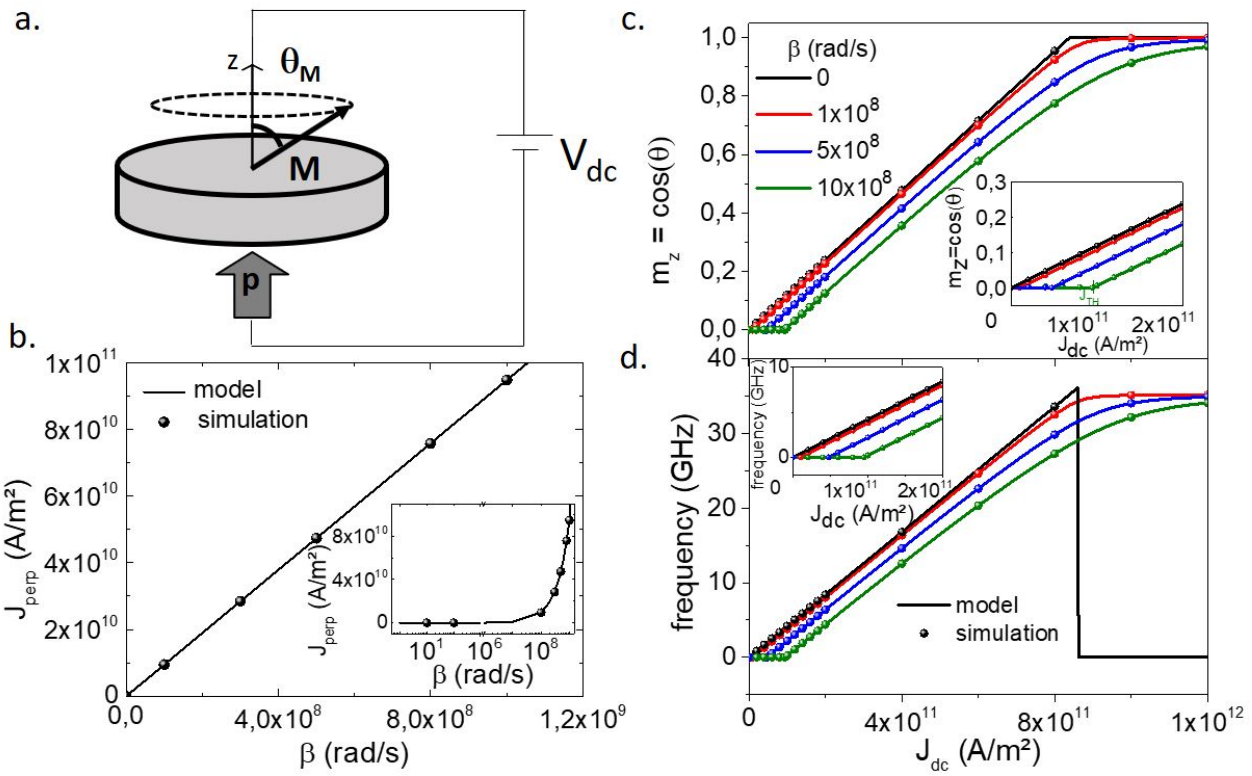

Fig. 3.3: Perpendicular polarizer STT-driven dynamics under dc current | **a.** Schematic of the STT effect on a sample with a free layer of magnetization $\vec{M}$ with dry friction and a perpendicular polarizer $\vec{p}$. **b.** Linear behavior of the threshold current density with β (in the inset the log scale). **c.** and **d.** Free layer out-of plane component and precession frequency versus dry friction amplitude. Insets: enlargements around the thresholds. The analytical model and the macrospin simulations are shown, respectively, in lines and dots for different values of β.

As indicated by Eqs. 3.10 and 3.11, the effect of dry friction shows up as a shift in both the frequency and out-of-plane component as shown in Figs. 3.3c and d. The macrospin simulations confirm that for low values of the friction parameter, the well-known linear behavior reported in Ref. [136] is recovered (black lines in Figs. 3.3c and 3.3d). Note that different from the case when

$\beta = 0$, the maximum value (corresponding to the case in which the magnetization is stable along the z axis and no more dynamics occur) is only reached asymptotically at infinite voltage.

3.2.3.2 In-plane field-dc current diagram with perpendicular polarizer

As explained in the general introduction, a transverse field can be used to limit the maximum excursion angle of the free layer magnetization in order to keep a fundamental property of a memristor: for the memristor resistance to be used as a synaptic weight, its resistance must vary monotonously for each current pulse polarity, that is, increase for one pulse polarity and decrease for the opposite pulse polarity [13] [14]. In the following, we show that this can be achieved by applying a static transverse field of appropriate amplitude on the free layer. To start with, the combined effect of the STT due to an applied dc current density and an in-plane static field is first considered by introducing both terms in H_{eff} and solving Eq. 3.3. In the case where the field H_{app} is applied along the y axis, the resulting effective field can be written as

$$H_{eff} = [Cm_y \qquad -Cm_x + H_{app} \qquad -M_S m_z] \tag{3.12}$$

where $C = (a_{||}/\mu_0)V$. In the numerical results shown in Fig. 3.4a, we can distinguish four regions (as in the previous paragraphs, the angle $\phi = \varphi_H - \varphi_M$): when the sum of the torques is lower than the dry friction (region 1), when one of the two is dominant (regions 2 and 3), and when the two are competing (region 4). In region 1, when the sum of the two torques is lower than the dry friction, magnetization motion cannot occur. The evident asymmetry in this region is due to the constructive or destructive competition of the two torques. In region 2, the torque due to STT is prevailing leading to out-of-plane steady state precession of the magnetization. The effect of the increasing field is to tilt the plane containing the precessing magnetization trajectory. In regions 3 and 4, the effect of STT acts as an in-plane discrete rotation of the magnetization that remains stable for all the pulse duration [136]. The static nature of the two torques can be analyzed as in the previous sections. In this case, looking for static ($\partial\vec{m}/\partial t = 0$) and in-plane solutions($\theta_M = \pi/2$), it can be found that the equilibrium condition becomes

$$|\gamma(H_{app} m_x) - C| < \beta \tag{3.13}$$

where, in this particular case, $m_x = sin(\phi_H - \phi_M)$. The final result is

$$-\frac{\beta}{\gamma\mu_0 H_{app}} + \frac{a_{||perp}}{\mu_0 H_{app}} V < sin(\varphi_H - \varphi_M) < \frac{\beta}{\gamma\mu_0 H_{app}} + \frac{a_{||perp}}{\mu_0 H_{app}} V \tag{3.14}$$

The creation of a stability sector around the effective field, as in Fig. 3.1, is modified by the STT linearly proportional to the applied voltage. It is interesting to note that an asymmetry with respect to the direction of the applied field is induced by the voltage term as shown in Fig.3.4b.

In fact, depending on the polarity of the applied voltage, the scalar product of the two components of the torque (field and STT) is positive or negative. Thus, the amplitude of the cone becomes only dependent on the field amplitude and the effect of the applied voltage is explicit in the angular shift. While in region 3 the effect of the field is dominant, leading to a small sector of stability more or less centered along the field direction (small angular shift), in region 4, the angular shift becomes significant, forcing the magnetization to point towards the positive or negative x axis direction depending on the polarity of the voltage. Moreover, the in-plane stable states created in this way can be destabilized for a threshold value of the current density J_{th} for which out-of-plane precession begins to occur (limit of the regions 1–2 and 2–4). This threshold value is given by

$$J_{th} = V_{th}/(R \times A) = \frac{\mu_0 H_{app} 2elM_S}{\hbar\eta_{perp}} - \frac{\beta 2elM_S}{\hbar\eta_{perp}\gamma} \tag{3.15}$$

As shown in Fig. 3.4a, the analytical white lines fit well with the oscillations limits obtained through macrospin simulations. It is important to note that the results in Fig. 3.4a are obtained by first applying the field at t=0 and then the voltage with a certain time delay (experimentally, the

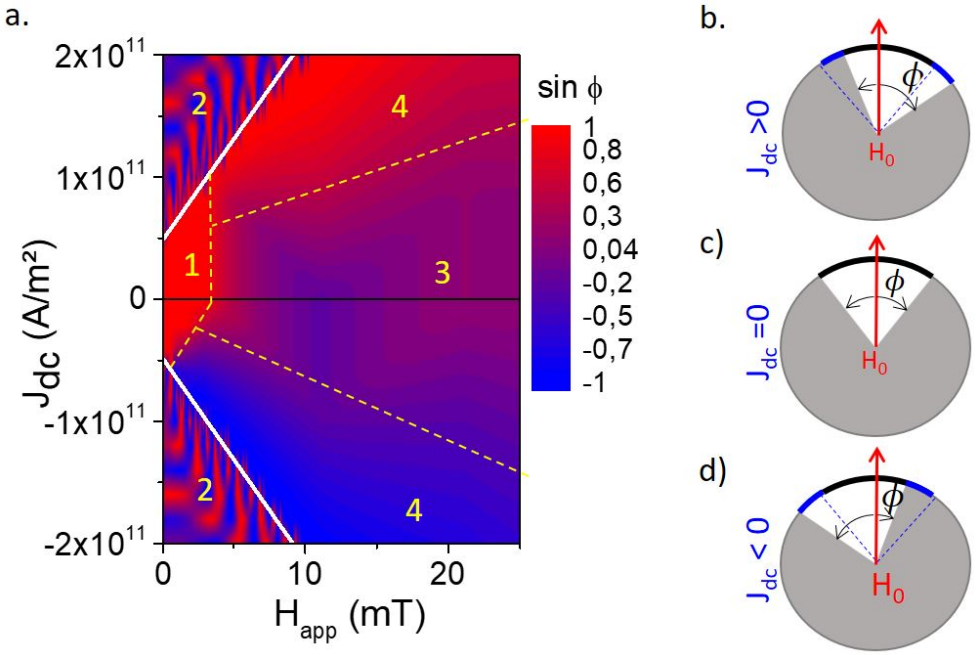

Fig. 3.4: In-plane field-dc current diagram with perpendicular polarizer | a. Current density-field diagram for $\beta = 5\times10^8 rad/s$. The white lines are the analytical limits of the oscillating region. **b.** - **d.** Schematics of the combined effect of field and current density on the system, respectively, for positive, zero, and negative polarity.

field is supposed to be applied all the time). In this case, a first relaxation of the magnetization can occur towards the cone and only after the effect of the angular shift on the final magnetization state is considered. Finally, it is important to underline that the dependence of the in-plane stable states (regions 3 and 4) on voltage cannot be exploited for the memristive characteristics. In fact, despite the linear behavior shown in Eq. 3.14, the monotonicity of the rotation with respect to the duration of the pulse is not respected (there is not any time dependence in the equation). Moreover, the application of two consecutive identical pulses will not have any effect because the magnetization will rotate forth and back by exactly the same angle when the pulse is applied and when it is switched off. For these reasons, the only way to obtain the wanted memristive characteristics is by exploiting the out-of-plane oscillating regime of region 2, achieving small angle rotations through the use of pulses.

3.2.3.3 STT from an in-plane analyzer

The full device with an out-of-plane polarizer (P), an in-plane free layer with dry friction (FL), and an inplane analyzer (A) is described in the macrospin code to simulate the complete memristor characteristics. Two STT terms must then be considered originating on the one hand from the bottom perpendicular olarizer, as already discussed, and on the other hand from the top in-plane pinned analyzer. Firstly, the effect of the STT term due to the analyzer is studied and compared to that of the polarizer. Similarly to the calculation done for the polarizer, the contribution of the torque coming from the in-plane analyzer is $T_{an} = \gamma a_{||an} V \vec{m} \times (\vec{m} \times \vec{l})$ where $\vec{l} = [1 \quad 0 \quad 0]$ is the spin-polarization unitary vector and $a_{||an} = \hbar/(2e)[\eta_{an}/(lM_S R \times A)]$ where η_{an} is the spin polarization. Looking for in-plane ($m_z = 0$) stationary solutions ($\partial\vec{m}/\partial t = 0$), we find that the threshold current density can be expressed as

$$J_{an} = \frac{\beta M_S l 2e}{\gamma \hbar \eta_{an}}. \tag{3.16}$$

Below this value of the current density, the magnetization is stable independently on its in-plane direction. By increasing the current density above this threshold, the magnetization starts to be

unstable or to move towards other in-plane stable states. Despite this, we find that the value of the current density needed to completely reverse the magnetization is very high (non physical) around $10^{13}A/m^2$. To futher investigate this aspect, we have simulated in-plane field - dc current density diagram in order to find the magnetization reversal region and the out-of-plane oscillating region at different conditions: for each of the two STT contributions (separately), the in-plane field is applied parallel and perpendicular to the analyzer magnetization direction, for $\beta = 0rad/s$ and for $\beta = 5 \times 10^8 rad/s$. The two junctions are supposed to be identical with a spin polarization of 0.3. The results are shown in Fig. 3.5.

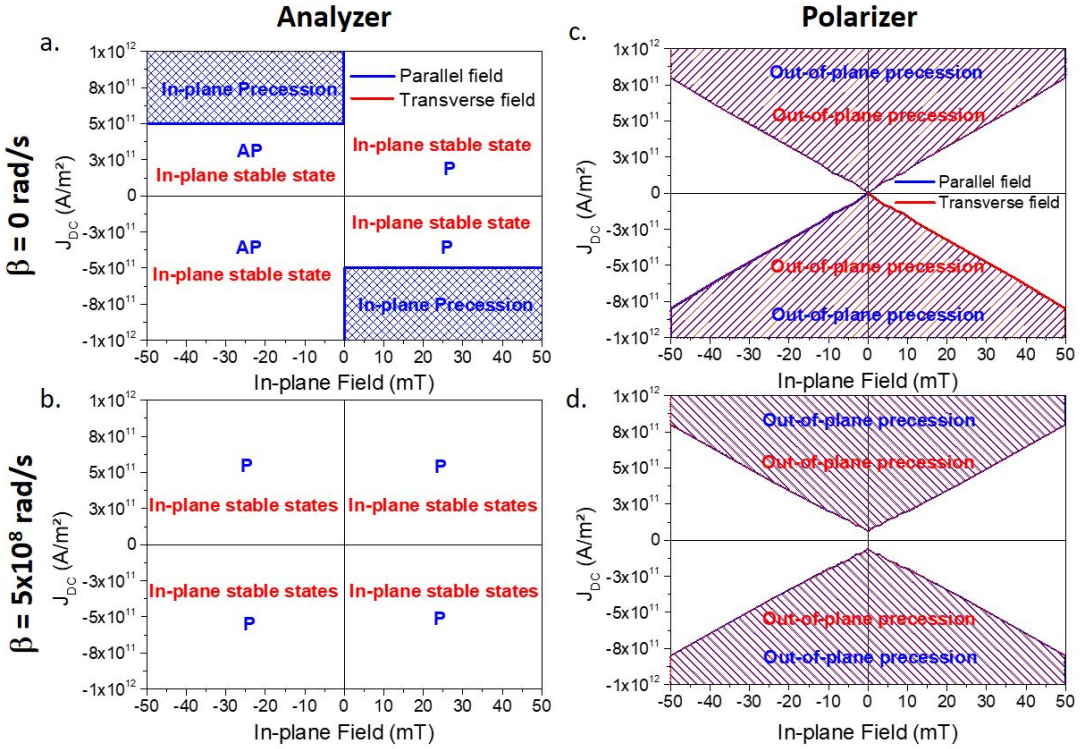

Fig. 3.5: In-plane field - dc current density diagrams for the two STT contributions | **a.** Dynamic phase diagram for only STT from analyzer with $\beta = 0rad/s$ for in-plane field applied parallel (blue) and perpendicular (red) to the analyzer magnetization direction. **b.** Same diagram as in a. with $\beta = 5 \times 10^8 rad/s$. **c.** Dynamic phase diagram for only STT from the perpendicular polarizer with $\beta = 0rad/s$ for in-plane field applied parallel (blue) and perpendicular (red) to the analyzer magnetization direction. **d.** Same diagram as in c. with $\beta = 5 \times 10^8 rad/s$.

Starting from the analyzer STT contribution, it is clear that for $\beta = 0rad/s$ (Fig. 3.5a), the effect of the transverse field (red phase diagram) is to shift the threshold of oscillations towards a higher values (higher than the simulated one) with respect to the case with the field parallel to the magnetization (blue phase diagram). The same effect is obtained by adding the dry friction term to the system with the field parallel (Fig. 3.5b in blue) where, in the voltage range simulated, it is not even possible to switch to the antiparallel configuration. We can conclude that the sum of both effects (dry friction and transverse field, as in the previous section and in red in Fig. 3.5b) is resulting in a relevant shift of the threshold. A similar effect occurs when the polarizer STT contribution is considered. In this case, the direction of the field does not affect the limits of the oscillating region because of an evident symmetry (Fig. 3.5c blue and red). Moreover, the effect of the dry friction, evident in a shift of the threshold, is much smaller than the one observed for only the analyzer. This can be explained by considering that the initial velocities associated with the two effects are very different. In fact, the slow beginning of the precessing motion in the case of the in-plane analyzer is easily stopped by the presence of the dry friction term, while in the case of polarizer contribution, the beginning of the precession is much faster.

3.2.4 Full stack and working regions

Finally we take into account the action of the STT terms from both polarizer and analyzer at the same time. The LLG equation is completed with a total torque given by $T_{tot} = T_{an} + T_{perp} = \gamma a_{||an} V \vec{m} \times (\vec{m} \times \vec{l}) + \gamma a_{||perp} V \vec{m} \times (\vec{m} \times \vec{p})$. As in the previous case, for in-plane ($m_z = 0$) stationary solutions ($\partial \vec{m}/\partial t = 0$), the resulting threshold is

$$J_{double} = \frac{\beta M_S l 2e}{\gamma \hbar} \frac{1}{\sqrt{\eta_{an}^2 + \eta_{perp}^2}}. \tag{3.17}$$

In this equation it is obvious how the ratio between spin-polarization factors plays a fundamental role in the magnetization dynamics of the device. To have a better overview of the working regions of the device, in Fig. 3.6a, the three critical lines of Eq. 3.9, Eq. 3.16 and Eq. 3.17 are plotted together with respect to the spin-polarization of the perpendicular polarizer η_{perp} for a fixed value of $\eta_{an} = 0.3$ (generic value for a tunnel junction). Considering a generic initial configuration of the magnetization of the free layer, the dotted line J_{an} represents the limit of stability of such state. Below this threshold there is the stability region where whatever in-plane magnetization direction is in equilibrium, while, above it, the magnetization is unstable. The dashed line J_{perp} is the critical line for the excitation of OPP. Above this line only OPP can occur (as in Fig. 3.6b). The green dashed dotted line J_{double} represents the correction to the stability line J_{an} due to the other STT contribution coming from the polarizer. In the unstable region, where the two STT contributions are competing, it is not possible to exactly define analytically the magnetization dynamics.

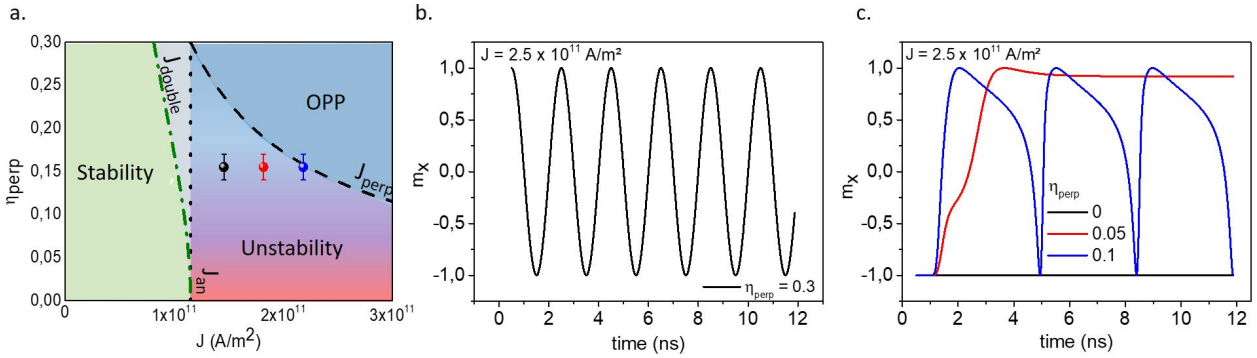

Fig. 3.6: STT dependent working regions | **a.** Analytical diagram of the working regions for a device with $\eta_{an} = 0.3$. The black, red and blue points are experimental values described later in this chapter. **b.** Magnetization dynamics under STT in the OPP region for $\eta_{perp} = 0.3$ and for current density $J = 2.5 \times 10^{11} A/m^2$. **c.** Magnetization dynamics under STT in the unstability region for different values of η_{perp} and for current density $J = 2.5 \times 10^{11} A/m^2$.

Generally, for values of η_{perp} close to zero, the torque from the analyzer is dominating, leading to a binary switching of the free layer. In this case, the addition of the dry friction term blocks all the stochastic behavior at the beginning of the switching mechanism, making the magnetization reversal almost impossible to occur at low current densities exactly as observed in the previous section (black line in Fig. 3.6c). By increasing the torque coming from the polarizer, the sum of the two contributions leads always to a binary switching but in a time significantly shorter than in the previous case. This is due to the reduced stochasticity introduced by the STT induced by the perpendicular polarizer. In this region, the binary nature of the torque T_{an} favors a switching between the parallel and the antiparallel configuration through a rotating trajectory dictated by the precession around the demagnetizing field because of the effect of T_{perp} as in the red line of Fig. 3.6c. For higher values of η_{perp}, the magnetization starts to precess because of the dominant effect of the perpendicular STT with a trajectory distorted by the other STT term (blue line in Fig. 3.6c).

For the final purpose of a memristive behavior, the two regions of OPP and unstability could be exploited. The two cases are described below.

3.2.4.1 Memristive behavior in the OPP region

The dynamic phase diagram of the full device under dc current and trains of current pulses, considering the sum of the two STT contributions coming from the two junctions, is shown in Fig. 3.7. The diagram under dc current (Fig. 3.7a) is actually similar to the one in Fig. 3.5d in which only the influence of the STT from the perpendicular polarizer is considered. Indeed, the effect of the STT from the in-plane analyzer in this field-voltage range is only to tilt the plane of the trajectory of the precessing magnetization, but it does not change the boundaries of the diagram. This is consistent with the results obtained in Ref. [156], where the effect of the analyzer is not to affect the out-of-plane precession region, but only to add another region of in-plane oscillations. The static field is applied in the perpendicular in-plane direction with respect to the top analyzer magnetization direction. It corresponds to the transverse field discussed in the previous section. Thus, if the magnetization goes from one edge to the other of the created sector of stability, the resistance will increase or decrease depending on the voltage pulse polarity (one of these edges is close to the parallel configuration of the top junction while the other is close to the antiparallel one). Note that the bottom junction is not giving any variation in terms of TMR since it remains in an invariant 90° configuration. Figures 3.7c and 3.7d show the free layer magnetization response to a series of positive and negative pulses as in Fig. 3.5d, respectively, without and with a transverse in-plane field of 3.5 mT (just above the threshold). This field allows the formation of a sector of stability (in white in Fig. 3.7d) that, as in Sec. 3.2.1, is narrower than 180°. After a fast relaxation of the magnetization inside the sector of stability, a series of identical positive pulses of 100 ps at $2.5 \times 10^{11} A/m^2$ is applied.

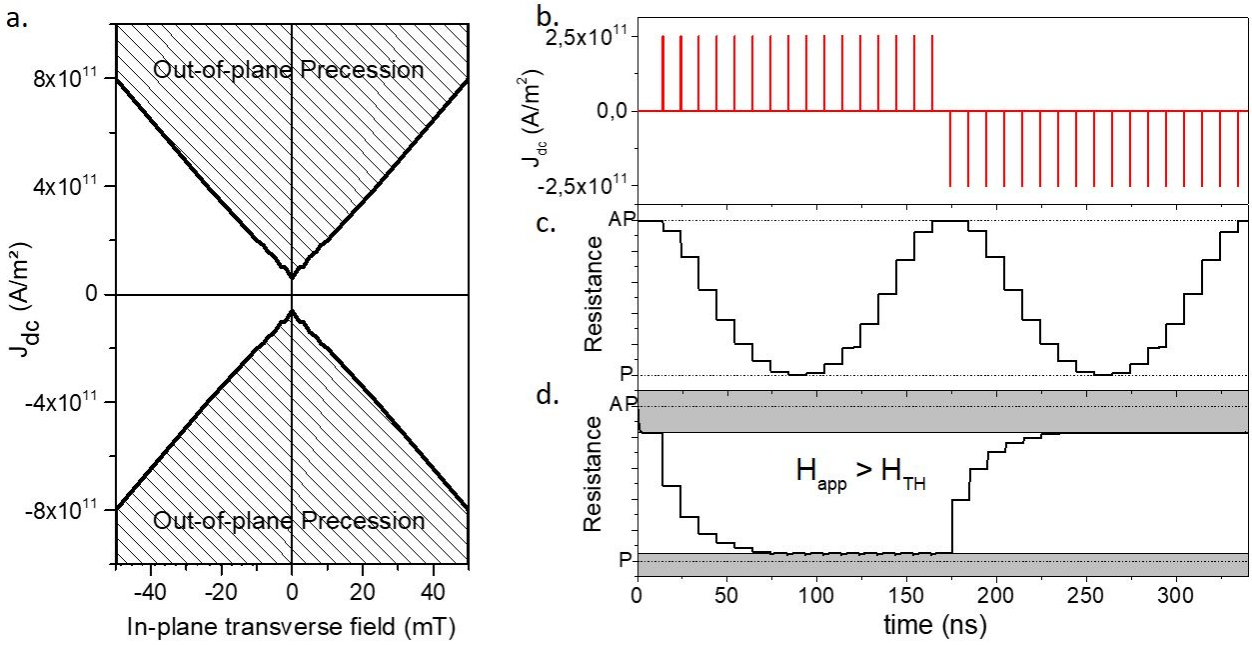

Fig. 3.7: Memristive operations using the OPP region a. Field-dc current density diagram of the device for $\beta = 5 \times 10^8 rad/s$. **b.** Train of pulses of 100 ps and $2.5 \times 10^{11} A/m^2$. Raise time of 50 ps. **c.** Numerical simulation of the time evolution of the resistance under a train of pulses as in b. for $\beta = 5 \times 10^8 rad/s$. **d.**Numerical simulation of the time evolution of the resistance under a train of pulses as in b. for $\beta = 5 \times 10^8 rad/s$ and $H = 3.5mT$.

The pulse duration is adjusted to be a fraction of the half period of the oscillations, which itself depends on the voltage as given by Eq. 3.10. As a result, several intermediate values of resistance can be reached. When the magnetization gets close to the limit of the sector of stability (after 70 ns in the plot of Fig. 3.7c), the voltage pulse pulls the magnetization out of it (in the gray region), but as soon as the voltage pulse ends, the magnetization relaxes back to within the sector of stability due to the torque from the transverse field (exactly as explained in Figs. 3.1c and 3.1d). This

effect can be used to definitely limit the maximum magnetization excursion angle to a region in which the resistance variation is monotonous as required for a memristor [13] [14]. The nonuniform rotation of the magnetization with identical pulses in Fig. 3.7d is due to the fact that while the spin transfer torque from the perpendicular polarizer is isotropic as is the dry friction torque, the torque due to the transverse field tends to attract the magnetization towards its direction with an amplitude proportional to the sine of the angle between the magnetization and field. As a result, for each polarity of the voltage, there is a region in which the rotation angle is larger because the two torques (from STT and from the field) favor the same direction of motion while in the other they oppose each other. Finally, the monotonicity of the resistance variation with the polarity of the voltage is only possible through the application of an in-plane field that would limit the motion of the magnetization only in half plane. Moreover, because of the very short pulse width, due to the relatively high frequency of oscillation (few GHz range), the error range for the application of pulses is very small (as for the precessional switching case). Those disadvantages make this region experimentally hardly exploitable for the final memristive behavior.

3.2.4.2 Memristive behavior in the unstable region

For these reasons, the unstability region seems to be better for this application. In particular, the fast binary switching, as the red line in Fig. 3.6c, would represent an ideal switching mechanism for our case. In fact, in this case, it would be possible to gradually rotate the magnetization thanks to the rotating trajectory and, at the same time, limit the magnetization excursion between the P and AP state. This would ensure the monotonicity of the resistance variation with the polarity of the voltage even without the application of an in-plane field (as for the OPP region). This is confirmed by the macrospin simulation in Fig. 3.8, where a train of positive and negative pulses ($2.5 \times 10^{11} A/m^2$, 1ns and 100ps of raising time) is able to discretely rotate the magnetization achieving the monotonicity of the resistance variation without the presence of any field (for $\eta_{perp} = 0.05$).

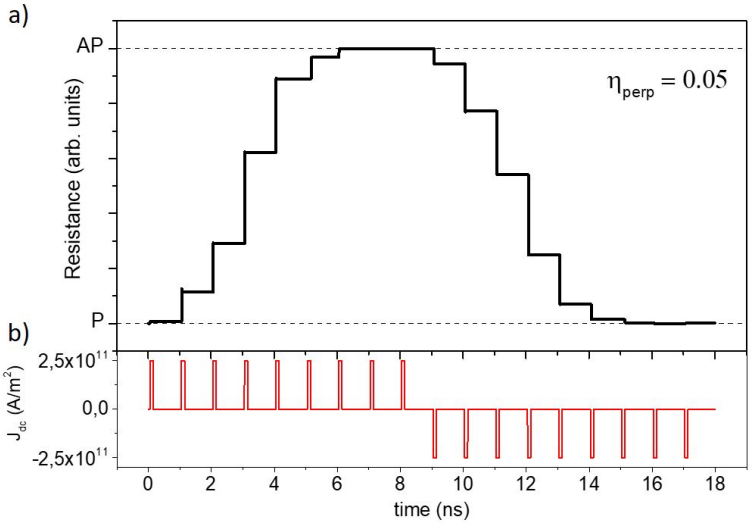

Fig. 3.8: Memristive operation using the unstability region | **a.** Resistance variation to a train of pulses as in **b.** for $\eta_{perp} = 0.05$ ($\beta = 5 \times 10^8 rad/s$).

Because of those advantages, we chose to develop a device within the unstability region of Fig. 3.6a. To do this, a short description of the material development follows in the next section before the final electrical characterization results.

3.3 Material development

The totality of measurements presented in this section was performed on full sheet samples in order to find the magnetic properties required in the final device.

3.3.1 Isotropically coercive free layer

Early studies in 1987 [157] and 1993 [158] reported the experimental and numerical observations of dry friction effects in ferromagnetic systems with distributed axes of anisotropy. In such systems (e.g., amorphous rare-earth/transition metal alloys [157]), the dry friction arises from coupled spins or grains that, having an isotropically distributed anisotropy direction, tend to fall into their potential minimum during a collective motion of the magnetization. The associated dissipation is enhanced for a proper ratio between the random anisotropy and the exchange energy. Here, we propose an alternative system with similar dry friction-like behavior, which can be integrated in MTJs. The idea is to exploit the frustration of exchange interactions, which exist at the interface between a F and an AF due to competing positive and negative exchange interactions, similar to an interfacial spin glass [159]. In the past, several publications have discussed the influence of the antiferromagnet thickness on the exchange bias and coercive field of such F-AF bilayers [160] [161]. After annealing under a magnetic field, an exchange bias appears above a certain thickness of the AF layer (typically above 2 nm for IrMn at room temperature (RT) [162]). This results from the fact that above this thickness, the anisotropy of the AF layer becomes sufficiently large for the AF spin lattice to resist the interfacial torque exerted by the F magnetization on the AF spin lattice upon field cycling. However, below this critical AF thickness, the AF spin lattice is fully dragged due to the torque caused by the F magnetization, yielding dissipation (coercivity) but no exchange bias. A maximum in coercivity is observed for an AF thickness corresponding to this critical thickness. For these low AF thicknesses, the interfacial frustration makes the AF spin lattice so disordered that it exhibits spin glasslike isotropic properties. Its dragging upon the motion of the F magnetization is expected to yield a dissipation equivalent to a dry friction, as in random anisotropy systems [157]. We perform an experimental study to investigate the AF thickness dependence of coercivity and exchange bias field in unpatterned Py(1 nm)/IrMn(l_{IrMn},)/Py(1 nm) trilayers, deposited by sputtering ($Py = Permalloy = Ni_{80}Fe_{20}$). These samples are annealed at 300 °C for 1 h and 30 min under an in-plane field of 0.23 T. Fig. 3.9a shows the influence of the IrMn thickness (l_{IrMn}) on the exchange bias and coercive field in these trilayer systems. All experiments described here were performed at room temperature (a part for the temperature section). As expected, for a critical thickness of IrMn (2.1 nm here), an enhanced coercivity and a zero exchange bias are measured with a vibrating sample magnetometer technique (VSM). This critical thickness of IrMn is, therefore, selected in the subsequent experimental studies.

3.3.1.1 Rotational hysteresis

Hysteresis loop measurements were performed on the sample with the VSM technique 2.2.1. As shown in Fig. 3.9b, a first hysteresis loop was measured with the field applied parallel to the annealing field (corresponding to $\varphi_H = 0$). Then other measurements were performed with the field applied in different directions characterized by the in-plane angle φ_H. For each field direction, a single loop is observed indicating that the two ferromagnetic layers are strongly coupled through the thin AF layer. Moreover, the variations of the coercive field between loops at different in-plane angles are below 5% (Fig. 3.9c). Therefore, as expected, such a F-AF-F sandwich can be considered as exhibiting an isotropic coercivity (similar to the model described in the previous section). Because the AF spin lattice is fully dragged upon field cycling, the AF layer exerts a dry friction on the F magnetization independent of the direction of application of the field. Note that this effect is visible in the rounded shape of the loop. The magnetization reversal is not occurring in a straight transition but an increasing field is gradually dragging it towards the opposite state. This is predicted from the model in Sec. 3.2.1, since, the magnetization tends to align with the field only for very high values of this last, when the sector of stability gradually reduces.

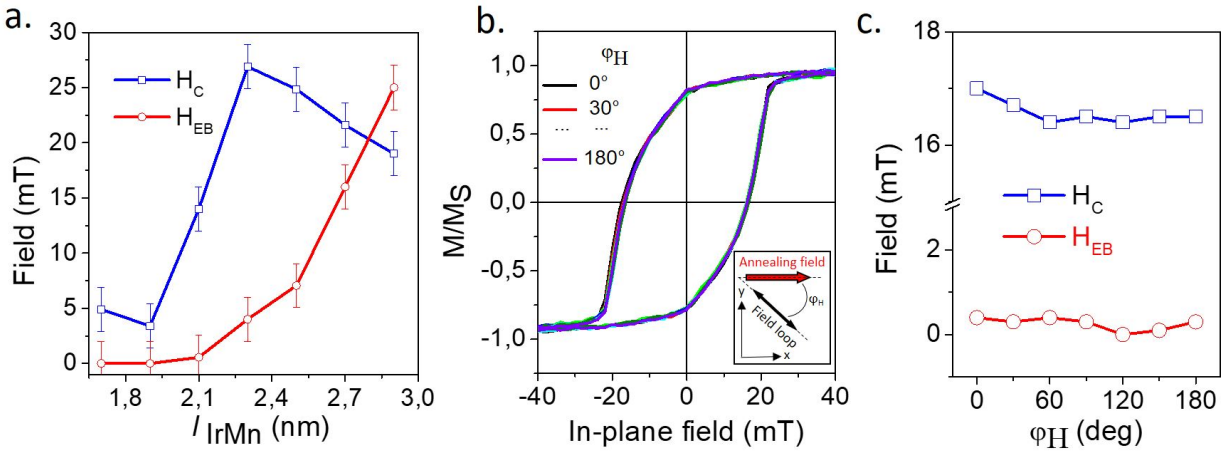

Fig. 3.9: Isotropically coercive layer | **a.** Coercive field H_C and exchange bias H_{EB} dependence on IrMn thickness. **b.** Hysteresis loops at different in-plane angles with respect to the annealing field direction (red arrow in the inset) for $l_{IrMn} = 2.1nm$. **c.** Coercive field H_C and exchange bias H_{EB} dependence on the in-plane angle φ_H for $l_{IrMn} = 2.1nm$. [10]

3.3.1.2 Planar Hall resistance measurement under rotating field

Planar Hall Effect (PHE) (Sec. 2.2.4) [46] measurements are performed on the Py/IrMn/Py trilayer under a rotating field, similar to the simulations described in the previous section related to the influence of a rotating field on the free layer magnetization dynamics in the presence of dry friction (measurement performed with the help of J. Nath and I.M. Miron). A rotating magnetic field of various amplitudes (0–34 mT) and varying frequencies up to 10 Hz is used. The sample is connected to the voltage and current terminals in a Hall geometry allowing to measure the planar Hall resistance (R_{PHE}). The angular dependence of this parameter is described as

$$R_{PHE} = \frac{V_H}{I} = \frac{\Delta R}{2} sin(2\varphi_M), \tag{3.18}$$

where V_H is the Hall voltage, ΔR is the PHE magnetoresistance, and φ_M is the in-plane angle of the magnetization with respect to the current direction [139]. When dry friction comes into play, if the rotating field amplitude is large enough, the magnetization is expected to follow the rotating field with a certain drag angle $\phi = \varphi_H - \varphi_M$ given by Eq. 3.8 (where φ_H is the angle of the field with respect to the current direction). This should result in a PHE signal varying as $R_{PHE} = \frac{V_H}{I} = \frac{R}{2} sin(2\varphi_H - 2\phi)$. This formula can be applied for extracting the value of the drag angle ϕ for different values of the field amplitude, and thereby for deriving the β parameter from Eq. 3.8. The experimental results, shown in Fig. 3.10, are performed on the same sample of the previous paragraph ($l_{IrMn} = 2.1nm$) and obtained by first saturating the in-plane magnetization along the current direction and then applying the rotating field of the selected amplitude. As expected, for field amplitudes lower than the coercive field ($H_C \approx 15mT$) (black line in Fig. 3.10a), the magnetization is not able to follow the field. When the field becomes higher than the threshold value, following an initial transient regime, a $sin(2\varphi_H)$ dependence of the PHE signal is observed with a phase shift dependent on the field amplitude. This is consistent with the general picture that the magnetization is rotating with the field with a drag angle due to dry friction.

The fact that the amplitude of the PHE signal depends on the applied field amplitude means that the magnetization does not remain fully saturated during this rotation, but is probably distributed at the microscopic scale within an angular sector around the average drag angle. The higher the rotating field amplitude, the narrower this angular sector. In Fig. 3.10b, the angular dependence of the sine of the drag angle derived from the PHE phase shift is plotted versus field amplitude. The fit of this variation with Eq. 3.8 is quite good and yields $\beta = 1.67 \times 10^9 rad/s$. Moreover, the value of the coercive field of the sample (in the red dashed line in Fig. 3.10b) is found to be different from the threshold field predicted by the fitting curve. Again, a reduction in the total magnetization during

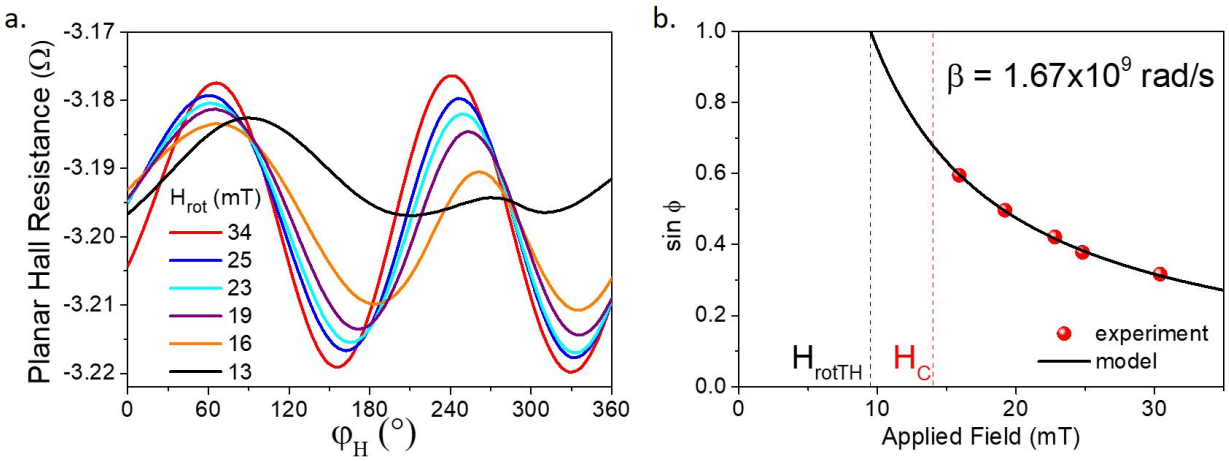

Fig. 3.10: Planar Hall resistance under in-plane rotating field | **a.** Planar Hall resistance under rotating field for different field amplitudes. **b.** Experimental angular shift (red points) fitted by Eq. 3.8 (black line).

the motion can explain the higher value of the coercive field found experimentally with respect to the one found by the model. In conclusion, in this section we show that an isotropically coercive layer can be realized using a ferromagnetic-antiferromagnetic-ferromagnetic trilayer in which the antiferromagnetic layer is adjusted just below the onset of the exchange bias. Interestingly, we found agreement with the model extracting a realistic value of the β parameter.

We acknowledge Jay Nath and I. Mihai Miron for the help with this measurement.

3.3.1.3 Temperature dependence

The presence of a thin IrMn layer in the system introduces some problems related to its temperature sesitivity. The first issue is related to the high temperature-induced diffusivity of the Mn ions during the annealing process.

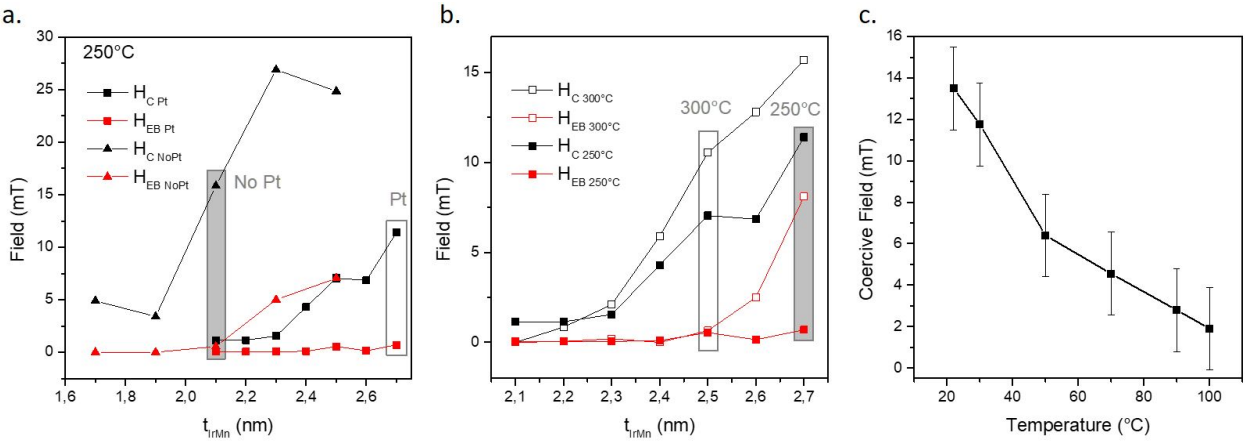

Fig. 3.11: Temperature dependences | **a.** Coercive field H_C and exchange bias H_{EB} dependence on IrMn thickness for 250°C annealing temperature for a sample with and without Pt insertions. **b.** Coercive field H_C and exchange bias H_{EB} dependence on IrMn thickness for a sample with Pt insertions at 250°C and 300°C annealing temperatures. **c.** Coercive field H_C dependence on temperature for a sample with Pt insertion and $l_{IrMn} = 2.5nm$.

This represents a significant problem because of the vicinity of the IrMn to the MgO barrier. In fact, the magnetic properties can be affected by the presence of Mn along the MgO/FeCoB interface. In this sense, a solution, already proposed in ref. [163], uses some Pt insertions close to the IrMn

layer as barriers against diffusion. Here the sample Py(1)/IrMn(l_{IrMn})/Py(1) is compared to a sample Py(1)/Pt(0.4)/IrMn(l_{IrMn})/Pt(0.4)/Py(1). This degrades the interfacial coupling between the IrMn and the Py layers as it is visible from the curves in Fig 3.11a. Despite this, the Pt insertions allow to increase the annealing temperature (Fig. 3.11b), bringing advantages in terms of TMR and STT because of a better MgO crystallization. Another issue due to such thin IrMn layer is linked to its relatively low blocking temperature. As shown in Fig. 3.11c, the IrMn strong temperature dependence is directly linked to the coercive field of the trilayer structure through the interfacial coupling. This phenomenon significantly affects the behavior of the device when the applied current pulses create an increase of the temperature due to Joule heating.

3.3.1.4 Magnetic configuration

In order to better understand the isotropic properties described above, we studied the magnetic configuration of the free layer through TEM Lorentz imaging (see Sec. 2.2.5).

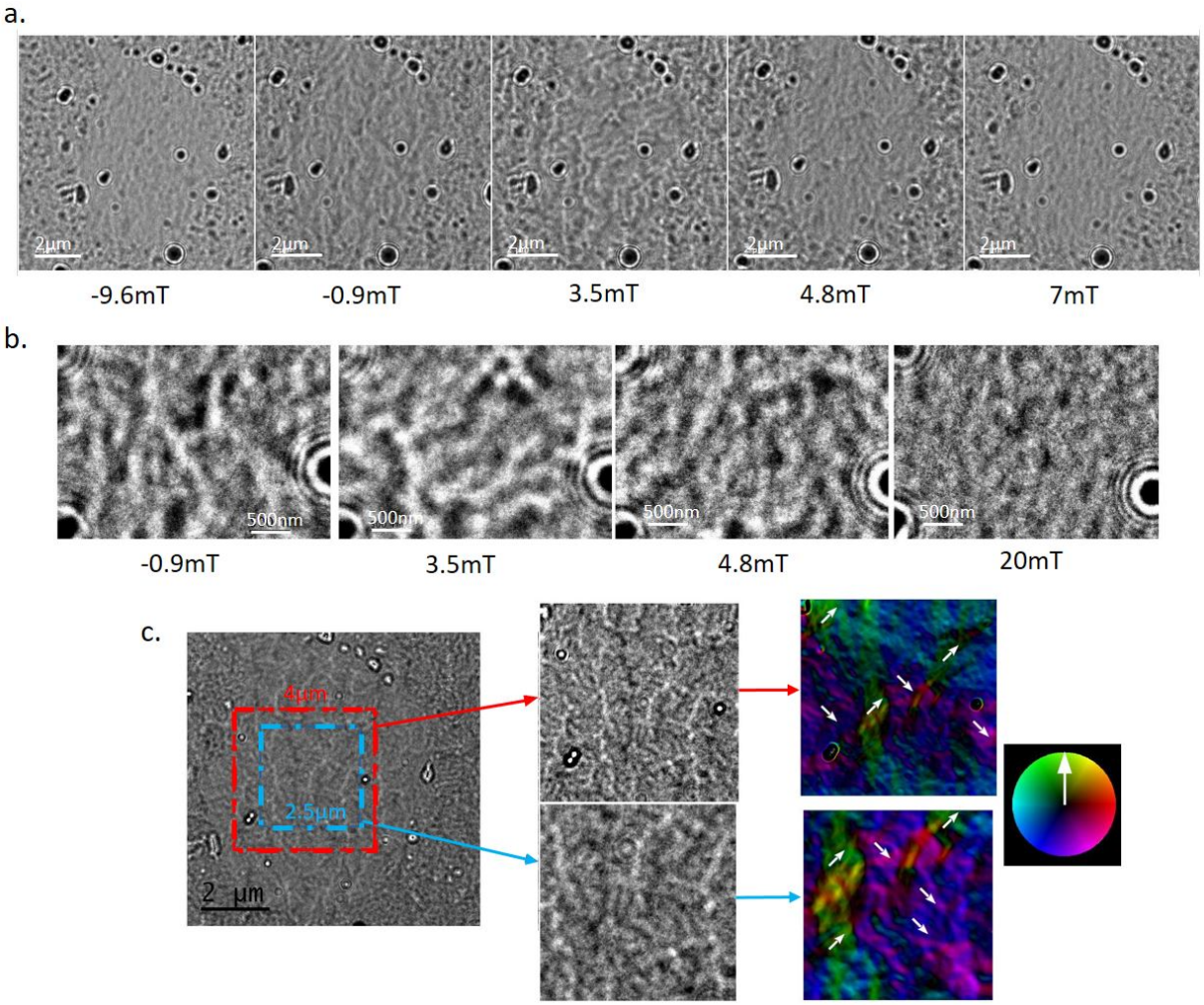

Fig. 3.12: TEM images of the free layer | **a.** Lorentz TEM images in Frenel mode of the free layer Co(0.6)/Py(1)/IrMn(2.1)/Py(1)/Co(0.6)/Ta(0.3)/FeCoB(1.6) for different in-plane field values (scale $2\mu m$) **b.** Lorentz TEM images in Frenel mode of the free layer for different in-plane field values (scale $500nm$) **c.** Lorentz TEM images in Frenel mode of the free layer and relative zoom as indicated by the dashed lines. The right panels are the relative magnetic induction cartography obtained through focal series reconstruction (through Transport of Intensity Equation [140]).

In Fig. 3.12a, a series of Lorentz TEM images in Fresnel configuration shows the domain wall complex structure created in such sample. In the following images, in Fig. 3.12b, it is clear that the actual size of the domains is very small (hundreds of nm) despite the resolution limit of such

technique. To further investigate the magnetic structure of the isotropic free layer, the magnetic induction cartography of a relatively small part of the sample shows that the in-plane component of the magnetization is spread over several directions (Fig. 3.12c). This and the very small size of the domains can be due to a distribution of the anisotropy direction in such layer that could be an effect of a uniform distribution of defects. A cause of this can be found in the granular nature of the IrMn layer. In fact, its relatively small thickness is not sufficient to set a unique Néel vector but it creates a spin glass-like structure. This structure then influences locally the ferromagnet magnetization orientation through the exchange interaction at the interface. In this way the ferromagnetic layer shows the complex magnetic structure as in Fig. 3.12c. We associate to this the isotropic properties described in this section. In fact, despite the evidence of a non-macrospin behavior, the dry-friction based model describes in a quite accurate way the results obtained experimentally. This proves the equivalence of this model with more complicated micromagnetic approachs as already stated in ref. [164].

We acknowledge Aurélien Masseboeuf for the images and the data treatment.

3.3.2 In-plane exchange-biased SAF

The in-plane magnetized synthetic antiferromagnet described in this paragraph is placed on top of the isotropically coercive layer so to provide the TMR used as reading mechanism. Here we develop a structure based on a layer pinned through exchange bias IrMn(7)/Py(1)/Co(3) and a reference layer Co(0.6)/Ta(0.3)/FeCoB(1.6) coupled with RKKY through a thin Ru(0.9nm) spacer. The capping layer has a Cu(3nm) layer in direct contact with the IrMn layer and a final Pt(3) layer. At the bottom part, the MgO is deposited as Mg(0.7), oxidized for 30 seconds at a pressure of $3 \times 10^{-3} mbar$ and covered with an additional Mg(0.5) layer. This gives a junction with an $R \times A$ around $7\Omega\mu m^2$. The stack is optimized for an annealing of 1h30 at 300°C. An in-plane field of 230mT is applied during the annealing in order to set the direction of the Néel vector in the IrMn. The resulting magnetization curve measured in the VSM is shown in Fig. 3.13a. As shown schematically by the black arrows, the SAF is stable in a range of $\pm 50mT$. For higher field amplitudes, the RKKY is not strong enough to keep the two magnetizations in an antiparallel configuration. The same structure is then deposited on top of the isotropically coercive free layer. As complement to the Py(1)/Pt(0.4)/IrMn(l_{IrMn})/Pt(0.4)/Py(1) structure, a part with Co(0.6)/Ta(0.3)/FeCoB(1.6) is added on the top part in order to optimize the transport properties across the MgO. The magnetization curve after annealing is shown in Fig. 3.13b. The free layer hysteresis loop turns out to be well centered in the stability range of the SAF. The isotropic properties of such structure have been checked in full sheet film.

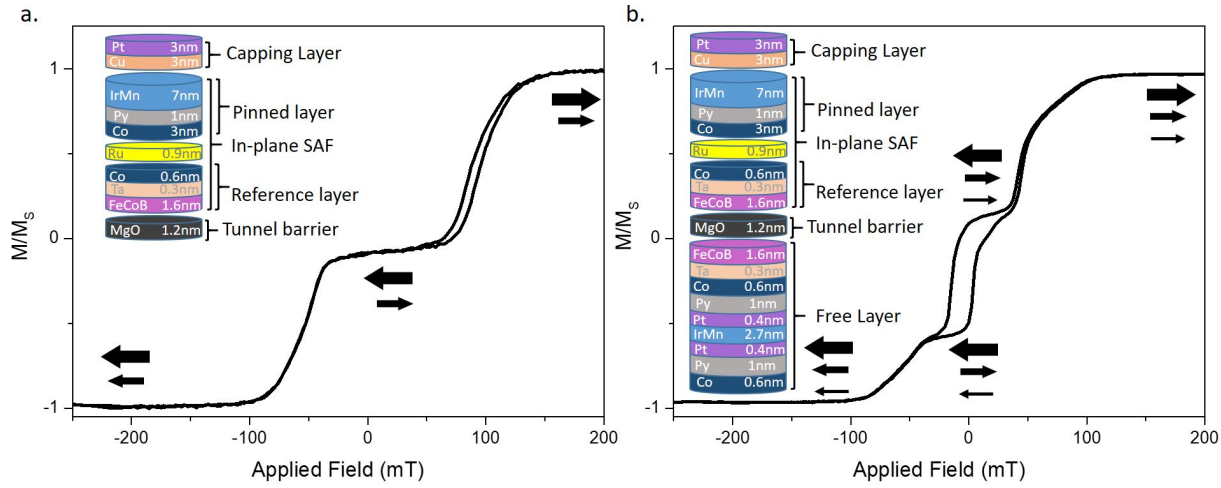

Fig. 3.13: In-plane SAF development | **a.** VSM curve of the magnetization for an in-plane SAF as in the inset. **b.** VSM curve of magnetization for an MTJ with an in-plane SAF and in-plane isotropic free layer as in the inset.

3.3.3 Perpendicular polarizer

The perpendicularly magnetized polarizer, placed at the bottom of the isotropic free layer, has the purpose of influencing the magnetization dynamics of the free layer through STT. The structure used in this work was developed and otpimized during the past years [165]. It is based on a Pt(5nm) seed layer on top of which an out-of-plane magnetized synthetic antiferromagnet is grown. This last is based on Co(0.5)/Pt(0.25) multilayers giving an interfacial perpendicular magnetic anisotropy. Here the reference layer has 6 repeats of Co(0.5)/Pt(0.25) and it is coupled to the 3 repeats constituting the reference through a Ru(0.9) spacer.

3.3.4 Full stack

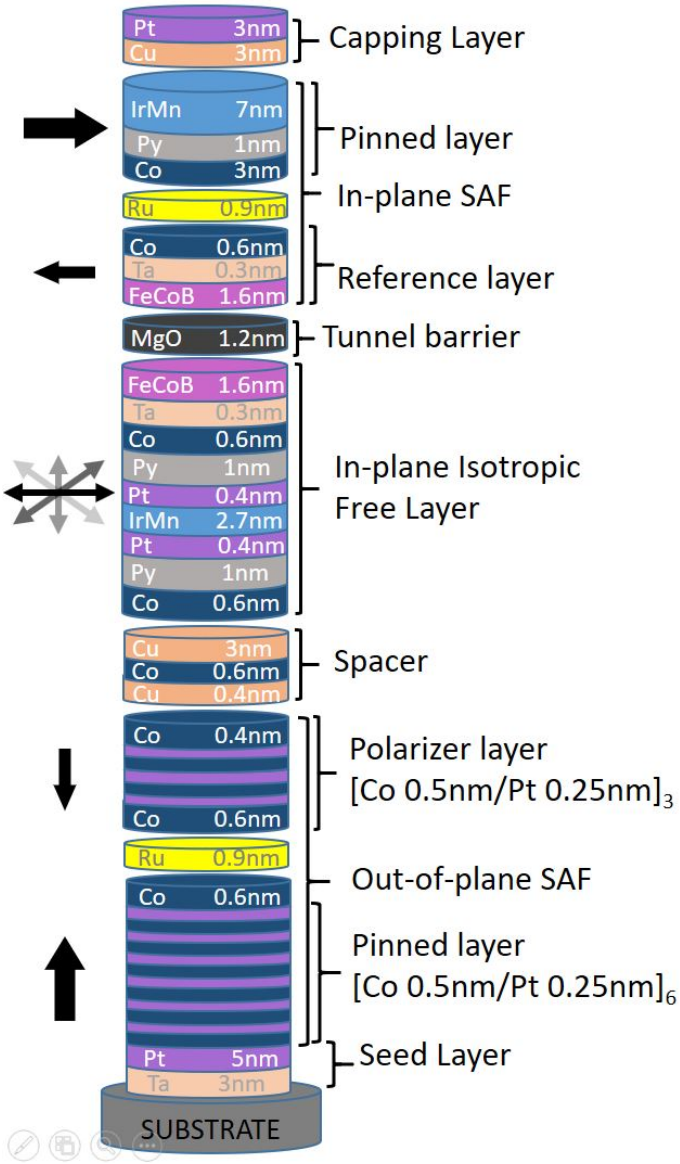

Fig. 3.14: Full stack | Schematic of the full stack and relative magnetization direction (black arrows).

Finally, the full material stack is shown in Fig. 3.14. The perpendicular polarizer is connected to the isotropic free layer through a Cu(3) spacer. This, accordingly to the simulation results presented in the previous section, lowers the spin polarization (called η_{perp} in the simulation part) so to achieve the memristive behavior as described in the unstability region. (The case of double MgO structure will be analyzed later in this chapter). A Cu(0.4) lamination is used to optimize the spin polarization of the current produced by the perpendicular polarizer [166] [167]. The structure is annealed at 300°C for 1h30 under an in-plane magnetic field of 230mT. As anticipated, the role of the annealing is fundamental for different reasons. As first effect, the use of an annealing temperature higher than the Néel temperature of the IrMn is used to set the Néel vector of such layer through the application if an in-plane field. The direction of the field set the magnetization direction of the in-plane SAF at the top of the structure. Another important effect of the annealing is the crystallization of the FeCoB(1.6)/MgO(1.2)/FeCoB(1.6) trilayer. This starts from the (100) texture of the MgO and propagates towards the amorphous FeCoB. In this way, while the B is absorbed by the nearest Ta layer, the remaining FeCo is perfectly crystallized with the same texture as the MgO. This good crystallographic matching between the barrier and the magnetic electrodes is mandatory to obtain good transport properties such as TMR and STT. Moreover, the presence ot the amorphous Ta insertions is used to break the texture since it is not favorable for the magnetic properties of the other layers (such as Co/Pt for example).

This stack is subsequently patterned in nano-sized pillars with the process described in the previous chapter.

3.4 Electrical results on patterned devices

All the results shown in this section come from measurements performed on patterned devices. The specific size and characteristics of the devices is detailed at each measurements.

3.4.1 Field-driven measurements

3.4.1.1 Angular dependence of TMR

A series of hysteresis loop measurements was performed at different in-plane angles with respect to the AL layer magnetization direction. First, note that the rounded shape of the resistance loop as in Fig. 3.15a corresponds to the full sheet film curve measured in the previous section and to the one expected from the model. A straight transition would indicate an immediate switch of the magnetization and, therefore, a non functional device. The experiment is realized with two couples of coils placed around the sample as in the setup described in the previous chapter. As shown in Fig. 3.15b, the coercive field of the different loops do not vary (with an error below 7%) while the high and low resistance states at zero field are gradually shifting towards the center. This demonstrates that the magnetic properties are again independent on the in-plane angle even at device level. The obtained variation of TMR was directly compared to the cosine variation expected in the ideal case in Fig. 3.15c showing good agreement.

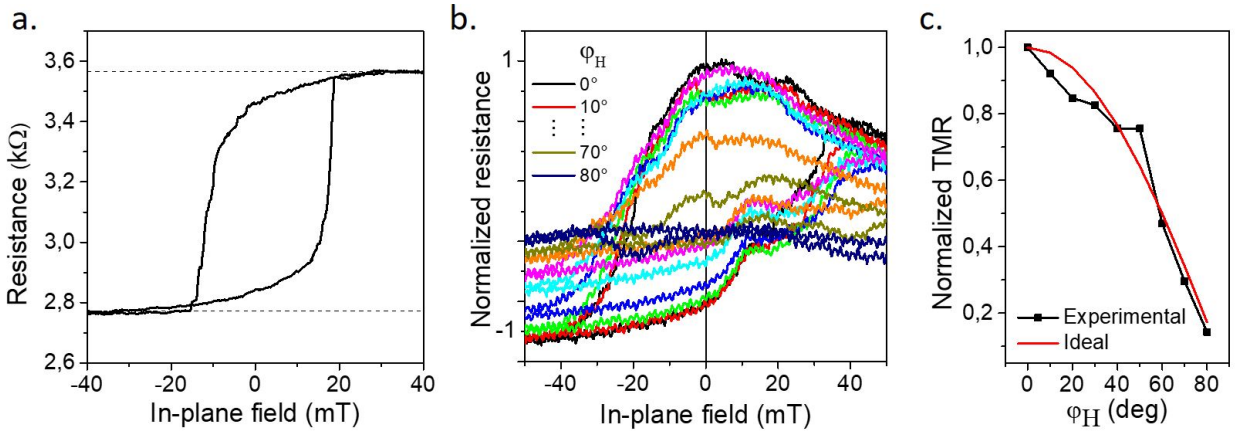

Fig. 3.15: Angular dependence of TMR | **a.** Example of resistance loop of a device with 80nm diameter, TMR≈ 32% and $R \times A \approx 15\Omega\mu m^2$. **b.** Example of evolution of resistance loops with the in-plane field angle. **c.**TMR variation with the in-plane angle in an ideal case (red line) and experimentally obtained.

3.4.1.2 Rotating field experiment

Rotating field experiments were performed on a similar setup as the previous one. The two couples of coils along x and y directions are supplied by 90° out-of-phase currents creating a rotating field on the device of constant amplitude. The rotating field frequency could be varied up to 5Hz. The results shown in Fig. 3.16a correspond to an applied field of 40mT and frequency of 2Hz. The resistance (Fig. 3.16b) is oscillating between its maximum and its minimum value with the same frequency as the rotating field one. Note that the resistance smoothly varies in quasi-sine form, passing through all the intermediate values. In contrast to this, if the same experiment is performed on a standard binary MTJ with similar characteristics, the result of Fig. 3.16c is observed. The resistance values are then distributed non uniformly with two main regions in the high resistance region and in the low resistance region. The magnetization does not follow smoothly the rotating field. Due to its uniaxial anisotropy, during its rotation, the FL magnetization undergoes irreversible jumps while it crosses its hard axis direction. Also in this case, the isotropic properties of the device can be confirmed.

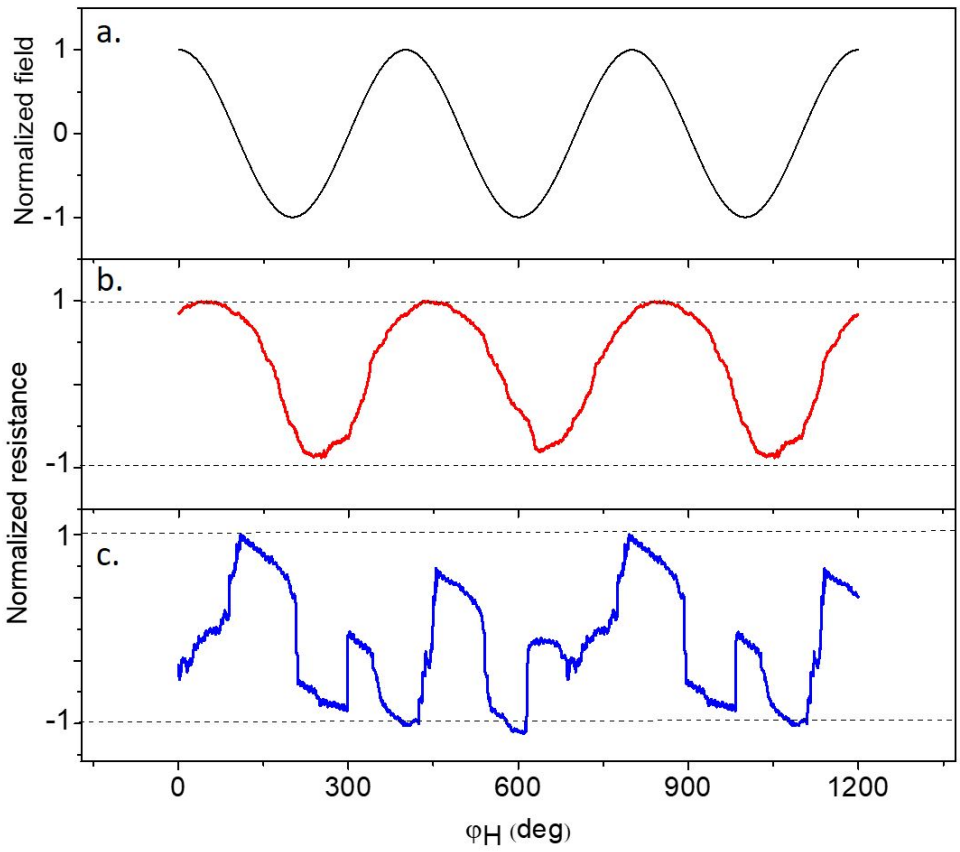

Fig. 3.16: Resistance evolution under in-plane rotating field | **a.** Rotating field applied to the experiment. **b.** Resistance variation of a device of 80nm of diameter, TMR≈ 32% and $R \times A \approx 15\Omega\mu m^2$ as in Fig. 3.14. **c.** Resistance variation of a standard binary MTJ of 80nm of diameter, TMR≈ 72% and $R \times A \approx 8\Omega\mu m^2$ with only two stable states.

3.4.2 STT-driven measurements

3.4.2.1 Single pulse

The first experiment aims to find the pulse characteristics (amplitude and duration) for which the STT makes the magnetization discretely rotate. To do this, the device is first set in the parallel state through the application of a strong in-plane field and, in a second moment, a single pulse is applied (at zero field) followed by the read out of the final resistance state. The device is reset in the P state before each pulse. This is repeated for different pulse amplitudes and durations similarly to a switching probability experiment on a binary device. In this case, instead of the switching probability, we expect to see the actual resistance variation dependence on the pulse parameters. The resulting experimental points (each averaged over 10 measurements) are shown in Fig. 3.17a (where $\Delta R = R_{afterpulse} - R_{beforepulse}$) for a junction with a nominal diameter around 100nm, TMR around 30% and $R \times A \approx 8\Omega\mu m^2$. The magnetization angle is directly extracted from the measurement through the cosine variation of the conductance [135] and shown in Fig. 3.17b. It is obvious that a monotonicity of the resistance variation is obtained with respect to both the pulse amplitude and duration. For each amplitude of the voltage, a threshold pulse length separates a region in which the magnetization is not moving from a region in which discrete rotations are measured. Those threshold values are decreasing with the increase of the voltage amplitude, as expected. The experimental points are fitted with a line that represents the ideal behavior in case of coherent precession of the magnetization (where the magnetization angle is linear with time). We note that the oscillation frequencies extracted turn out to be significantly lower than the GHz range. This is likely the result of the important increase of the Gilbert damping already observed in

trilayers of FM/AF/FM [168] [169] [170] and expected from the expression in Eq. 3.10. The linear behavior of this last equation with respect to the applied voltage can be used to fit the experimental points as in Fig. 3.17c. From this fit, the extracted threshold voltage for the triggering of the OPP is around 0.6V. From this value, that corresponds to the critical line J_{perp} in Eq. 3.9, one can estimate a value of $\eta_{perp} \approx 0.15 \pm 0.2$ that leads, through Eq. 3.10, to a value of $\alpha_G \approx 0.07 \pm 0.1$. The experimental points can be compared to the analytical diagram in Fig. 3.6a, finding that the experimental working region is actually not in the OPP region but in the unstable one. Despite the fact that the values of η_{perp} and α_G perfectly match the expectations, they can be affected by an error coming from the fact that the equations used to extract them are valid in the OPP region and in the long pulses approximation while the experimental points are taken in the unstability region where no analytical expressions can be computed. Also, the importance of the STT coming from the perpendicular polarizer is confirmed by the fact that, in devices as in Fig. 3.14 but without perpendicular SAF, no switching actually occurs for pulse parameters as in Fig. 3.17a exactly as predicted by the black line in Fig. 3.6c.

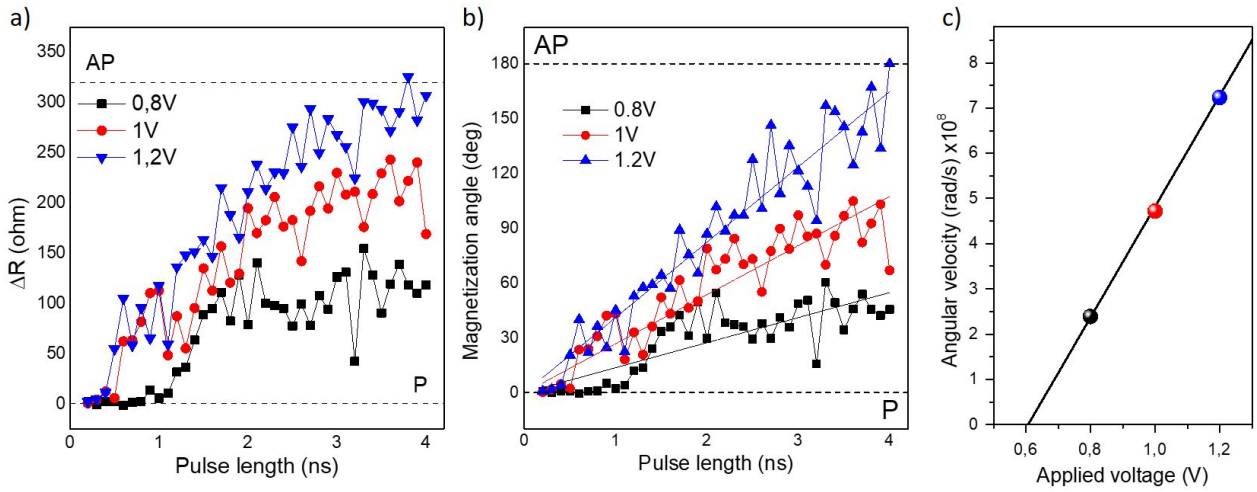

Fig. 3.17: Resistance evolution under a single pulse | **a.** Resistance jumps variation to a single pulse for different durations and amplitudes. **b.** In-plane angle of the magnetization varying with the pulse characteristics as in **a**. The black, red and blue fitting lines correspond respectively to angular velocity of the magnetization. **c.** Linear fitting of the angular velocity variation with the voltage amplitude. The measurements shown here are performed on a device with nominal diameter of 100nm, TMR around 30% and $R \times A \approx 8\Omega\mu m^2$.

3.4.2.2 Train of pulses

In the following experiment, a train of pulses is sent to the device to observe the evolution of its resistance. The device is set in the P state only at the beginning and not between two consecutive pulses as in the previous experiment. The pulses are designed in a way to not switch completely the magnetization but to rotate it so to reach several intermediate resistance values. For this reason, the voltage amplitude is set to 0.9V with a varying pulse duration for the results shown in the following. An important parameter chosen for this experiment is the delay between two consecutive pulses that is set to 1s so to give an idea of the thermal stability of the intermediate resistance states (discussed later in this chapter). The resistance variation to a series of 50 pulses of positive polarity is shown in Fig. 3.18a for different pulse lengths. The magnetization, that is not much affected by the 1ns pulses, gradually rotates towards the AP state proportionally to the pulse length. The resistance is then saturating to the AP state confirming that the effect of the double STT acts as in the unstable region of Fig. 3.6a and not as in OPP (for which the resistance is supposed to oscillate with the same polarity of the voltage). Note that the saturated states (both P and AP) measured by field (dashed lines in Fig. 3.6) may not always correspond to the one achieved by STT. This

difference is due to the fact that, while, during the application of a high field, the spins are forced in a single direction, the magnetic configuration after the application of a current pulse relaxes into a state where spins in-plane directions are spread over a smal angle (exactly as in the cartography in Fig. 3.12c). For this reason, the AP (P) resistance measured by field is generally higher (lower) than the one achieved by STT. In both zooms of Fig. 3.18a it can be stated that the intermediate resistance states turn out to be thermally stable along the 1s between the two pulses confirming the possibility to stabilize the magnetization along different in plane directions. Interestingly, the resistance jumps, due to the application of pulses, turn out to be not always monotonous with the pulse polarity (as in the two zooms of Fig. 3.18a). For this reason, the number of pulses needed to completely switch from the P to the AP state is higher than according to Fig. 3.17a (for which an average over 10 measurements reduces the random effect). This effect, that will be discussed in the next paragraph, is not dependent on the voltage polarity as evident in Fig. 3.18b. Even if the STT effect is evident in the monotonicity of the average resistance with the polarity of the voltage, the presence of random resistance jumps at the moment of the pulse injection persists also in the saturated P or AP values where the STT has no more effect. Note that the P-AP and AP-P transitions are asymmetric because of the dipolar field coming from both the uncompensated out-of-plane SAF and in-plane top SAF that favors the precession only towards one direction.

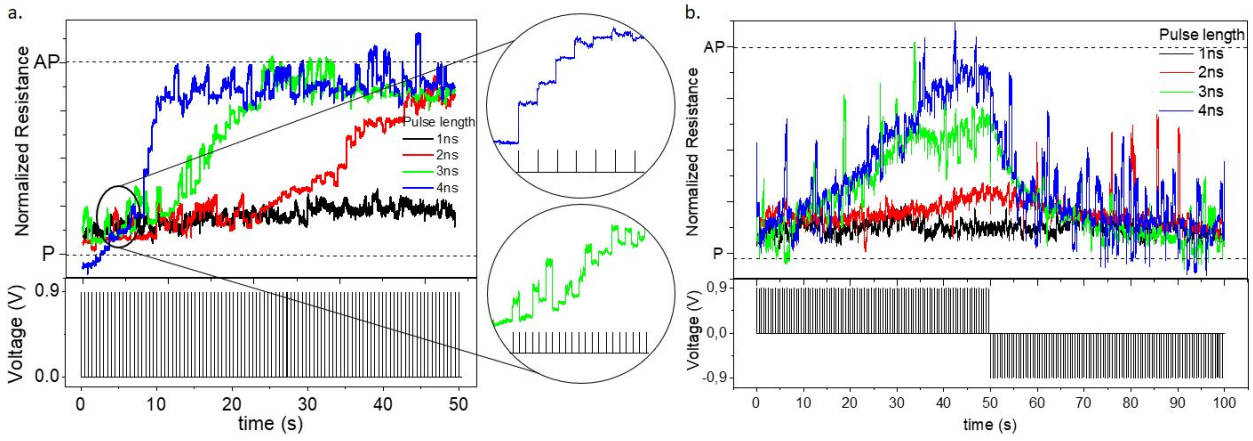

Fig. 3.18: Resistance evolution under STT | **a.** Resistance variation due to a train of pulses of 0.9V with varying pulse length and 1s delay between two consecutive pulses. In the zooms, the blue curve shows a monotonous behavior while the green curve exhibits an average monotonous trend of the resistance variation interrupted by random jumps. **b.** Resistance variation to a train of pulses of both polarities. The measurements shown here are performed on a device with nominal diameter of 100nm, TMR around 30% and $R \times A \approx 8\Omega\mu m^2$.

3.5 Temperature effect

As anticipated, the presence of a thin IrMn layer in the free layer, with a blocking temperature around 100°C (Fig. 3.11), makes this device quite sensitive to temperature. For this reason, the effects of temperature are investigated in terms of stability of the intermediate resistance states and Joule heating induced with the voltage pulses.

3.5.1 Thermal Stability

A first idea of the thermal stability of the resistance levels reached through STT is shown in the zooms of Fig. 3.18a. An example of resistance distribution of such curve is shown in Fig. 3.19a showing an almost continuous range of resistances achieved between the P and AP states.

To look at the stability of a single resistance level, only few level have been selected as in Fig. 3.19b. The distribution of such resistances show a FWHM below 3Ω, meaning a resistance variation

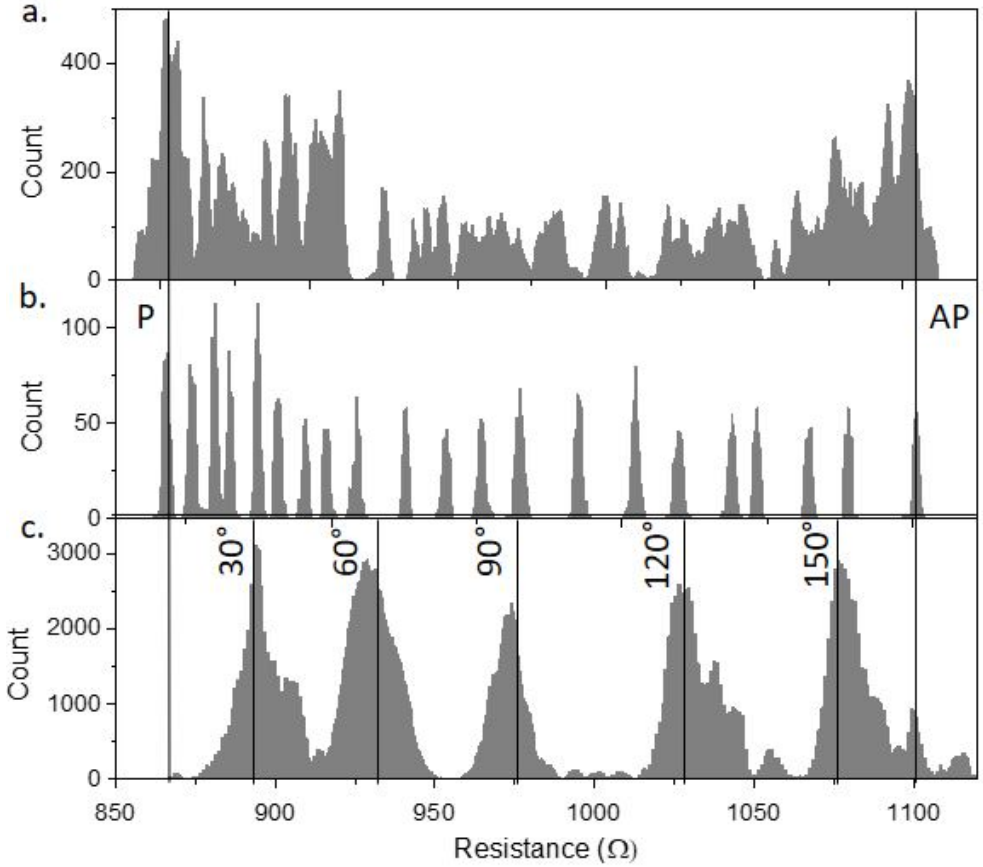

Fig. 3.19: Thermal stability | **a.**Resistance distribution in a multiple pulse experiment. **b.** Resistance distribution for few distinguishable levels. **c.** Resistance distribution for intermediate resistance values induced by field saturation at different in-plane angles for a 3min timescale. The measurements shown in this figure are performed on a 100nm MTJ with a $TMR \approx 26\%$ and $R \times A \approx 8\Omega\mu m^2$.

below 0.1% in a time range of 1s. To have a better idea of the thermal stability of the resistance states at RT, the magnetization is saturated, through the application of a strong in-plane field, in different directions and the resistance is measured for 3 minutes. As you can see from Fig. 3.19c, the FWHM is around 17Ω with a resistance variation below 2%. The results suggest that, for a device with TMR 100% and same RxA, a discrete number of intermediate states of 50 can be ideally used for applications that require an access to the value of such device in a frequency range higher that few Hz. Moreover, this confirms that the resistance jumps, observed in the previous experiment and that occur at the moment of the pulse, are mainly due to the Joule heating. This would mean that the randomness observed in the resistance during the application of the pulse could be due to a not fully macrospin switching of the magnetization.

3.5.2 Joule heating

To investigate this, the idea is to separate the effect of the resistance variation due to STT from the one due to Joule heating. For each polarity of the voltage, the STT is supposed to act only up to the saturation to the P or AP state (as for example in Fig. 3.20a). At this point, all the pulses applied are heating up the device with a negligible STT effect. A statistical analysis of the resistance jumps due to a train of pulses in the saturated AP state is shown in Fig. 3.20b for different pulse lengths in a device of 150nm of diameter. Interestingly, the distribution of jumps turn out to be peaked around an average value. This means that, when the magnetization is in the AP state, the temperature effect is to switch the magnetization of a relatively small part of the free layer so to

vary the total resistance. The fact that this variation is peaked with such distribution means that the area of the free layer to be switched is always the same. Moreover, this area tends to increase with the pulse length probably because of an increased temperature induced in the device (see Fig. 3.20c).

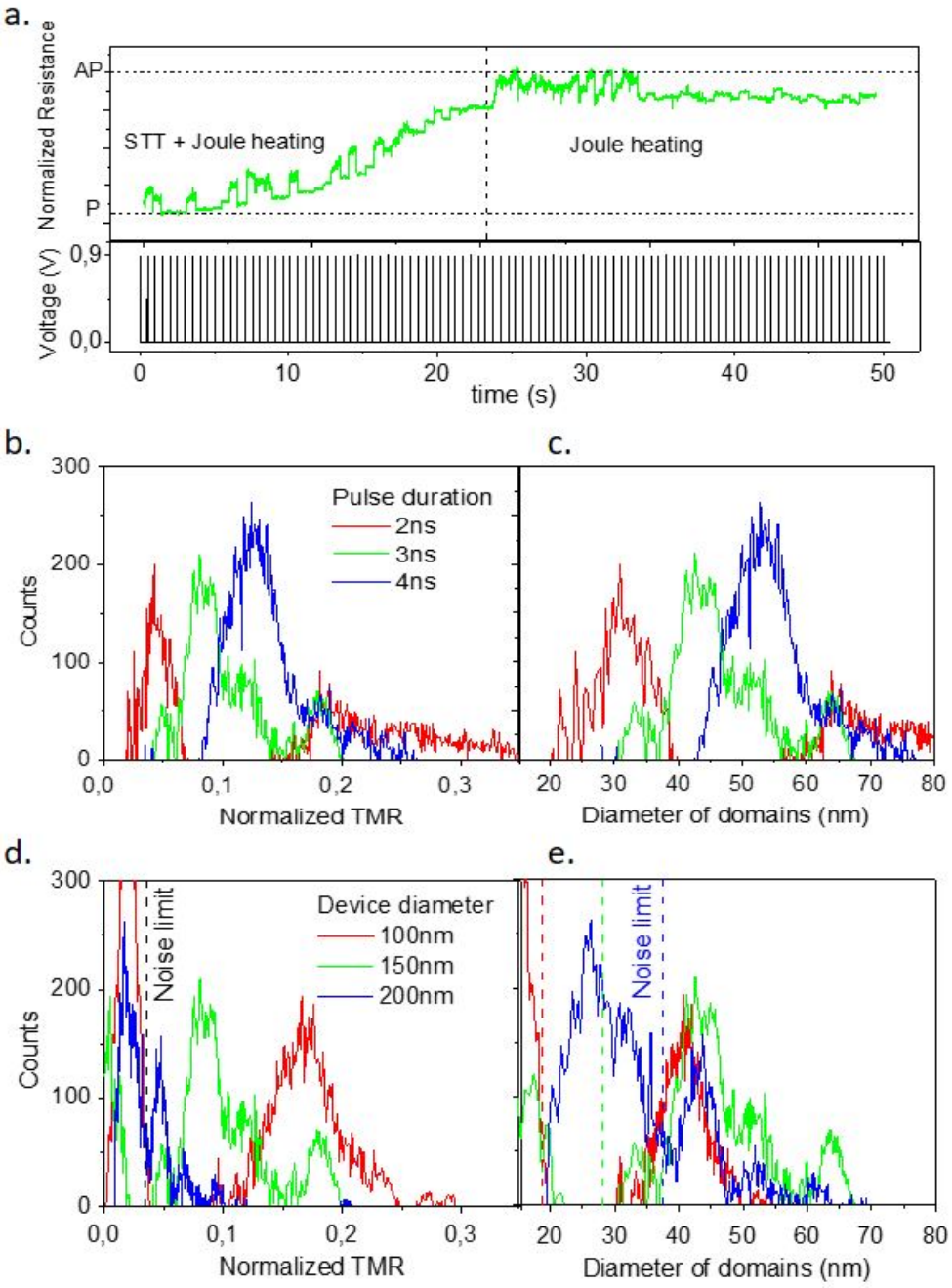

Fig. 3.20: Resistance jumps statistical analysis | **a.** Example of resistance variation with a train of pulses taken from Fig. 3.18a. **b.** Resistance jumps distributions for different pulse lengths for a 150nm MTJ with a $TMR \approx 32\%$ and $R \times A \approx 7\Omega\mu m^2$. **c.** Resistance jumps distributions as in b. normalized with respect to the device diameter. **d.**Resistance jumps distributions for different device diameters with similar properties and pulse length of 3ns. **e.** Resistance jumps distributions as in d. normalized with respect to the correspondent diameters.

This result suggests that the Joule heating activate the switching of small portions of the free layer as it would in an granular layer. To further investigate this, the same analysis is performed on devices with different diameters (with similar TMR and $R \times A$) with a fixed pulse length of 3ns. As shown in Fig. 3.20d, the resistance jumps appear in a similar peaked distributions independently

on the size of the device (the noise limit is taken at 2% accordingly to the previous measurement). Furthermore, the overall resistance variation seems to decrease with the increasing diameter of the device. By normalizing the distributions with respect to the size of the corresponding device, we find that the three distributions present the same average value around 45nm as shown in Fig. 3.20e. This means that the area of the free layer to be switched by Joule heating is always the same independently on the size of the device. This tends to confirm the idea of a uniform distribution of grains in the free layer. This phenomenon can be explained with the presence of the IrMn layer in the free layer. Its granular structure and its spin glass-like magnetic state (due to the small thickness that does not give rise to exchange bias, see Sec. 3.3.1) can create, through exchange interaction at the interface with the two ferromagnetic layers, a granular type of magnetic behavior in the free layer. Those could be switched because of the increasing temperature due to the Joule effect. This can be estimated in a MTJ within an unidimensional model through the expression

$$T(t) = T_0 + \frac{P_d A}{K}[1 - \exp(-\frac{t}{\tau})], \tag{3.19}$$

where T_0 is the initial temperature (RT), P_d the power density ($R \times AJ^2$), A the device area, K the proportionality between power density and temperature increase, τ the characteristic heating time (around 10ns for IrMn [171]) and t the pulse length [172]. Generally, for $t > \tau$, the temperature stabilizes to a value that depends on the prefactor of the exponential function. For $t < 5\tau$, the temperature increases rapidly with the pulse length t and almost independently on the device size. In this last working region, that better corresponds to the experimental results in Fig. 3.20, the final temperature can be relatively low. This is fundamental for a good functionality of this device since, as already said, the presence of the IrMn does not allow this device to work in a large temperature range. For this reason, it is fundamental the use of ns range pulses that are effective only thanks to the fast switching mechanism provided by the presence of the perpendicular polarizer.

3.6 Double MTJ structure

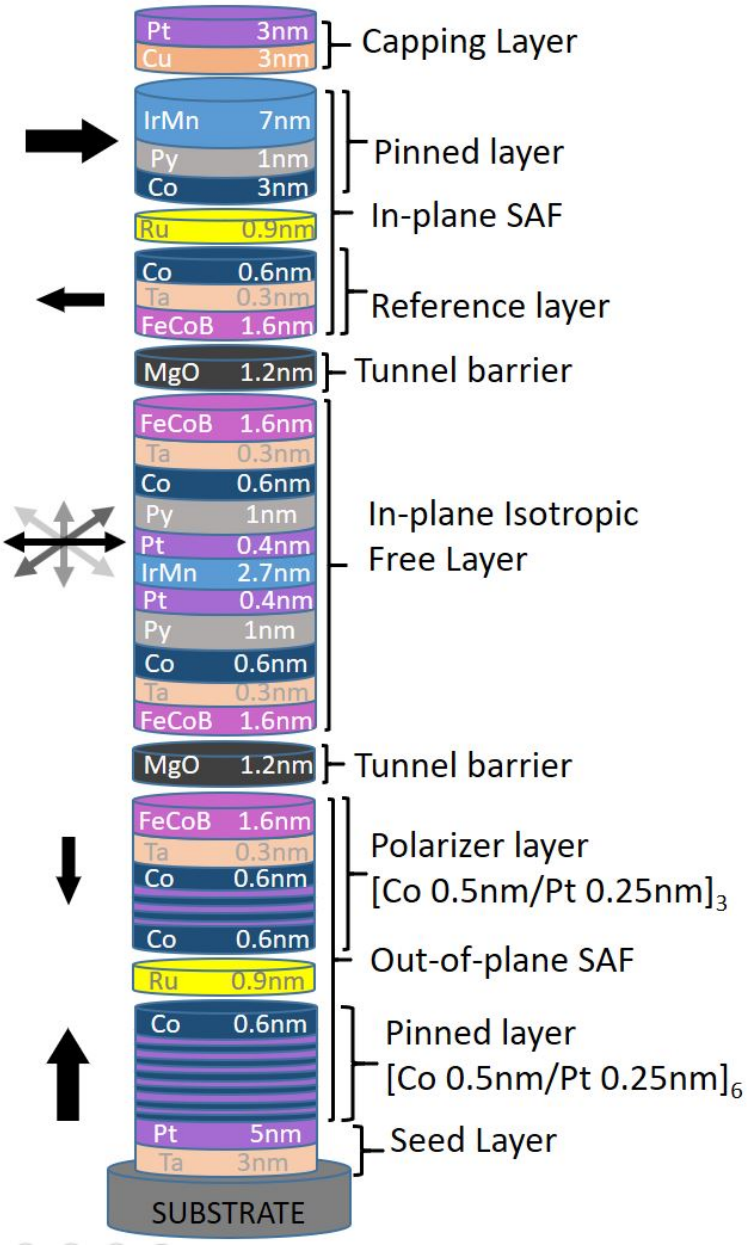

Fig. 3.21: Double MTJ structure | Schematic of the double MTJ stack and relative magnetization direction (black arrows).

In this section we explore the other working region of the device as in Fig. 3.6a, i.e. the OPP one. As already stated, in this case the use of similar STT efficiency for the two contributions would favour the out-of-plane precession of the magnetization for relatively low current densities (as in Fig. 3.6a). To fully exploit this region, we optimize a magnetic stack including two magnetic tunnel junctions as shown in Fig. 3.21. In addition to the previous magnetic stack, the insertions of FeCoB layers in contact with the bottom MgO barrier is expoited to improve the STT.

Remembering that the two junctions have different purposes (the bottom is supposed to be efficient in term of STT and the top one has to give better TMR), an optimization of the two barriers is necessary. In particular, for the top junction, we choose the barrier oxidation conditions in order to obtain the best TMR possible without important restriction to its $R \times A$, while, for the bottom one, a lower $R \times A$ is chosen to reduce the serial resistance of this second tunnel barrier which do not contribute to the overall TMR of the stack. For this reason an analysis at CIPTMR (see Sec. 2.2.3) is performed on different oxidation conditions (time and pressure) as shown in Table 3.2. As visible from the results, the barrier with $p = 3{\times}10^{-2} mbar$ and 30s of oxidation turns out to have good TMR with an $R \times A \approx 10 \Omega \mu m^2$ and, therefore, it is choosen as top barrier. For the bottom barrier, the reduction of $R \times A$ induced by lower oxidation pressures or time, implies a drastic reduction of TMR that is linked to a reduction of the spin polarization. For this reason, macrospin simulation on the influence of such $R \times A$ and spin polarization (extracted from the formula $\eta = \frac{\sqrt{TMR(TMR+2)}}{2(TMR+1)}$ [173]) on the threshold voltage are performed. As shown in Fig. 3.22, the total voltage needed to start the oscillations (sum of the voltages dropping on both junctions with a current density given by Eq. 3.9) seems to slightly reduce by lowering the $R \times A$ despite the evident decrease of spin polarization. The dashed lines, in fact, correspond to the lines with a constan value of the spin polarization taken from the 30s oxidation for each pressure (supposed to be the best oxidation time). This means that the deviation from this line of each sample with the same pressure condition is due to a decreased spin

	$3 \times 10^{-2} mbar$		$1 \times^{-2} mbar$		$3 \times^{-3} mbar$	
	TMR (%)	$R \times A(\Omega\mu m^2)$	TMR (%)	$R \times A(\Omega\mu m^2)$	TMR (%)	$R \times A(\Omega\mu m^2)$
30s	78	9.8	35.9	4.8	39.5	3.2
10s	38	5.4	36.2	4.1	25.8	2.3
5s	66	4.8	33.6	3.0	31.8	2.3
1s	56	3.6	38.7	3.0	27.3	1.2

Table 3.2: TMR and $R \times A$ values measured by CIPTMR for different values of oxidation pressure and time for a total Mg thickness of 1.2nm.

polarization probably due to a partial oxidation of the Mg layer. In this case, we choose as bottom junction the one obtained at $p = 3 \times 10^{-3} mbar$ and 1s of oxidation with an $R \times A \approx 1.2\Omega\mu m^2$.

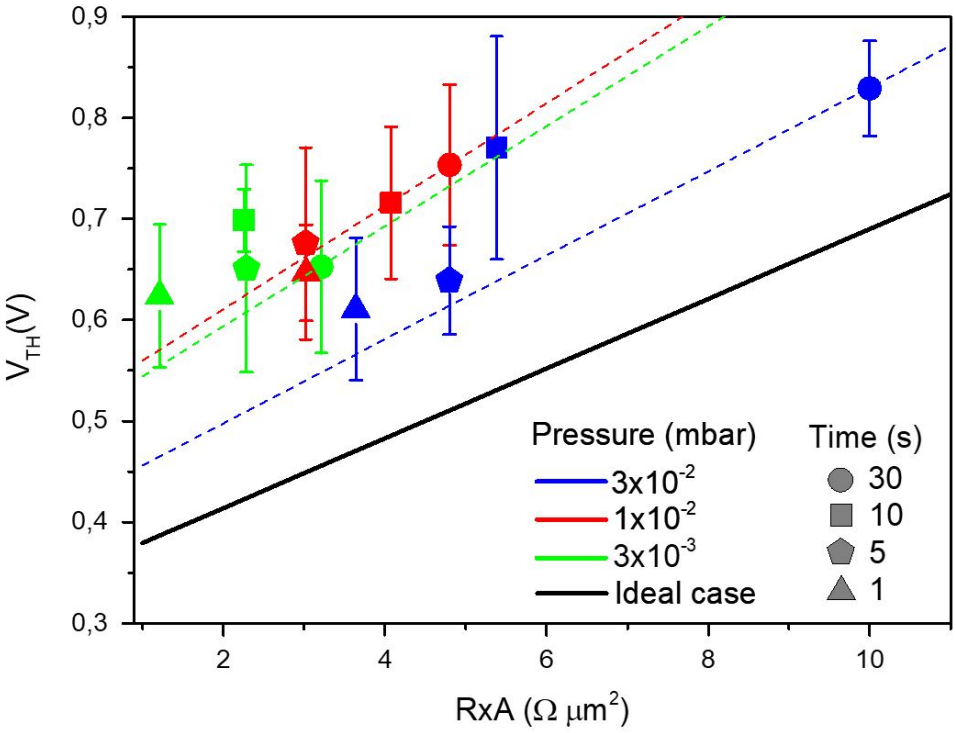

Fig. 3.22: Threshold voltage for OPP | Threshold voltage dependence on the bottom junction $R \times A$ for different oxidation pressure and time. The dashed lines represent the iso-lines for different spin polarizations (black 100%, blue 83%, red 68% and green 70%).

3.6.1 DC current-driven excitations

An experiment performed on this sample (as in Fig. 3.21) consists in injecting a dc current in order to observe directly the OPP as expected from the diagram in Fig. 3.6a. Here, in fact, we expect the bottom MgO to give a much higher spin polarization than in the case of a Cu spacer, resulting in an easier exitation of the wanted precession. The experiment is performed on the setup of the RF team in Spintec with the help of A. Litvinenko and U. Ebels. Initially a fixed current of 0.2mA is injected in the device and the field is varied in order to find an optimum amplitude of the peak. In the setup, this is done by manually moving a permanent magnet placed below the wafer. This allows to apply a wide range of field amplitudes and directions but without knowing them exactly. The results shown in Fig. 3.23 are performed on a device of 80nm of diameter, a TMR around 40% and an $R \times A$ around $15\Omega\mu m^2$. The results of these measurements are shown in Fig. 3.23a (the Power Spectral Density signals are vertically shifted for a better understanding). As visible from the black curve, without field, the frequency is spread around values of few hundreds

of MHz. As soon as a small field is applied, a peak appears around 1.7GHz with a very large bandwidth. The peak then shifts towards higher frequencies by increasing the field (note that the field increase is referred to its amplitude. The magnet initially far is displaced closer and closer up to an optimized position that is not perfectly under the device, i.e. an in-plane component of the field is always necessary. This is reasonable since an in-plane stray field of 20mT is affecting the device probably due to an uncompensated in-plane SAF).

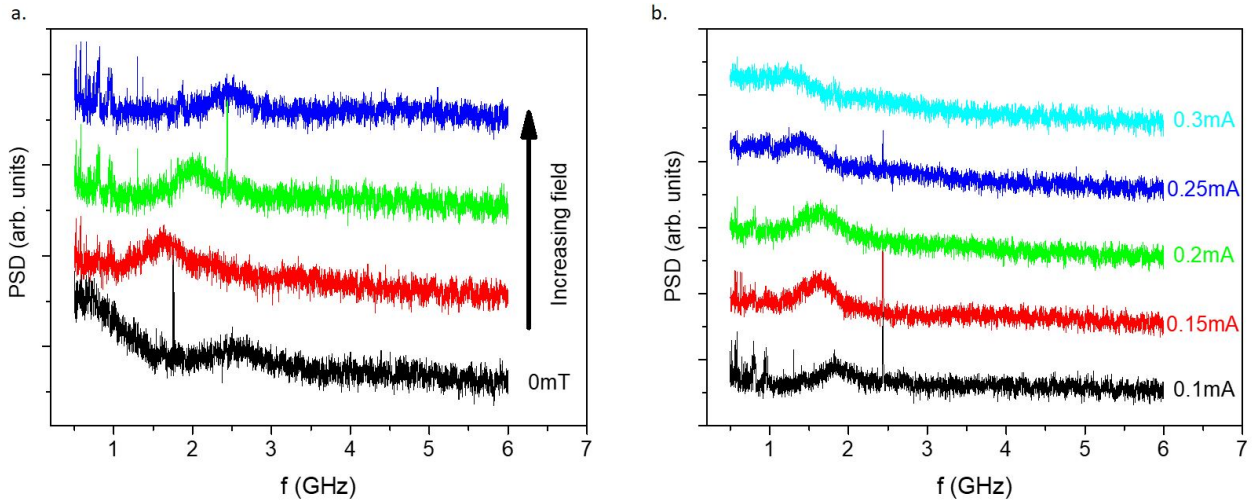

Fig. 3.23: DC current-induced oscillations | **a.** Power spectral density obtained at fixed input current (0.2mA) for different field values (the exact field amplitude is not measurable in the setup). **b.** Power spectral density obtained with a fixed field (position of the magnet) and increasing current value as indicated in the figures. In both images, the signals have been vertically shifted for a better understanding. The measurements shown here are performed on a device with nominal diameter of 80nm, TMR around 40% and $R \times A \approx 15\Omega\mu m^2$.

A second trial is made by fixing the magnet in a position that optimizes the peak amplitude and varying the injected current. The results are shown in Fig. 3.23b. The peak is slightly shifted towards lower frequencies by increasing the current from 0.1mA to 0.3mA contrarily to the predictions simulated in the paragraph 3.2.3.1. Also, the amplitude of the peak gradually reduces with the increase of the current. These characteristics, together with the very large bandwidth, could be a sign of the thermal origin of those signals. In fact, apart the very senstive nature of the free layer to the temperature (as stated in the paragraph 3.3.1.3), the current values used in this experiments do not provide an injected power high enough to induce oscillations in a 4nm layer with a dissipation mechanism enhanced by the presence of IrMn. This is due to the fact that the bottom barrier has a breakdown voltage much lower than the top one (demonstrating the lower quality of the barrier) and, therefore, the maximum injectable current is not enough to initiate the OPP. Despite this, thermally-induced excitation can exist, assisted by the STT from the dc current. As for the device with bottom Cu spacer, it is possible that, for very short pulses, the STT contribution to the magnetization dynamics becomes more relevant. To confirm this, a multiple pulses experiment is performed on this device in order to assess whether the memristive behavior of the device, as simulated in section 3.2.4.1, can be confirmed with the application of an in-plane field.

3.6.2 Pulsed current-driven excitations

The experiment is performed similarly to the one in section 3.4.2.2. A train of pulses of different pulse lengths and amplitudes have been sent through the device with a frequency of 1Hz or 2Hz. As observed in the previous experiments, the effect of the pulses on the resistance variation starts to be evident only for relatively high applied voltages ($\geq 0.9V$). An example of this is shown in Fig. 3.24 for a device of 100nm of diameter and TMR of 40% (applied pulses of 1V and 2ns at 2Hz).

Interestingly, the resistance, initially in the P state, rapidly varies when a pulse is applied, and it comes back to the initial state immediately after. Note that the resistance variations are much lower than the total TMR value. This means that the magnetization is not able to actually start the rotation because of the current density below threshold. As already said in the previous paragraph, the current density is limited by the low breakdown voltage of the bottom tunnel barrier. This is due to the fact that the low oxidation pressure used for the bottom MgO to obtain a lower $R \times A$ creates a poor quality barrier (demonstrated by the low TMR value as in table 3.2).

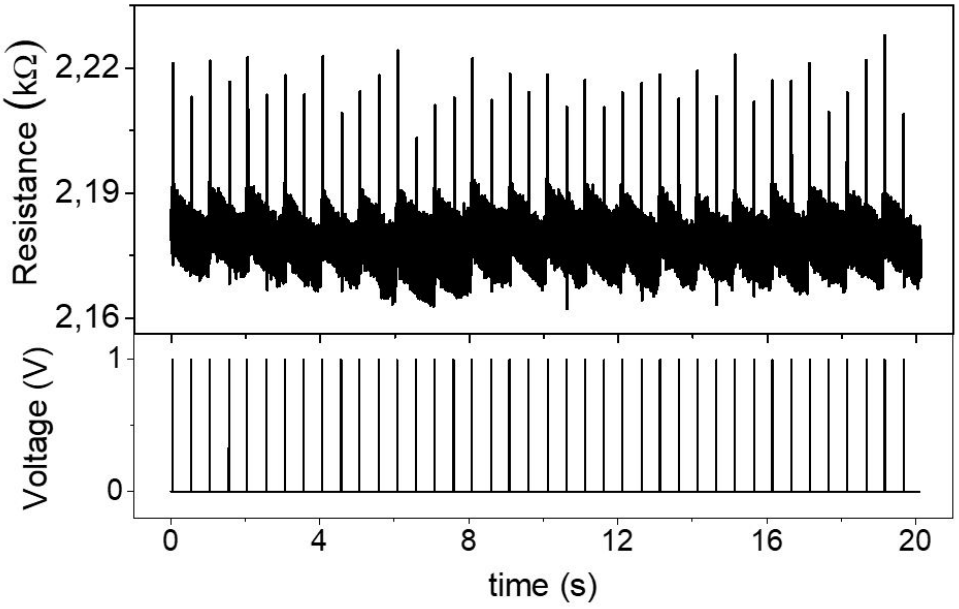

Fig. 3.24: Multiple pulse experiment | Resistance variation of a double MTJ structure to a train of pulses as in the bottom panel. The measurements shown here are performed on a device with nominal diameter of 100nm, TMR around 40% and $R \times A \approx 16\Omega\mu m^2$.

To try to solve this issue, other oxidation conditions have been used for the bottom barrier. A first trial is done with the one with $p = 3 \times 10^{-2} mbar$ and 1s oxidation time that gives an $R \times A$ around $4\Omega\mu m^2$ with a quite high TMR (better quality than the previous one) and it is close to the ideal voltage threshold (dashed blue line in Fig. 3.22). Also in this case, the results obtained are similar to the ones described above. This is due to the fact that, despite the better quality of the junction and the consequent higher breakdown voltage, the increase of $R \times A$ induces an higher voltage (always higher than the breakdown). A final trial with the bottom barrier with $p = 3 \times 10^{-2} mbar$ and 5s oxidation time gave no different results.

Finally the poor quality of the low $R \times A$ barriers (that were supposed to reduce the voltage below the breakdown threshold) reduces significantly also their breakdown voltage and their spin polarization. Despite this, the use of higher $R \times A$ would be negative for the readout of the device since an higher bias voltage would be required.

3.7 Conclusions

In this chapter we proposed a spintronic memristor based on the TMR dependence on the angle between the magnetizations of the two magnetic electrodes of an in-plane junction. We were able to model a free layer with isotropic coercive field thanks to an additional dissipative term in the LLG equation analog to the dry friction in the Newton's equation. The isotropic properties of such layer are simulated with a static and a rotating field finding in both cases the analytical solution to the modified LLG equation. The effect of the STT coming from the in-plane analyzer (used to obtain the TMR signal), placed on top of the isotropic free layer, turns out to be not effective to move the free layer magnetization. This is due to the initial stochastic movement of the free layer magnetization that is completely damped by the dry friction term. To avoid this stochasticity, and additional out-of-plane polarizer is placed underneath the isotropic free layer. In this way, the STT coming from it tends to pull the magnetization out-of-plane and induce a precessional motion around the demagnetizing field, thus, avoiding the stochastic movements and reducing the switching voltage. Finally, we find that, depending on the STT efficiency ratio between those two contributions, it is possible to achieve a memristive behavior in different working regions. In case of equal STT efficiencies (i.e. for equal barriers), the magnetization of the free layer is entering an OPP region for an applied dc current. In this case, the application of pulses with a pulse length equal to a fraction of the oscillation period makes the magnetization discretely rotate by a small angle. In this case, only thanks to the use of an in-plane field perpendicular to the analyzer magnetization, the free layer magnetization dynamics is restricted only to half plane (between P and AP states), making the resistance variation monotonous with the pulse polarity. The second working region exploits the low STT efficiency part of the perpendicular polarizer. In this way, its contribution is only destabilizing the free layer magnetization enough to be afftected by the main STT contribution coming from the in-plane analyzer. The magnetization turns out to switch between the P and AP state with a rotating trajectory (similarly to the precessional switching). Here, the use of properly designed pulses acts on the magnetization as in-plane discrete rotations between the P and the AP state. This means that the monotonicity of the resistance variation with the pulse polarity in ensured without the use of an applied field (as in the previous case).

In order to realize such device, the first challenge is to create a magnetic medium able to stabilize the magnetization independently on the in-plane direction. Here, we used the exchange interaction at the interface between two ferromagnetic materials and an antiferromagnet. This last is thin enough to not give rise to exchange bias because of a spin glass-like state in which there is not a unique Néel vector defined. We find that in full sheet fils, this trilayer structure has the same magnetic properties independently on the in-plane angle. Moreover, a planar Hall measurements setup allows to perform a rotating field experiment that turns out to be well fit by the model, extracting a realistic value of the dry friction parameter. We integrated this layer between a perpendicularly magnetized SAF based on Co/Pt multilayers (at the bottom) and an in-plane exchange biased SAF (at the top). A first sample used a Cu spacer between polarizer and free layer and an MgO barrier between free layer and in-plane SAF. In this way, the STT efficiency from the perpendicular polarizer becomes lower than the one from the top in-plane SAF. This allows us to realize the memristive functionalities without the application of any field. After the nanofabrication process, the isotropic properties of the free layer are confirmed and compared with the full sheet film properties, finding good agreements. In order to proof the memristive behavior, experiments under single current pulse and train of pulses were performed. We find that, as expected from the simulations, the resistance variation is monotonous with the pulse polarity for pulses from 1ns to 5ns. Also, an almost continuous range of intermediate states is found. More than 21 distinguishable resistance states were demonstrated. In this sample, the Joule heating turns out to have an important effect visible in the randomness of the resistance jumps during the pulse. A statistical analysis of these jumps shows that those are associated to the thermally activated switching of small magnetic areas of the samples, probably due to the granular nature of the sputtered samples. The larger the diameter, the lower the noise due to the increased number of grains.

The memristive functionalities in the OPP region are explored with a sample with two MgO barriers in order to have similar STT efficiency. A study on the oxidation conditions of the bottom barrier is made in order to optimize the switching voltage. It turns out that low $R \times A$ barriers can be used to reduce the switching voltage despite their lower quality. Three main barriers are tested in order to find the OPP region but only thermally induced precession are measured under dc current. Moreover, the application of a train of pulses is not effective on the magnetization. The total current density turns out to be limited by the breakdown voltage of the bottom barrier.

In conclusion, we create a device whose working principle does not depend directly on the lateral siwe of the device. Despite the difficulties created by the thermal sensitivity of the free layer and by the complexity of the device, the scalability could offer the solution to go towards a more macrospin behavior and to reduce the Joule heating, making of this device a good candidate for large scale integration.

Chapter 4

Memristor based on a granular structure of the free layer

Contents

In this chapter the working principles of a memristive device based on a granular free layer in an MTJ structure are described. The material development and the electrical results are detailed before a conclusive section.

4.1 Introduction

As already anticipated, in this chapter we propose a spintronic memristive device that exploits a granular nature of the free layer to gradually switch its magnetization. This layer, integrated in a MTJ stack, would give a number of intermediate states proportional to the number of grains in the free layer. The switching mechanism (STT in this case) acts in a probabilistic way through the application of properly designed pulses. A probabilistic switching curve (similarly to a switching probability for a binary device) determines the pulse amplitude and duration to be used in order to switch a certain percentage of the total number of grains. The main challenge in the realization of such device is the material development for the realization of the granular magnetic medium.

In section 4.2, the challenges and the final methods for the granular material development are detailed.

In section 4.3, patterned devices are measured at room temperature and in a low temperature setup for a better understanding of the device characteristics and problematics.

In a final section 4.4 the chapter is summarized before a brief description of the perspectives.

4.2 Material development

The development of materials for magnetic recording dates back to the end of 19^{th} century for the realization of audio recording [174]. The idea to realize an ultradense storage memory device relies on the growth of magnetic grains with a high thermal stability and non magnetic grain boundaries in order to be isolated from their neighbors and avoid any coupling (that leads to higher bit error rates) as in Fig. 4.1a [175]. Along the years, the continuous scaling down to increase the areal storage density led to the creation of several solutions to improve the performances of such technology. In fact, while initially in-plane magnetized grains were used to carry the information [176], the scalability problems as the reduced thermal stability (due to the reduced magnetic volume) or the increased SNR due to the presence of more than one easy axis in each grain, led to the advent of perpendicularly magnetized recording media (PMR). Initially proposed by Hitachi and based on CoPtCr [177], PMR is the main technology used nowadays. The average grain size in this technology is 6nm of diameter (and 10nm of thickness) with a thermal stability that, similarly to the one required for STT-MRAM, allows a retention time around 10 years. Recently, the scalability of such technology reached its limit since a further reduction of the grain size leads to an increased anisotropy and, therefore, to an increase writing field (that is limited to 2.4T because of material properties). For this reason, the most recent developments of such technology are related to the reduction of the writing field in order to improve the scalability. Some examples of this are the antiferromagnetically coupled grains [178] [179] [180], or even the use of a soft magnetic underlayer that was developed to mirror the writing field in order to ease the writing of the bit. This allowed to increase the vertical component of the write field leading to the use of media with higher perpendicular anisotropy and, therefore, enhanced thermal stability [181] [182] [183]. Other ideas include the thermally assisted recording (where an heating process is used during the writing process to lower the switching field of the grain) [184] [185] and magnetic nanoparticles media [186] [187]. Generally, all those years of development led to an important amount of knowledge for the control of the magnetic properties of the grains and, consequently, to an extreme control of their growth.

In this work, we aim to obtain a granular material to be able to exploit its magnetic properties in the storage layer of a perpendicularly magnetized tunnel junction as shown in Fig. 4.1b.

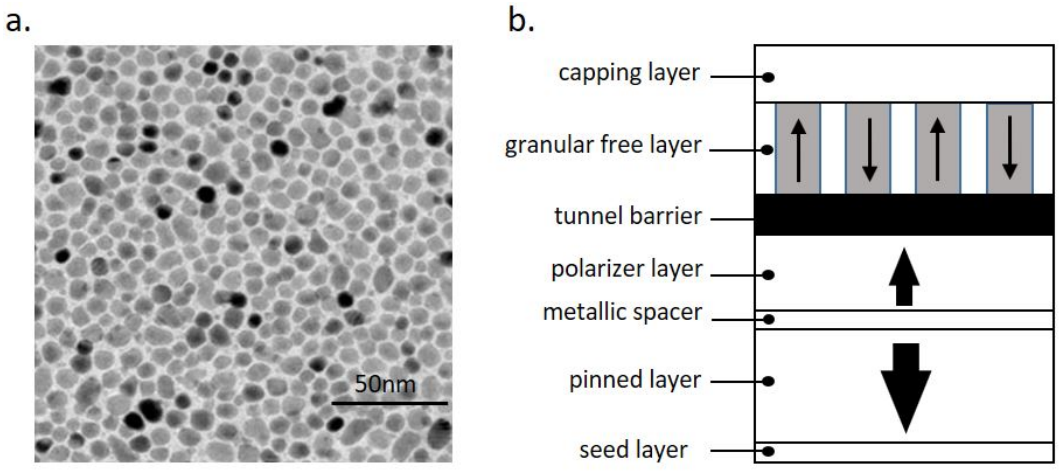

Fig. 4.1: Granular materials | **a.** Top view TEM image of a granular medium of FePtAg – C [188] **b.** Schematic of the cross section of the perpendicular MTJ with a granular free layer.

Generally, the use of immiscible materials (one of which being magnetic) in a sputtering machine able to deposit both at the same time (co-sputtering) is exploited to grow such granular structure in a controlled way. The relative content of the two materials has to be chosen dependently on the ratio between the area of the magnetic grains and their separation. The size of the grains has to be small enough to allow a good statistics in a relatively small MTJ pillar (below 100nm) and big enough to have sufficient anisotropy and avoid superparamagnetism at room temperature. Typically, sizes

between 2nm and 10nm are required. The thickness of the grain boundaries is designed to reduce as much as possible the magnetic coupling between neighbor grains; it is typically around 1nm to 2nm. In this way, the inter-grain exchange interactions or dipolar couplings are not able to significantly influence the magnetic state of each grain. Moreover, since the switching mechanism is a current induced effect, using such granular structure may be advantageous since it allows to maximize the current density in the inner part of the grains. For these reasons, we chose to develop a granular layer made of FeCoB grains and Al_2O_3 boundaries. In order to have the wanted grain and boundaries dimensions a ratio of the two materials $FeCoB_x/(Al_2O_3)_{1-x}$ around $x = 60\%$ to 70% should be used. The possibility to fabricate granular heterogeneous alloys with these two materials has already been demonstrated in earlier studies [189] [190] [191].

In this work, the non availability of a co-sputtering machine and of an Al_2O_3 target put into play an higher number of variables for the realization of such magnetic medium. The solution that we found to the absence of a co-sputtering machine exploits the sputtering deposition of a multilayer structure made of the repeated alternations of FeCoB and Al. In this case, when each deposited layer has a very low thickness, an alloy rather than a multilayered structure is formed. Thanks to a subsequent preferential oxidation of the Al into Al_2O_3 and a temperature annealing, the demixing of the two materials is induced. In this particular situation, the immiscibility of the two materials tends to create aggregates that, for a given ratio of the two materials, yields the granular structured layer which serves as storage layer in our memristive device. This method, never used in Spintec, is exploited for all the samples presented in this section.

4.2.1 Oxidation conditions

The first big challenge in the development of such granular structure is the control of the selective oxidation of the Al. In fact, due to the absence of the Al_2O_3 target in the deposition machine, the formation of the oxide accompanying the demixing occurring during the annealing is a critical issue. The reason for this criticality lies in the fact that the remaining Al is miscible with FeCoB and, therefore, does not demix. Besides, during the oxidation process, Al should get easily oxidized since the enthalpy of formation of Al_2O_3 ($\approx -1669.8 kJ/mol$) is much lower than the one of Fe_3O_4 ($\approx -1120.9 kJ/mol$) or CoO ($\approx -239.3 kJ/mol$). Only the Ta_2O_5 has a lower enthalpy of formation ($\approx -2046.3 kJ/mol$) but it does not represent a problem since it serves as B absorber and, therefore, only 0.3nm of thickness is used.

In this section, we show the methods that we used to oxidize the Al layer before the annealing. To do this, we compare three samples to which we applied three different oxidation conditions.

- **Sample A** | In a first trial, as in Fig. 4.2a, the multilayer of FeCoB and Al is integrated between two MgO barriers to increase the perpendicular magnetic anisotropy. The two Al layers are deposited as a wedge and each of it is directly oxidized with very high pressure (150mbar) and for a total time of 10s (those are the classical oxidation conditions used in the deposition machine to oxidize the Al). The sample magnetic properties, mapped with NanoMOKE (see 2.2.2) before annealing, results in a total absence of signal. This is expected since each individual FeCoB layer is too thin to be magnetic at room temperature. After annealing at 300°C for 10 minutes (optimum conditions for the MgO crystallization), the magnetic properties mapping shows still no signal. In this case, the problem is likely due to the creation of a continuous planar Al_2O_3 barriers that does not allow the demixing.

- **Sample B** | For this reason, the other trials that we made relied on the deposition of the multilayered structure FeCoB/Al as in Fig. 4.2b. The oxidation step then consists in a longer oxidation of the stack after the deposition of the Mg layer (60s instead of 30s at $p = 3 \times 10^{-2} mbar$). In this way, after the full oxidation of the Mg layer, the oxygen in excess tends to migrate towards the rest of the stack. At this point, the very low enthalpy of formation of the Al_2O_3 favors the creation of the wanted oxide. In this step, the thickness of the Al layers is a critical parameter since an excess of oxygen would affect the FeCoB layer and, as consequence, the granularity and the magnetic properties of the final structure. As in

the previous case, the magnetic properties of the sample are not measurable before annealing confirming the good quality of the deposition. The coercive field mapping of this sample after annealing (300°C for 10 minutes) is shown in Fig. 4.2d (in the figure, the total Al thickness is varying along the y axis from 0.4nm at the bottom to 0.9nm at the top). The presence of a magnetic signal is a sign that the demixing during the annealing led to the creation of a FeCoB layer thicker than before annealing. Moreover, the slow variation of the coercive field along the y axis can be related to the fact that, by increasing the Al content, the FeCoB is less oxidized since the oxygen tends to create Al_2O_3. Despite this, the very small coercive field variation all over the wafer indicates that the oxidation is not that effective (the zero coercivity zone on the top is an artefact of the NanoMOKE due to a spatial shift of the laser spot). This can be due to the relatively low pressure used in this step.

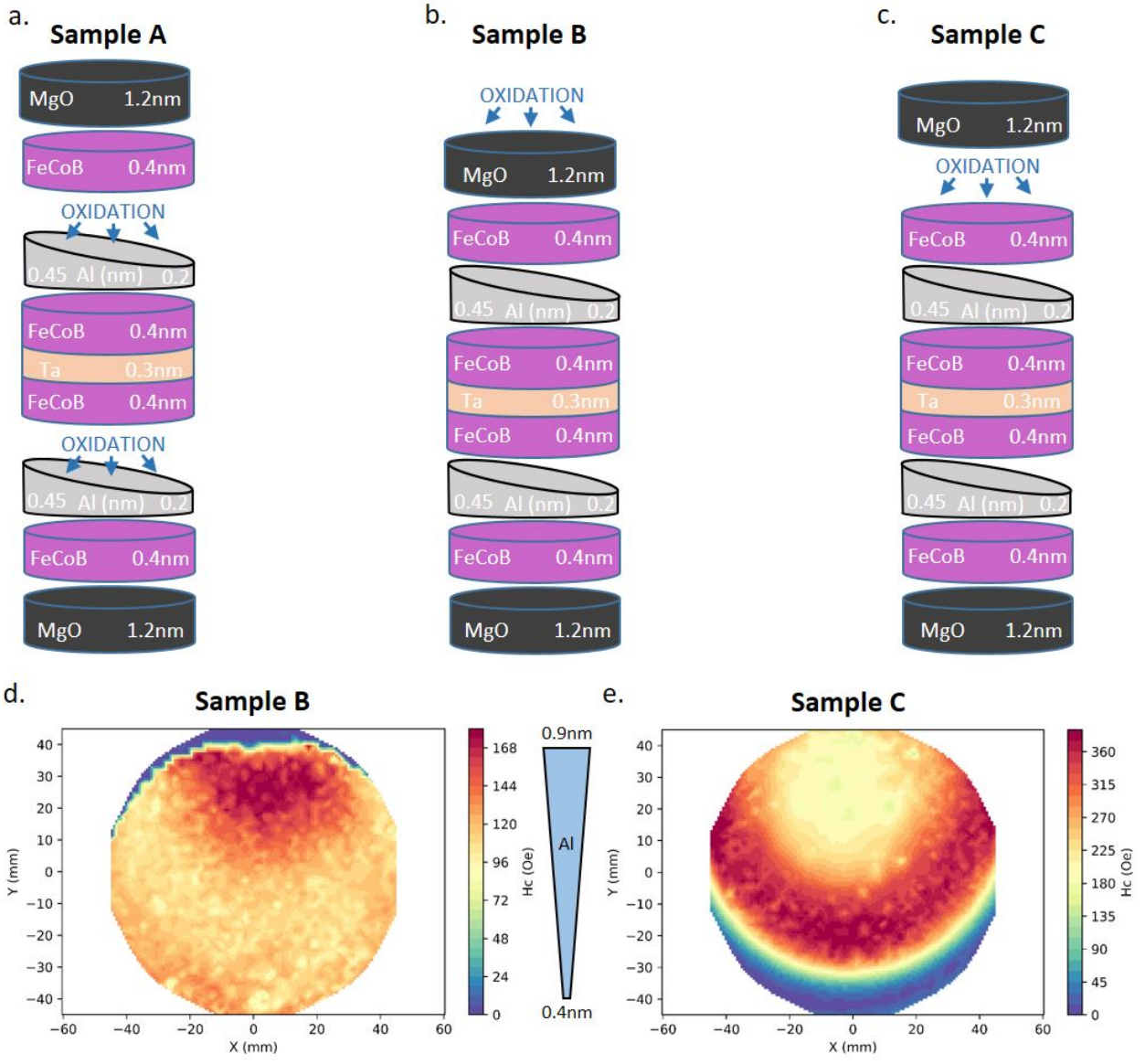

Fig. 4.2: Oxidation conditions for Al_2O_3 | **a.** Sample schematic with an oxidation step after each Al deposition. **b.** Sample schematic with a longer oxidation time for the top MgO layer. **c.** Sample schematic with an oxidation step before the top MgO deposition. **d.** Coercive field mapping after annealing for the sample as in b., with an Al wedge along the y axis from 0.4nm to 0.9nm. **e.** Coercive field mapping after annealing for the sample as in c, with an Al wedge along the y axis from 0.4nm to 0.9nm.

- **Sample C** | For these reasons, in the last trial, in Fig. 4.2c, the oxidation step was done before

the last MgO deposition and with the oxidation conditions as in the first sample (150mbar for 10s). Similarly to the previous sample, we expect the formation of Al_2O_3 and the demixing of the two phases to form the desired granular structure after annealing. As in the two previous samples, there are no measurable magnetic properties before annealing. In Fig. 4.2e the coercive field mapping after annealing (300°C for 10 minutes) is shown. Along the y axis, where the total Al thickness varies from 0.4nm at the bottom to 0.9nm at the top, there is a sharp transition of coercive field followed by a maximum close to the cental part and a slow decrease right after. This can be explained by the fact that, for very low thickness of Al (bottom), the oxidation mostly affects the FeCoB layers degrading the magnetic properties. For a critical thickness of the Al layer, all the oxygen tends to form Al_2O_3 and, therefore, the coercive field of the FeCoB layer tend to increase up to a maximum value where, ideally, the whole amount of Al is oxidized. By keeping increasing the Al content, the excess of material, that is not oxidized, diffuses creating an alloy with the FeCoB. In this way, the magnetic properties start to slowly degrade as in the top part of the mapping.

Finally, considering the positive effect of the oxidation on this last sample, the oxidation conditions used in **Sample C** as in Fig. 4.2c are the ones used for the set of samples presented in the following.

4.2.2 Magnetic stack optimization

After the optimization of the oxidation conditions for the formation of Al_2O_3, here we present the material development for the creation of the granular medium. The influence of the ratio of the two materials has been investigated in order to obtain the suitable magnetic properties and granular structure. In order to do this, we deposited a wedge of FeCoB along the x direction and a wedge of Al along the y one as shown in Fig. 4.3a in **Sample C1**. In this way, it is possible to obtain all the combinations of thicknesses of the two materials spatially distributed on the wafer and, therefore, the associated magnetic properties. Coercive field, remanence and amplitude of such sample are respectively shown in Fig. 4.3b, c and d. It is evident that a relatively sharp transition occurs between a non magnetic region (bottom left part of the wafer, for low FeCoB and low Al thickness) and a magnetic one. Along the Al wedge, this transition marks the critical value of Al content for which it gets all the oxygen. This means that, for Al content lower than this critical line, the oxygen in excess tends to partially oxidize the FeCoB (leading to a layer thin enough to be paramagnetic at RT), while, for higher Al content, the excess of Al, that does not get oxidized, tends to diffuse in the FeCoB, degrading gradually the magnetic properties. Moreover, the evolution of the magnetic properties along the FeCoB wedge is expected since its thickness goes from a total of 0.8nm, that is paramagnetic at RT, to 1.6nm where the magnetization starts to be in-plane.

In order to more deeply investigate these properties, the total FeCoB layer thickness was fixed to 1nm. The magnetic transition for this thickness of FeCoB occurs for an Al thickness around 0.55nm. **Sample C2** with a wedge as in Fig. 4.4a was deposited and annealed in order to have an extended transition region in the wafer. The coercive field mapping in Fig. 4.4b, shows how the magnetic properties of such sample are very senstive to the material thickness despite the zoom in the Al wedge between 0.5nm and 0.6nm. This is confimed by the cylindrical symmetry effect visible in Fig. 4.4b that is due to the variation of the total thickness deposited by the sputtering tool between the central part of the wafer and the edges (see 2.1).

In order to find and to prove the existence of the granular structure, different characterization techniques have been used on **Sample C2** depending on the positions as in Fig. 4.4b.

- More accurate magnetic measurements were performed by VSM on different parts of the sample numbered as in Fig. 4.4b. The resulting coercive field and amplitude obtained in those positions are plotted in Fig. 4.4c. Coerently with the NanoMOKE mapping, the coercive field rapidly increases and saturates to a value around 30mT. More interestingly, the amplitude curve turns out to be not monotonous as the coercive field. Its initial increase, parallel to the coercive field one, can be explained by the fact that, as previously said, the increasing quantity of Al tends to form more and more Al_2O_3 thus limiting the oxidation of the FeCoB.

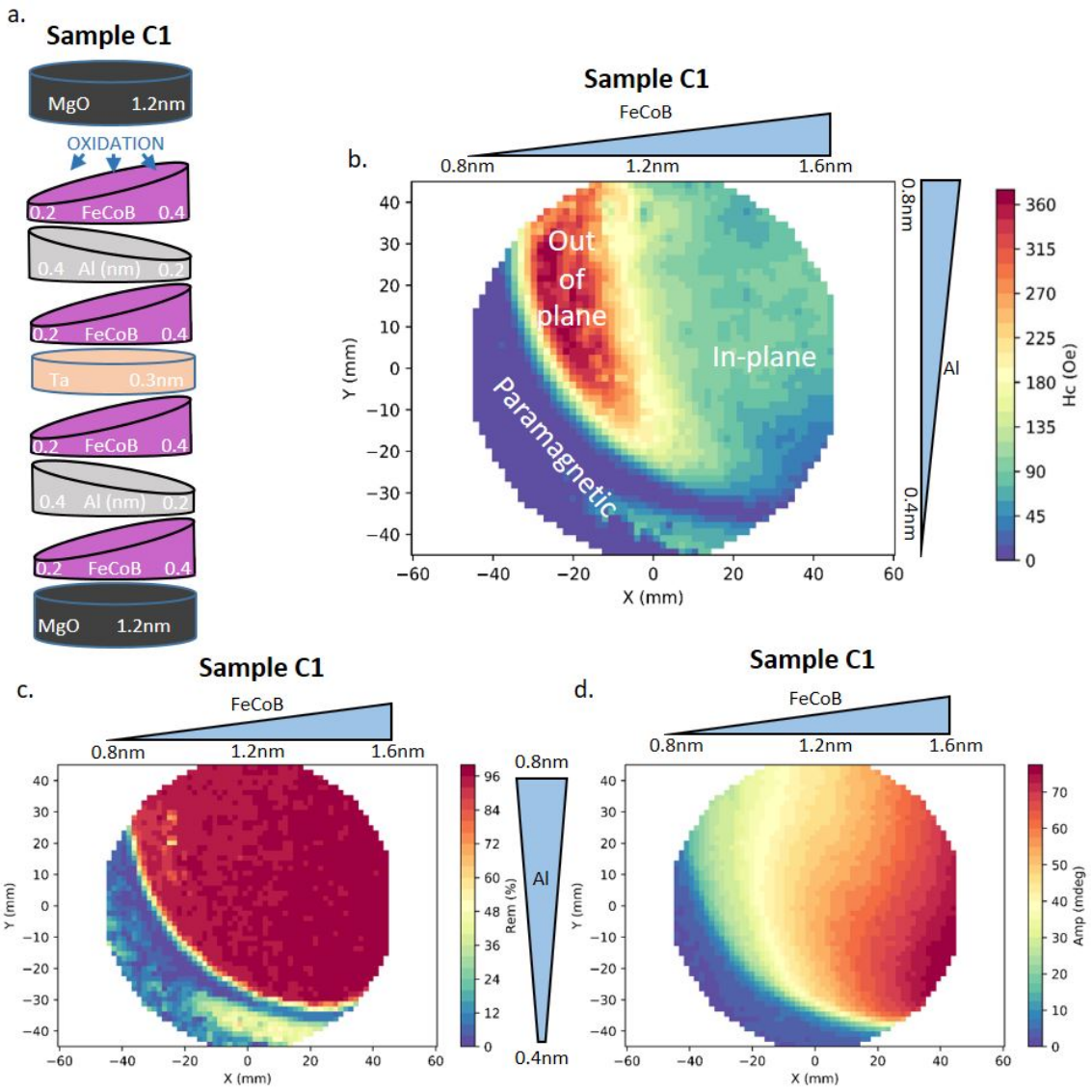

Fig. 4.3: Material optimization | **a.** Sample schematic with double wedge on FeCoB along x and Al along y. **b.** Coercive field mapping after annealing for the sample as in a. **c.** Remanence mapping after annealing for the sample as in a. **d.** Amplitude mapping after annealing for the sample as in a.

This means that the evolution of the magnetic properties up to position 4 of Fig. 4.4b, is related to an increasing quantity of FeCoB. At position 4, the peak in the amplitude, sign of a maximum value of M_S, is probably due to the fact that the full FeCoB layer is magnetic and the Al is fully oxidized. Therefore, a further increase of the Al thickness would imply that the Al is not completely oxidized. The remaining metallic Al would tend to diffuse into the FeCoB during the annealing. The reduction in the amplitude of the signal shown at positions beyond 4 can confirm this assumption. In this sense, the magnetic properties obtained around position 4, where the coercive field is not yet at its maximum value, look suitable for the formation of grains since a correct demixing between FeCoB and a fully oxidized Al_2O_3 seems to occur under these conditions.

- For a first confirmation of this, a resistance measurement was performed at full sheet film level with a technique similar to the one used by CIPTMR (see Sec. 2.2.3). In this $current - in - plane$ (CIP) configuration, we expect to have a relatively low resistance on the sample before annealing since the current would flow only in the metallic part of the multilayer structure. After annealing, instead, the creation of grains perpendicular to the surface as in Fig. 4.1b,

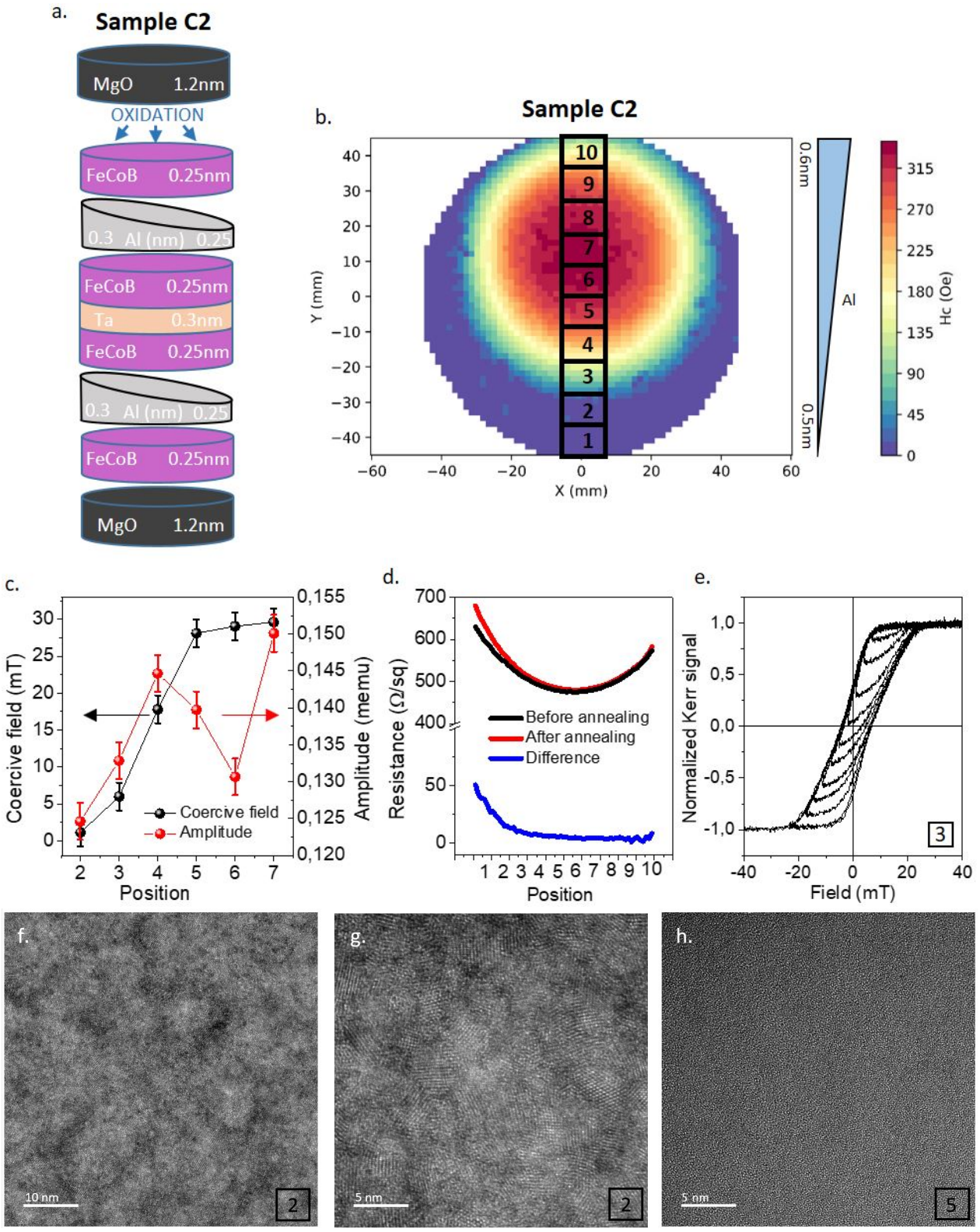

Fig. 4.4: Material properties | **a.** Sample schematic with a wedge on the Al layers. **b.** Coercive field mapping after annealing for the sample as in a. **c.** Coercive field and amplitude variation with the position as indicated in b. measured at VSM. **d.** Resistance variation with the position as indicated in b. before and after annealing. **e.** Minor hysteresis loops obtained in position 3 by NanoMOKE. **f.** STEM image obtained in position 2. **g.** Zoom of STEM image obtained in position 2. **h.** TEM image obtained in position 5.

would result in a significant increase of the resistance in the CIP configuration. The results, shown in Fig. 4.4d, show that the resistance varies after annealing for positions in the wafer up to 5. Despite this, the variation detected is quite small with respect to the expected one for which a transition from metallic behavior to insulator-like is supposed to occur.

- Another experiment that could confirm the formation of a granular structure between position 1 and 4, is the partial magnetization reversal with field. A series of field loops with different amplitudes is realized in order to observe whether the magnetization undergoes intermediate reversal configurations. This is a sign of the presence of a certain distribution of grain size that can be switched by different critical field amplitudes. The result in Fig. 4.4e obtained at position 3, along the transition, shows that several intermediate magnetization configurations can be obtained between the two saturated states. This result cannot be reproduced in other positions of the wafer because of the straight transition between the two saturated states.

- At this point, as several results suggest the possibility of having a granular structure between positions 2 and 4, TEM imaging was used to confirm this interpretation. The sample as in Fig. 4.4b was deposited on a substrate with an array of SiN membranes placed along the Al wedge (y axis). In this way, after a proper process on such membranes, we were able to realize TEM images of the top view of the sample for different Al contents. As expected, the presence of grains was detected at position 2 as visible from the STEM images in Fig. 4.4f and g. The polycrystalline layer shows grain size between 2nm and 3nm of diameter explaining the paramagnetic nature of the sample. By further increasing the Al content the granularity tends to reduce up to completely disappear at position 5 (Fig. 4.4h).

The set of information coming from all these experiences suggests that a granularity of the magnetic layer is obtained even if not as in the ideal case sketched in Fig. 4.5a. Instead, it is possible that the oxidation is much more effective on the first Al layer and on the thin Ta interlayer, and it does not reach the second Al layer in the bottom (as in Fig. 4.5b). This leads to a strong oxidation of the material at the interface with the top MgO, to the formation of a granular structure (visible in the TEM) in the part above the Ta, while, below, the Al not oxidized forms an alloy with the FeCo that is almost continuous (explaining the relatively small CIP resistance variation after annealing).

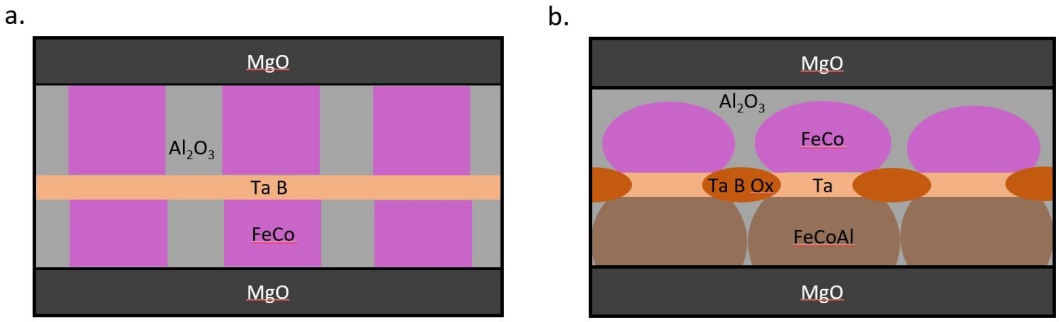

Fig. 4.5: Material phenomenology | a. Schematics of the cross section of the wanted granular structure. **b.** Schematics of the cross section of the structure obtained.

Finally, despite the complexity of the structure, we realized a granular material that, because of the low Al content, is more comparable to a FeCoB layer full of Al_2O_3 defects. Unfortunately, the critical thicknesses and the oxidation conditions choosen, led to the formation of grains that are paramagnetic at room temperature.

Such free layer, as in Fig. 4.4, was integrated in a perpendicularly magnetized MTJ with a reference layer made of a
$[Co(0.5)/Pt(0.25)]_6/Co(0.6)/Ru(0.9)/[Co(0.5)/Pt(0.25)]_3$
based SAF with an additional FeCoB at the inteface with MgO. The sample was patterned in nano pillars with diameters between 80nm and 300nm with the nanofabrication process as in Sec. 2.3. The electrical results of such devices are detailed in the next section.

	OXIDATION CONDITIONS			MATERIALS	
NAME	pressure (mbar)	time (s)	position	FeCoB	Al
Sample A	150	10	after each Al depositon	1.2nm	Wedge along y 0.4nm to 0.9nm
Sample B	3×10^{-2}	60	after the MgO capping	1.2nm	Wedge along y 0.4nm to 0.9nm
Sample C	150	10	before the MgO capping	1.2nm	Wedge along y 0.4nm to 0.9nm
Sample C1	150	10	before the MgO capping	Wedge along x 0.8nm to 1.6nm	Wedge along y 0.4nm to 0.8nm
Sample C2	150	10	before the MgO capping	1nm	Wedge along y 0.5nm to 0.6nm

Table 4.1: Resume of the samples for the material development

4.3 Electrical results on patterned devices

In this section the set of electrical results obtained on patterned devices are discussed. The deposited stack presents an out-of-plane magnetized SAF
$[Co(0.5)/Pt(0.25)]_6/Co(0.6)/Ru(0.9)/[Co(0.5)/Pt(0.25)]_3$
followed by the free layer as in **Sample C2** (Fig. 4.4a). The 4 inches wafer fabricated presents a wedge in the Al layer since the magnetic properties are very sensitive to the Al thickness, as previously described, and the deposition of a constant layer would have been subject to non uniformities coming from the deposition tool (see 2.1). The mapping of the magnetic properties of the wafer before patterning are shown in Fig. 4.6a. The mapping of the electrical and magnetic properties of the wafer after patterning are shown in Fig. 4.6b, c and d. As evident from Fig. 4.6b, the coercive field distribution of the devices in the wafer corresponds to the one measured at full sheet film with NanoMOKE (in Fig. 4.6a) (the increase of the average value is expected after patterning because of the reduction of the demagnetizing energy). This demonstrates that the nanofabrication process did not impact in an evident way the properties of the materials deposited. We note that the TMR mapping in Fig. 4.6c shows a very low average value. This can be due to the presence of a FeCoAl alloy at the interface with the bottom MgO as in Fig. 4.5b. Also, the very high $R \times A$ values, shown in Fig. 4.6d, are a clear sign of the presence of a series resistance. In fact, despite an overall increase of resistance is expected in case of a proper granular structure (with respect to a classical multilayer structure) as in Fig. 4.5a (since the metallic area is supposed to be significantly lower than the total device area), this would be limited to few tens of $\Omega\mu m^2$ (the value for a classical MTJ of $\approx 10\Omega\mu m^2$ is expected to increase from 2 to 5 times). In this case, the measurement of values around few hundreds of $\Omega\mu m^2$ is compatible with the presence of Al_2O_3 at the interface with the top MgO capping layer (as in Fig. 4.5b).

In order to further investigate the properties of such sample, additional measurements were performed at different positions on the wafer (corresponding to different Al content).

In the central part of the wafer ($X = 0, Y = 0$), for higher Al content, despite the absence of granular structure, the presence of Al diffused in the FeCoB layer may create a magnetic medium able to nucleate and pin domain walls. This mechanism may be used for a memristive behavior similarly to [115], but with a denser and more uniform distribution of pinning sites that would improve the scalability of the device. Despite these expectations, the experiments performed on such devices, described in section 4.3.1, demonstrate their binary nature.

In the bottom part of the wafer ($X = 0, Y = -35$), for lower Al content, the granular structure of the free layer may lead to the expected memristive behavior described in the introduction. In this case, the paramagnetic nature of the free layer due to the very small size of the grains forces us to characterize such devices at temperatures lower than RT. The results are described in Sec. 4.3.2.

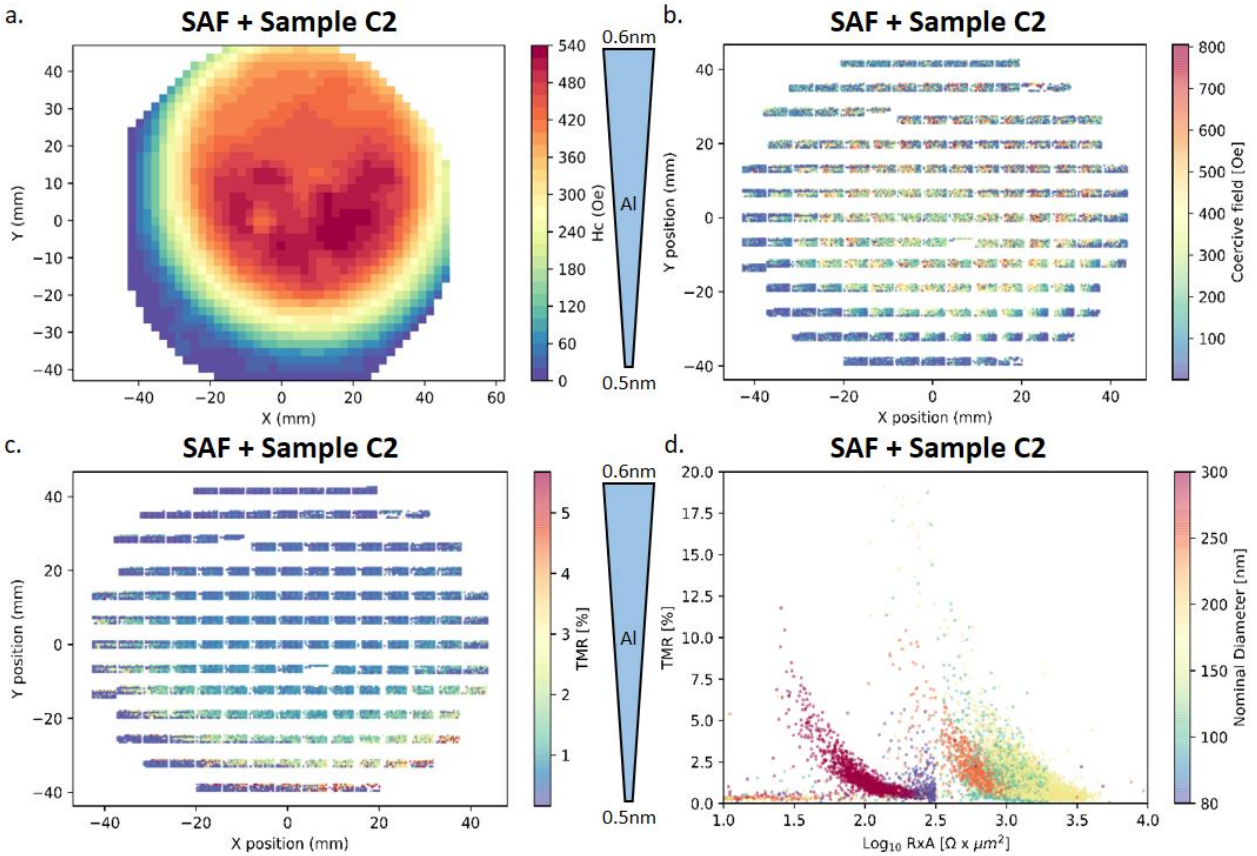

Fig. 4.6: Wafer yield and magnetic properties | **a.** Coercive field mapping at full sheet film level in NanoMOKE of a sample with a wedge along the y axis of Al from 0.5nm to 0.6nm. **b.** Coercive field mapping of the devices in the patterned wafer with a wedge along the y axis of Al from 0.5nm to 0.6nm as in a. **c.** TMR mapping of the devices in the patterned wafer with a wedge along the y axis of Al from 0.5nm to 0.6nm as in a. The color scale is adjusted for having a better visualisation of the TMR variation. **d.** TMR distribution of the devices in the patterned wafer with a wedge along the y axis of Al from 0.5nm to 0.6nmas in a. depending on their $R \times A$.

4.3.1 Devices with high Al content

In the central part of the wafer ($X = 0, Y = 0$), where the concentration of Al is higher, the magnetic hysteresis loops show very straight transitions (as in Fig. 4.7a). This can be a sign of the binary nature of the magnetic layer that, as evident from the TEM image in Fig. 4.4h, does not have a granular structure. To investigate such devices, we perform a temperature dependent measurements of the magnetic properties. As shown in Fig. 4.7b, the coercive field reaches the zero value around 370K. This is directly linked to the temperature dependence of the saturation magnetization [192] [193]. Also the TMR value, generally very low in this part of the wafer, has a similar trend due to the gradually decreasing magnetic anisotropy with temperature that affects the spin polarization [194] [195].

At this point, since no intermediate resistance states can be observed through the application of minor field loops (because of the straight magnetic transitions), the effect of STT is studied in order to find the switching regions and exploit the switching probability to partially switch the magnetization of the free layer. In order to do this, we performed phase diagram measurements that consist in the application of trains of pulses of different amplitudes (100ns duration at 1KHz), during the field amplitude sweeping (around 1Hz). In this way, we easily obtain the switching regions depending on field and voltage pulses. Two examples of phase diagrams are shown in Fig. 4.7c and d for two devices of respectively of 150nm (TMR around 9% and $R \times A$ around $350\Omega\mu m^2$) and 250nm of diameter (TMR around 12% and $R \times A$ around $300\Omega\mu m^2$). In both devices, the effect

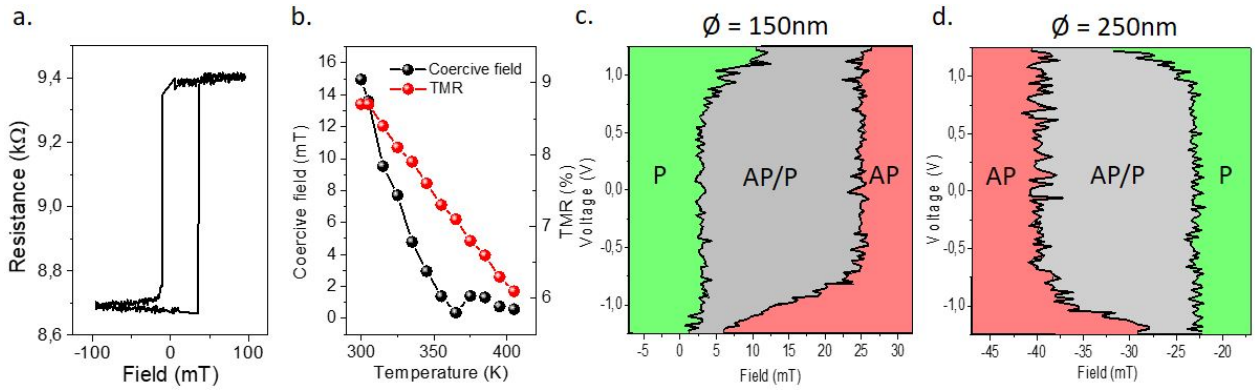

Fig. 4.7: High Al content device | **a.** Example of an hysteresis loop for a device with high Al content of 250nm of diameter, TMR around 8% and $R \times A$ around $440\Omega\mu m^2$. **b.** Coercive field and TMR dependence on temperature for a device with high Al content of 250nm of diameter, TMR around 13% and $R \times A$ around $300\Omega\mu m^2$.. **c.** Example of phase diagram for a device with high Al content of 150nm of diameter, TMR around 9% and $R \times A$ around $350\Omega\mu m^2$. **d.** Example of phase diagram for a device with high Al content of 250nm of diameter, TMR around 12% and $R \times A$ around $300\Omega\mu m^2$.

of the STT becomes evident at relatively high voltages ($\approx 1V$) in the asymmetric reduction of the coercive field (note that the maximum applied voltage $\approx 1.2V$ corresponds to the breakdown of the MgO barrier). Despite this, no other resistance values, different from the P and AP, are observed during the measurement. In order to confirm this binary behavior, trains of pulses with different pulse amplitudes and durations were applied to the device together with a field in order to find intermediate resistance states. In fact, the application of pulses with a switching probability lower than 100% would allow a partial switch of the magnetization. Unfortunately, also in this case, the resistance shows transitions only between the P and AP states. This, finally, confirms the binary nature of these devices.

4.3.2 Devices with low Al content

As previously stated, the granular structure created in the bottom part of the wafer is in a paramagnetic state probably due to the very small size of the grains (2nm - 3nm of diameter). For this reason the electrical characterizations of those devices were performed in a cryostat (able to reach temperatures down to 10K) and with a setup similar to the one already described in Sec. 2.4.1. Initially, the resistance trend with temperature, shown in Fig. 4.8a, was measured in order to check the good electrical functionalities of the setup (the measurement of too high resistances is problematic because of the presence of the bias tee). In a second step, we measured the magnetic properties variation with temperature in order to find the proper condition for the final memristive characterization. Ideally, this would be at a temperature low enough to ensure that each grain is no more paramagnetic (with a coercive field high enough) and with the highest possible remanence. However, a too low temperature would increase the thermal stability of the grains making them hardly switchable by STT. Therefore, a tradeoff on the measurement temperature has to be found.

The temperature dependences of coercive field and TMR are shown in Fig. 4.8b. As expected, the coercive field at very low temperatures reaches high values and goes to zero around 210K [192] [193]. Similarly, the TMR decreases with increasing temperature [195] but its average value remains rather low (generally from 5% to 15%). The ideal conditions for the current-induced measurements are found around 150K where the coercive field is generally between 25mT and 40mT (the temperature is set to this value for all the measurements shown in the following).

In order to prove the existence of intermediate resistance states, we perform a series of hysteresis loops under a field with varying amplitude. In fact, for this kind of devices, that at RT shows a paramagnetic behavior as in Fig. 4.8c, we expect, at low temperature, a tilted shape of the loop

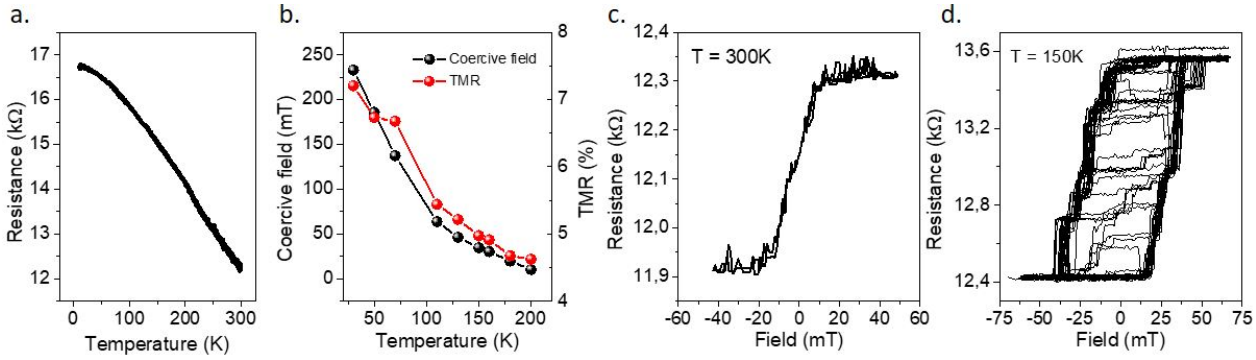

Fig. 4.8: Temperature dependence of magnetic properties | **a.** Resistance dependence on temperature for a device with low Al content of 250nm of diameter and TMR around 7%. **b.** Coercive field and TMR dependence on temperature for a device with low Al content. **c.** Example of hysteresis loop of a device with low Al content at RT. **d.** Example of hysteresis loop of a device with low Al content at 150K. The intermediate resistance values are obtained through minor field loops.

due to the anisotropy distribution caused by the different grain sizes. In this way, a series of minor loops with increasing amplitudes can gradually switch grains depending on their anisotropy, leading to intermediate resistance states. The result of this experiment is shown in Fig. 4.8d. The very high number of intermediate resistances at zero field demonstrates that an important number of magnetic configurations can be created in the sample. Considering the evident existence of multiple intermediate resistance states between the P and the AP ones, we studied the effect of the STT on these devices. We expect to obtain a statistical switching of the grains for different pulse parameters (duration and amplitude) due to the fact that the critical current for each grain depends on its anisotropy that, as previously stated, is linked to the size. Initially, to study the switching probability depending on the applied field and voltage, we perfomed a phase diagram similar to the one used for binary devices. Example of the resulting switching regions are shown in Fig. 4.9a and b for two devices of respectively 200nm (TMR around 8% and $R \times A$ around $300\Omega\mu m^2$) and 300nm (TMR around 11% and $R \times A$ around $270\Omega\mu m^2$) of diameter. Note that the colormap is simplified to have an easier understanding of the overall behavior. In fact, the high number of intermediate resistances is recreated with a very high number of colors and, therefore, does not allow an easy visualisation of the switching regions. In these diagrams the only transitions considered are taken at half of the total TMR. The actual magnetic transition, similarly to Fig. 4.8d, is gradual and undergoes a very high number of intermediate resistance states. As visible from the two figures, the STT effect starts to be evident for very high voltages ($> 1.3V$) and with the assistance of magnetic field. The critical voltage at zero field cannot be reached because of the breakdown voltage at 1.8V. Interestingly, while in Fig. 4.9a the effect of the increasing pulse length yields to a reduction of the switching voltage as expected from the STT, in Fig. 4.9b it increases the Joule heating effect, evident in the symmetric reduction of the coercivity. This is in agreement with the fact that the temperature reached because of Joule effect increases with the device diameter (see Eq. 3.19) [172].

At this point, the regions that show STT can be exploited for the final memristive behavior. In order to do this, a train of pulses with different parameters is applied to the device together with a field (according to the switching diagram). Despite several trials (pulse length, amplitude and frequency at different field amplitudes), the monotonicity of the resistance variation with the pulse polarity was hardly obtained. An example of this is shown in Fig. 4.9c for the device as in Fig. 4.9a. The pulses were applied at 1.5V and 50ns of duration together with an out-of-plane field of -10mT. While the average resistance tends to slowly decrease, the resistance variation occurring at the application of each pulse is not controllable. This can be due to the fact that the STT effect is weak due to the presence of FeCoAl at the interface with the MgO barrier (confirmed by the low TMR value) as in Fig. 4.5b . STT influence becomes visible only when a large number of current pulses is used as in the case of the phase diagram where around 1000 pulses are applied for each

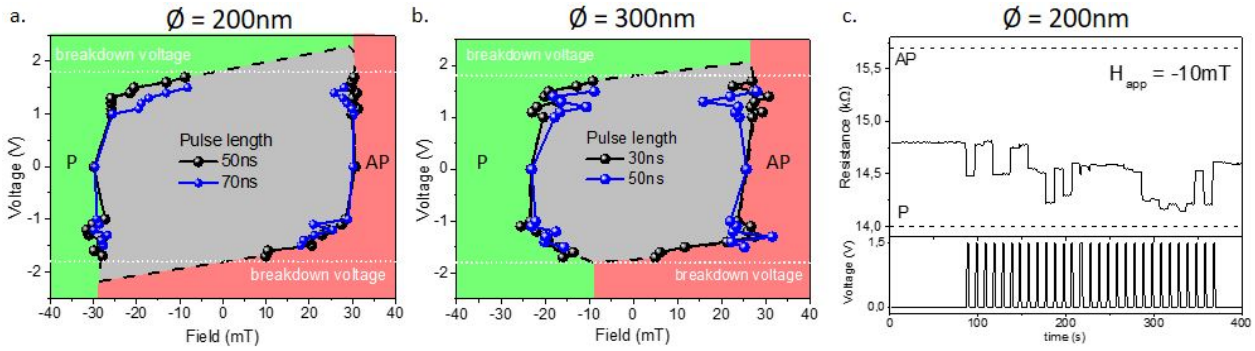

Fig. 4.9: Proof of STT at low temperature | **a.** Example of voltage - field diagram at 150K and different pulse lengths for a device with low Al content of 200nm of diameter, TMR around 8% and $R \times A$ around $300\Omega\mu m^2$. **b.** Example of voltage - field diagram at 150K and different pulse lengths for a device with low Al content of 300nm of diameter, TMR around 11% and $R \times A$ around $270\Omega\mu m^2$. In both diagrams the high number of intermediate resistance values is not taken into account in the colormap for simplicity. The transitions points are taken at half of the TMR value. **c.** Example of resistance variation to a train of pulses of 1.5V and 50ns duration, with an applied out-of-plane field of $H_{app} = -10mT$ for the device as in a.

point. Also, while the STT effect acts on the magnetization together with the field, a rearrangement of ions (as for example oxygen ions) can occur because of the high voltage applied across the high $R \times A$ device, probably due to the creation of hot spots. This can affect the resistance of the device in a complex way since the ion migration can increase/decrease the resistance (as for an OxRAM) and, at the same time, interact with the MgO barrier. Those measurements, up to now performed at 150K, were also repeated for other temperatures. At 120K, the thermal stability is higher and the critical voltage is increased so, finally, the STT effect is hardly observed. At 170K, despite the reduction of the thermal barrier, the Joule heating during the application of pulses becomes critical since the blocking temperature is around 200K. In this sense, the temperature set at 150K is a good trade off between those two phenomena. Also, we stated that devices with smaller dimensions (80nm or 100nm of diameter) present a number of intermediate states significantly lower probably due to the reduced number of grains.

Finally, we proved the existence of an STT effect, even if small. This does not allow a correct memristive behavior since the resistance variation is not controllable at the application of each pulse. The use of a layer with a better granularity should help to solve the problem and lead to a proper control of the resistance variation of the device.

We acknowledge Maxen Cosset-Cheneau and Laurent Vila for the help with this measurement.

4.4 Conclusions

In conclusion, the realization of such device with granular free layer relies on the possibility to create a magnetic medium made of FeCoB grains with a perpendicular anisotropy, surrounded by Al_2O_3 grain boundaries. The use of the oxide is supposed to optimize the STT efficiency since the full current would pass through the FeCo grains. The usual method for the deposition of a granular structure is the co-sputtering of two immiscible materials but, because of the absence of such tool in our lab, we exploited demixing of immiscible materials upon annealing starting from ultrathin multilayers. Also, the absence of an Al_2O_3 target in our sputtering tool was an additional challenge since the Al is supposed to be oxidized before being demixed (Al alone is miscible with FeCoB). To solve this, different oxidation conditions were investigated in order to explore the most efficient way to create Al_2O_3. It was found that, by oxidizing the ultrathin multilayer structure at the end of the deposition, the oxygen tends to migrate towards the Al instead of the FeCoB because of the very low enthalpy of formation of Al_2O_3. This mechanism is extremely sensitive to the Al content since a lack of Al yields the FeCoB oxidation, while an excess of Al yields the intermixing of Al with FeCoB creating an alloy and gradually degrading the magnetic properties. Once found the most efficient oxidation conditions, the ratio of materials for the formation of actual grain was investigated. We found that a granular structure can be created for $FeCoB_x/(Al_2O_3)_{1-x}$ at $x \approx 64\%$. The TEM images confirmed the creation of a polycrystalline magnetic medium in the region where the full quantity of Al is supposed to be oxidized. Unfortunately, the average grain size turns out to be around 2nm to 3nm of diameter leading to a paramagnetic state at RT.

A wafer with an Al wedge was deposited and patterned in nanopillars with sizes from 80nm to 300nm. The magnetic properties variations (such as the coercive field) at full sheet film were found to be not affected by the nanofabrication process. A series of electrical characterizations on the devices with high Al content indicated the existence of only two resistance states. In the thin part of the wedge, where all the Al is supposed to be oxidized, the field-driven measurements performed at 150K showed a quite high number of magnetic configurations possible in the granular structure. Moreover, current driven measurements showed that the STT effect slightly affects the magnetization of such free layer. However, despite the experimental evidence of STT effects in these devices, the resistance variation control is hardly achievable after a single pulse.

Finally, the complexity of the granular free layer does not allow a clear and overall understanding of the behavior of the device. Despite this, the important knowledge of the spintronic community on the granular media for magnetic recording, combined with the advances in the MRAM technology, should make this device an interesting candidate for a memristive device. However, further optimization would be necessary than was possible in the timeframe of this thesis and without the availability of a sputtering tool enabling cosputtering.

Chapter 5

Summary and perspectives

The purpose of this thesis was to propose new concepts of spintronic memristive devices in order to overcome the issues related with the size and the integrability of the existing ones. Here we describe two new devices that, thanks to their characteristics and working principles, are scalable and integrable at very large scale.

In the first device, shown in Chapter 3, the multi level resistances is achieved thanks to the cosinus variation of the conductance with the relative angle between the magnetizations of the storage layer and reference layer in an in-plane MTJ. A free layer whose magnetization can be stabilized independently on the in-plane direction and rotated by STT was developed. We modeled such layer with a macrospin code including an additional dissipative term in the LLG, analog to a dry friction term in the Newton's equation. With this model, we were able to reproduce the isotropic properties of the free layer and, thanks to the effect of an additional perpendicular polarizer, to discretely rotate the magnetization with current pulses properly designed and, finally, achieve the memristive behavior. Experimentally, we realized the isotropically coercive free layer with a FM/AF/FM structure where the thickness of the AF was chosen thin enough not to provide any exchange bias but rather enhanced coercivity. We were able to compare the experimental results and the model, finding good agreement. After some optimization steps, we integrated this composite free layer in a magnetic stack composed by substrate / buffer / perpendicularly magnetized SAF polarizer / bottom non-magnetic metallic spacer (Cu) / isotropically coercive free layer / MgO tunnel barrier / in-plane SAF analyzer. With field-driven experiments we checked that the isotropically coercive properties of the free layer are not affected significantly by the nano fabrication process used to create nano sized pillars. At device level, we obtained the expected memristive characteristics with voltage pulses of duration of the order of few ns. We demonstrated at least 21 intermediate resistance states. The main advantage of this device relies in the fact that its working principle are not directly related to its size (contrarily to the existing ones). This means that it can be scaled and, due to the similarities with a classic MRAM cell, it could be integrated at very large scale. The main drawback of this device is the presence of the thin AF layer in the free layer. In fact, despite its fundamental role in the formation of the isotropic properties, its relatively low blocking temperature does not allow a wide working temperature range and creates some complex dynamics due to the Joule heating occurring during the application of the pulses. In future, an accurate investigation of the temperature effects at full sheet film and at device level could lead to some improvements. Moreover, the study of an alternative way of achieving the isotropic properties could bring the device closer to a very large scale integration.

Towards this goal, in Chapter 4, we introduced the idea of an MTJ whose free layer presents a granular structure similar to the one developed for decades for magnetic recording media. The memristive behavior could be obtained from the probabilistic switching of grains with properly designed current pulses through STT (or even SOT). We encountered several problems in the creation of such granular layer mostly linked to the non-availability in our lab of a deposition tool enabling co-sputtering of materials. Despite this, we created such layer through a complex combination of very thin multilayer deposition and oxidation steps. The small nature of the grains,

paramagnetic at RT, led us to perform experiments at lower temperature. Here we achieved a very high number of intermediate resistance states in field-driven experiments and we observed STT effects. Despite this, the complexity of the material development did not allow a complete understanding of the resistance variation observed. Generally, this problems are easily solvable with the use of a proper co-sputtering machine. Moreover, the industrial expertise acquired for the realization of granular structures for recording media, could be used, in this sense, to obtain the wanted magnetic properties. Also, considering the industrialization level of both recording media and STT-MRAM, a large scale integration of such device should be achievable. Even the simple working principle could bring the advantage of an easy programmable interface for the control of the device. The main disadvantage is that the scalability of the device is relatively limited. In fact, similarly to the spintronic memristors based on DW, the size of the device cannot be reduced to extremely small values (sub-20nm) since a minimum number of grains is required for a good statistic during the probabilistic switching. Despite this, the device remains much more compact than the ferroelectric, DW pinning and AF/FM based devices.

Finally, the integration of such devices in a relatively simple architecture could demonstrate the potentialities of these memristive devices at very large scale and with a density integration higher than with analog CMOS.

Appendix

Contents

This appendix provides the detailed steps to calculate the critical fields and current densities presented in chapter 3.

A.1 Static equilibrium under in-plane field

Considering an in-plane applied field, the expression of the LLG equation modified by an additional dissipative term

$$\frac{\partial \vec{m}}{\partial t} = -\gamma(\vec{m} \times \mu_0 \vec{H_{eff}}) + \alpha_G(\vec{m} \times \frac{\partial \vec{m}}{\partial t}) + \beta \frac{\vec{m} \times \frac{\partial \vec{m}}{\partial t}}{|\vec{m} \times \frac{\partial \vec{m}}{\partial t}|} \tag{A.1}$$

includes an effective field given by

$$\vec{H_{eff}} = \vec{H_{app}} + \vec{H_{dem}} = [H_{app}cos(\varphi_H) \quad H_{app}sin(\varphi_H) \quad -M_S cos(\theta_M)] \tag{A.2}$$

where $\theta_{M,H}$ and $\varphi_{M,H}$ are, respectively, the polar angle and the azimuthal angle of the magnetization (M) and the external field (H). Considering the magnetization $\vec{m} = [m_x \quad m_y \quad m_z]$, the equilibrium condition, given by the expression

$$|\gamma(\vec{m}\times)\mu_0 \vec{H_{eff}}| < \beta \tag{A.3}$$

becomes

$$\gamma\mu_0 \begin{vmatrix} -m_y M_S cos(\theta_M) - m_z H_{app} sin(\varphi_H) \\ m_z H_{app} cos(\varphi_H) + m_x M_S cos(\theta_M) \\ m_x H_{app} sin(\varphi_H) - m_y H_{app} sin(\varphi_H) \end{vmatrix} < \beta \tag{A.4}$$

Considering in-plane solutions ($m_z = 0$ and $cos(\theta_M) = 0$) we obtain

$$\gamma\mu_0 \begin{vmatrix} 0 \\ 0 \\ m_x H_{app} sin(\varphi_H) - m_y H_{app} sin(\varphi_H) \end{vmatrix} < \beta \tag{A.5}$$

Using the spherical coordinates, we have $\vec{m} = [cos(\varphi_M) \quad sin(\varphi_M) \quad 0]$ and the equilibrium contition becomes

$$|cos(\varphi_M)sin(\varphi_H) - sin(\varphi_M)sin(\varphi_H)| < \frac{\beta}{\gamma\mu_0 H_{app}} \tag{A.6}$$

$$|sin(\varphi_H - \varphi_M)| = |sin(\phi)| < \frac{\beta}{\gamma\mu_0 H_{app}}. \tag{A.7}$$

Since $|sin(\varphi_H - \varphi_M)| \leq 1$ we obtain

$$\frac{\beta}{\gamma\mu_0 H_{app}} \leq 1 \tag{A.8}$$

$$\mu_0 H_{th} \leq \frac{\beta}{\gamma} \tag{A.9}$$

A.2 Magnetization dynamics under in-plane rotating field

Considering an in-plane rotating field, the effective field can be written as

$$\vec{H_{eff}} = \vec{H_{rot}} + \vec{H_{dem}} = [H_{rot}cos(\omega_{rot}t + \varphi_{rot}) \quad H_{rot}sin(\omega_{rot}t + \varphi_{rot}) \quad -M_S cos(\theta_M)] \tag{A.10}$$

where ω_{rot} and φ_{rot} are, respectively, the angular velocity of the rotating field and its initial angle. Considering the magnetization

$$\vec{m} = [sin(\theta_M)cos(\omega_M t + \varphi_M) \quad sin(\theta_M)sin(\omega_M t + \varphi_M) \quad cos(\theta_M)] \tag{A.11}$$

To solve the LLG we first compute

$$\frac{\partial \vec{m}}{\partial t} = \begin{pmatrix} -\omega_M sin(\theta_M) sin(\omega_M t + \varphi_M) \\ \omega_M sin(\theta_M) cos(\omega_M t + \varphi_M) \\ 0 \end{pmatrix} \tag{A.12}$$

$$\vec{m} \times \frac{\partial \vec{m}}{\partial t} = \begin{pmatrix} -\omega_M sin(\theta_M) cos(\theta_M) cos(\omega_M t + \varphi_M) \\ -\omega_M sin(\theta_M) cos(\theta_M) sin(\omega_M t + \varphi_M) \\ \omega_M sin(\theta_M)^2 \end{pmatrix} \tag{A.13}$$

and

$$\vec{m} \times \vec{H_{eff}} \begin{vmatrix} -M_S cos(\theta_M) sin(\theta_M) sin(\omega_M t + \varphi_M) - H_{rot} cos(\theta_M) sin(\omega_{rot} t + \varphi_{rot}) \\ H_{rot} cos(\theta_M) cos(\omega_{rot} t + \varphi_{rot}) + M_S cos(\theta_M) sin(\theta_M) cos(\omega_M t + \varphi_M) \\ H_{rot} sin(\theta_M) sin(((\omega_{rot} - \omega_M)t) + \varphi_{rot} - \varphi_M) \end{vmatrix} \tag{A.14}$$

Considering the third component equation

$$0 = -\gamma \mu_0 H_{rot} sin(((\omega_{rot} - \omega_M)t) + \varphi_{rot} - \varphi_M) + a\omega_M sin(\theta_M)^2 \tag{A.15}$$

we can assume in-plane ($cos(\theta_M) = 0$) and stationary solutions ($\omega_{rot} = \omega_M = \omega$) and we obtain

$$sin(\varphi_{rot} - \varphi_M) = sin(\phi) = a\frac{\omega}{\gamma \mu_0 H_{rot}} = \frac{\alpha_G \omega}{\gamma \mu_0 H_{rot}} + \frac{\beta}{\gamma \mu_0 H_{rot}} \tag{A.16}$$

where we remember that $a = \alpha_G + \beta/|\frac{\partial m}{\partial t}| = \alpha_G + \beta/|\omega sin(\theta_M)|$ Since $sin(\phi) \leq 1$ we have that the threshold field for the rotating case is

$$\mu_0 H_{throt} \leq \frac{\beta}{\gamma} + \frac{\alpha_G \omega}{\gamma} \tag{A.17}$$

A.3 Perpendicular polarizer STT-driven dynamics under dc current

Considering the STT coming from the out-of-plane polarizer, it is possible to include in the H_{eff} the following term $H_{stt} = C\vec{m} \times \vec{p}$ where $\vec{p} = [0 \quad 0 \quad 1]$ and $C = (a_{||perp}/\mu_0)V$, here $a_{||perp} = \hbar/(2e)[\eta_{perp}/(lM_S R \times A)]$ where η_{perp} is the spin polarization, l is the layer thickness, V is the voltage across the tunnel barrier separating the perpendicular polarizer and the free layer, and $R \times A$ is the resistance-area product. Considering

$$\vec{m} = [sin(\theta_M) cos(\omega_M t + \varphi_M) \quad sin(\theta_M) sin(\omega_M t + \varphi_M) \quad cos(\theta_M)] \tag{A.18}$$

the effective field becomes

$$\vec{H_{eff}} = \vec{H_{stt}} + \vec{H_{dem}} = \begin{pmatrix} C sin(\theta_M) sin(\omega_M t + \varphi_M) \\ -C sin(\theta_M) cos(\omega_M t + \varphi_M) \\ -M_S cos(\theta_M) \end{pmatrix} \tag{A.19}$$

Looking for stationary solutions (with constant out-of-plane angle $cos(\theta_M) = constant$) it can be obtained

$$\frac{\partial \vec{m}}{\partial t} = \begin{pmatrix} -\omega_M sin(\theta_M) sin(\omega_M t + \varphi_M) \\ \omega_M sin(\theta_M) cos(\omega_M t + \varphi_M) \\ 0 \end{pmatrix} \tag{A.20}$$

$$\vec{m} \times \vec{H_{eff}} = \begin{pmatrix} -M_S sin(\theta_M)cos(\theta_M)sin(\omega_M t + \varphi_M) + Csin(\theta_M)cos(\theta_M)cos(\omega_M t + \varphi_M) \\ Csin(\theta_M)cos(\theta_M)sin(\omega_M t + \varphi_M) + M_S sin(\theta_M)cos(\theta_M)cos(\omega_M t + \varphi_M) \\ -Csin(\theta_M)^2 \end{pmatrix} \quad (A.21)$$

$$\vec{m} \times \frac{\partial \vec{m}}{\partial t} = \begin{pmatrix} -\omega_M sin(\theta_M)cos(\theta_M)cos(\omega_M t + \varphi_M) \\ -\omega_M sin(\theta_M)cos(\theta_M)sin(\omega_M t + \varphi_M)) \\ \omega sin(\theta_M)^2 \end{pmatrix} \quad (A.22)$$

The third component LLG equation is then

$$0 = \gamma\mu_0 Csin(\theta_M)^2 + a\omega_M sin(\theta_M)^2 \quad (A.23)$$

from which we can obtain

$$0 = \gamma\mu_0 C + a\omega_M = \gamma\mu_0 C + (\alpha_G + \frac{\beta}{|\omega_M sin(\theta)|})\omega_M \quad (A.24)$$

and finally

$$\omega_M = -\frac{\gamma\mu_0 C}{\alpha_G} - \frac{\beta}{\alpha_G sin(\theta_M)}\frac{\omega_M}{|\omega_M|} \quad (A.25)$$

A.4 In-plane field-dc current diagram with perpendicular polarizer

Considering the STT coming from the perpendicular polarizer and an in-plane field perpendicular to the direction of the analyzer magnetization (in this case the field is along the y axis) $\vec{H_{app}} = [0 \quad H_{app} \quad 0]$, it is possible to include in the H_{eff} the following term $H_{stt} = C\vec{m} \times \vec{p}$ where $\vec{p} = [0 \quad 0 \quad 1]$ and $C = (a_{||perp}/\mu_0)V$, here $a_{||perp} = \hbar/(2e)[\eta_{perp}/(lM_S R \times A)]$ where η_{perp} is the spin polarization, l is the layer thickness, V is the voltage across the tunnel barrier separating the perpendicular polarizer and the free layer, and $R \times A$ is the resistance-area product. The effective field becomes

$$\vec{H_{eff}} = \vec{H_{stt}} + \vec{H_{dem}} + \vec{H_{app}} = \begin{pmatrix} Cm_y \\ -Cm_x + H_{app} \\ -M_S m_z \end{pmatrix} \quad (A.26)$$

Considering the equilibrium condition, given by the expression

$$|\gamma(\vec{m}\times)\mu_0 \vec{H_{eff}}| < \beta \quad (A.27)$$

becomes for in-plane solutions ($m_z = 0$)

$$\gamma\mu_0 \begin{vmatrix} 0 \\ 0 \\ -Cm_x^2 - Cm_x^2 + H_{app}m_x \end{vmatrix} = \gamma\mu_0 \begin{vmatrix} 0 \\ 0 \\ -C + H_{app}m_x \end{vmatrix} < \beta \quad (A.28)$$

This becomes

$$|\gamma\mu_0 H_{app} m_x - \gamma a_{||perp} V| < \beta \quad (A.29)$$

Since, in this case, $m_x = sin\phi$, we can obtain

$$-\frac{\beta}{\gamma\mu_0} + \frac{a_{||perp}V}{\mu_0 H_{app}} < sin\phi < \frac{\beta}{\gamma\mu_0} + \frac{a_{||perp}V}{\mu_0 H_{app}} \quad (A.30)$$

Since $sin\phi \leq 1$ we obtain the threshold

$$J_{th} = V_{th}/R \times A = \frac{\mu_0 H_{app} 2elM_S}{\hbar\eta_{perp}} - \frac{\beta 2elM_S}{\hbar\eta_{perp}\gamma} \quad (A.31)$$

A.5 In-plane analyzer STT-driven dynamics under dc current

Considering the STT coming from the in-plane analyzer, it is possible to include in the H_{eff} the following term $H_{stt} = C\vec{m}\times\vec{l}$ where $\vec{l} = [1 \quad 0 \quad 0]$ and $C = (a_{||}/\mu_0)V$, here $a_{||an} = \hbar/(2e)[\eta_{an}/(lM_SR\times A)]$ where η_{an} is the spin polarization, l is the layer thickness, V is the voltage across the tunnel barrier separating the perpendicular polarizer and the free layer, and $R \times A$ is the resistance-area product. The effective field becomes

$$\vec{H_{eff}} = \vec{H_{stt}} + \vec{H_{dem}} = [0 \quad Cm_z \quad -Cm_y - M_Sm_z] \tag{A.32}$$

Considering the equilibrium condition, given by the expression

$$|\gamma(\vec{m}\times)\mu_0\vec{H_{eff}}| < \beta \tag{A.33}$$

becomes for in-plane solutions ($m_z = 0$)

$$\gamma\mu_0 \begin{vmatrix} -Cm_y^2 \\ Cm_xm_y \\ 0 \end{vmatrix} < \beta \tag{A.34}$$

Considering in-plane solutions ($m_z = 0$ and $cos(\theta_M) = 0$) we obtain

$$\gamma\mu_0 \begin{vmatrix} 0 \\ 0 \\ m_xH_{app}sin(\varphi_H) - m_yH_{app}sin(\varphi_H) \end{vmatrix} = |\gamma\mu_0 Cm_y| < \beta \tag{A.35}$$

This can be written as

$$-\frac{\beta 2elM_SR\times A}{\gamma V\eta_{an}\hbar} < m_y < \frac{\beta 2elM_SR\times A}{\gamma V\eta_{an}\hbar} \tag{A.36}$$

and since $m_y \leq 1$ we have that

$$J_{an} = V/R\times A = \frac{\beta M_Sl2e}{\gamma\hbar\eta_{an}}. \tag{A.37}$$

A.6 In-plane analyzer and perpendicular polarizer STT-driven dynamics under dc current

Considering the STT coming from the in-plane analyzer and perpendicular polarizer, it is possible to include in the H_{eff} the following term $H_{stt} = C_{perp}\vec{m}\times\vec{p} - C_{an}\vec{m}\times\vec{l}$ where $\vec{l} = [0 \quad 0 \quad 1]$, $\vec{l} = [1 \quad 0 \quad 0]$ and $C_{perp(an)} = (a_{||perp(an)}/\mu_0)V$, here $a_{||perp(an)} = \hbar/(2e)[\eta_{perp(an)}/(lM_SR\times A)]$ where $\eta_{perp(an)}$ is the spin polarization, l is the layer thickness, V is the voltage across the tunnel barrier separating the perpendicular polarizer and the free layer, and $R \times A$ is the resistance-area product. Note that the minus sign takes into account that the electron flux passes through polarizer, free layer and analyzer (meaning that the two STT terms are opposite in sign) or vicecersa.

$$H_{stt} = C_{perp}\vec{m}\times\vec{p} - C_{an}\vec{m}\times\vec{l} = \begin{vmatrix} C_{perp}m_y \\ -C_{an}m_z - Cperpm_x \\ C_{an}m_y \end{vmatrix} \tag{A.38}$$

from this

$$\vec{H_{eff}} = \vec{H_{stt}} + \vec{H_{dem}} = \begin{vmatrix} C_{perp}m_y \\ -C_{an}m_z - C_{perp}m_x \\ C_{an}m_y - M_Sm_z \end{vmatrix} \tag{A.39}$$

Considering the equilibrium condition, given by the expression

$$|\gamma(\vec{m}\times)\mu_0\vec{H_{eff}}| < \beta \tag{A.40}$$

becomes for in-plane solutions ($m_z = 0$)

$$C_{an}^2 m_y^2 + C_{an}^2 m_x^2 m_y^2 + C_{perp}^2 < \beta^2/(\gamma^2\mu_0^2) \tag{A.41}$$

$$C_{an}^2 m_y^2 + C_{perp}^2 < \beta^2/(\gamma^2\mu_0^2) \tag{A.42}$$

$$m_y^2 < \frac{\beta^2}{\gamma^2\mu_0^2 Can^2} - \frac{C_{perp}^2}{C_{an}^2} \tag{A.43}$$

Since $m_y^2 \leq 1$, we can write

$$\frac{\beta^2}{\gamma^2\mu_0^2 C_{an}^2} - \frac{C_{perp}^2}{C_{an}^2} \leq 1 \tag{A.44}$$

$$\beta^2 - \gamma^2\mu_0^2(C_{perp}^2 + C_{an}^2 \leq 0 \tag{A.45}$$

$$\beta^2 - \gamma^2\frac{\hbar^2}{4e^2l^2M_S^2}J^2(\eta_{perp}^2 + \eta_{an}^2 \leq 0 \tag{A.46}$$

From this

$$J_{double} = \frac{\beta 2elM_S}{\gamma\hbar}\frac{1}{\sqrt{\eta_{perp}^2 + \eta_{an}^2}} \tag{A.47}$$

References

[1] Moore G. *Cramming More Components Onto Integrated Circuits.* Proceedings of the IEEE **86**, 82–85 (1998). [p. 1]

[2] *DataAge 2025 - La numérisation du monde — Seagate France.* [p. 1]

[3] Reinsel D., Gantz J. & Rydning J. *The Digitization of the World from Edge to Core* 28 (2018). [p. 1]

[4] *AlphaGo: Mastering the ancient game of Go with Machine Learning.* [p. 1]

[5] Silver D., Huang A., Maddison C. J., Guez A., Sifre L., van den Driessche G., Schrittwieser J., Antonoglou I., Panneershelvam V., Lanctot M., Dieleman S., Grewe D., Nham J., Kalchbrenner N., Sutskever I., Lillicrap T., Leach M., Kavukcuoglu K., Graepel T. & Hassabis D. *Mastering the game of Go with deep neural networks and tree search.* Nature **529**, 484–489 (2016). [p. 1]

[6] *Big data needs a hardware revolution.* Nature **554**, 145–146 (2018). [p. 2]

[7] Thompson N. C., Greenewald K., Lee K. & Manso G. F. *The Computational Limits of Deep Learning.* arXiv:2007.05558 [cs, stat] (2020). [p. 2]

[8] Furber S. B., Galluppi F., Temple S. & Plana L. A. *The SpiNNaker Project.* Proceedings of the IEEE **102**, 652–665 (2014). [p. 2]

[9] Merolla P. A., Arthur J. V., Alvarez-Icaza R., Cassidy A. S., Sawada J., Akopyan F., Jackson B. L., Imam N., Guo C., Nakamura Y., Brezzo B., Vo I., Esser S. K., Appuswamy R., Taba B., Amir A., Flickner M. D., Risk W. P., Manohar R. & Modha D. S. *A million spiking-neuron integrated circuit with a scalable communication network and interface.* Science **345**, 668–673 (2014). [p. 2]

[10] Indiveri G. & Liu S.-C. *Memory and information processing in neuromorphic systems.* Proceedings of the IEEE **103**, 1379–1397 (2015). [p. 2]

[11] Sze V., Chen Y.-H., Emer J., Suleiman A. & Zhang Z. *Hardware for machine learning: Challenges and opportunities.* In *2018 IEEE Custom Integrated Circuits Conference (CICC)*, 1–8 (2018). [p. 2]

[12] Xia Q., Berggren K. K., Likharev K., Strukov D. B., Jiang H., Mikolajick T., Querlioz D., Salinga M., Erickson J., Pi S., Xiong F., Lin P., Li C., Xiong S., Hoskins B., Daniels M., Madhavan A., Liddle J., McClelland J., Yang Y., Rupp J., Nonnenmann S., Gong N., Cheng K.-T. T., Montaño M. A. L., Talin A. A., Salleo A., Shastri B. J., de Lima T. F., Tait A. N., Shen Y., Meng H., Roques-Carmes C., Cheng Z., Bhaskaran H., Jariwala D., Wang H., Segall K., Shainline J., Yang J. J., Roy K., Datta S. & Raychowdhury A. *Roadmap on emerging hardware and technology for machine learning.* Nanotechnology (2020). [p. 2]

[13] Chua L. *Memristor-The missing circuit element.* IEEE Transactions on Circuit Theory **18**, 507–519 (1971). [pp. 3, 45, 50]

[14] Chua L. O. & Sung Mo Kang. *Memristive devices and systems.* Proceedings of the IEEE **64**, 209–223 (1976). [pp. 3, 45, 50]

[15] Ishimaru K. *Future of Non-Volatile Memory -From Storage to Computing-* 6 . [p. 3]

[16] Li Y., Wang Z., Midya R., Xia Q. & Yang J. J. *Review of memristor devices in neuromorphic computing: Materials sciences and device challenges.* Journal of Physics D: Applied Physics **51**, 503002 (2018). [pp. 3, 20]

[17] Grollier J., Querlioz D. & Stiles M. D. *Spintronic Nanodevices for Bioinspired Computing.* Proceedings of the IEEE **104**, 2024–2039 (2016). [p. 3]

[18] Locatelli N., Vincent A. F., Mizrahi A., Friedman J. S., Vodenicarevic D., Kim J., Klein J., Zhao W., Grollier J. & Querlioz D. *Spintronic devices as key elements for energy-efficient neuroinspired architectures.* In *2015 Design, Automation Test in Europe Conference Exhibition (DATE)*, 994–999 (2015). [pp. 3, 20]

[19] Étienne Du Trémolet de Lacheisserie. *Magnétisme (Tome I) - Étienne Du Trémolet de Lacheisserie - EDP Sciences* (EDP Sciences, 2012). [p. 6]

[20] Gilbert W. *On the Loadstone and Magnetic Bodies and on the Great Magnet the Earth* (1600). [p. 6]

[21] Oersted H. C. *Experiments on the Effect of a Current of Electricity on the Magnetic Needle. vol. 16, p. 273-277* (1820). [p. 6]

[22] Maxwell J. C. *A Treatise on Electricity and Magnetism* (1873). [p. 6]

[23] Weiss P. *L'hypothèse du champ moléculaire et la propriété ferromagnétique.* Journal de Physique Théorique et Appliquée **6**, 661–690 (1907). [pp. 6, 7]

[24] Stoner E. C. *Collective electron ferronmagnetism.* Proceedings of the Royal Society of London. Series A. Mathematical and Physical Sciences **165**, 372–414 (1938). [p. 6]

[25] Stoner E. C. *Collective electron ferromagnetism II. Energy and specific heat.* Proceedings of the Royal Society of London. Series A. Mathematical and Physical Sciences **169**, 339–371 (1939). [p. 6]

[26] Slater J. C. *Electronic Structure of Alloys.* Journal of Applied Physics **8**, 385 (2004). [p. 6]

[27] Coey J. M. D. *Materials for Spin Electronics.* In Ziese M. & Thornton M. J. (eds.) *Spin Electronics*, 277–297 (Springer, Berlin, Heidelberg, 2001). [p. 7]

[28] Brown W. F. *Criterion for Uniform Micromagnetization.* Physical Review **105**, 1479–1482 (1957). [p. 7]

[29] Heisenberg W. *Mehrkörperproblem und Resonanz in der Quantenmechanik.* Zeitschrift für Physik **38**, 411–426 (1926). [p. 7]

[30] Aharoni A. *Demagnetizing factors for rectangular ferromagnetic prisms.* Journal of Applied Physics **83**, 3432–3434 (1998). [p. 8]

[31] Shuddemagen C. L. B. *The Demagnetizing Factors for Cylindrical Iron Rods.* Proceedings of the American Academy of Arts and Sciences **43**, 185 (1907). [p. 8]

[32] Néel L. *Anisotropie magnétique superficielle et surstructures d'orientation.* J. Phys. Radium **15**, 225–239 (1954). [p. 9]

[33] Engel B. N., England C. D., Van Leeuwen R. A., Wiedmann M. H. & Falco C. M. *Interface magnetic anisotropy in epitaxial superlattices.* Physical Review Letters **67**, 1910–1913 (1991). [p. 9]

[34] Johnson M. T., Bloemen P. J. H., den Broeder F. J. A. & de Vries J. J. *Magnetic anisotropy in metallic multilayers.* Reports on Progress in Physics **59**, 1409–1458 (1996). [p. 9]

[35] Nakajima N., Koide T., Shidara T., Miyauchi H., Fukutani H., Fujimori A., Iio K., Katayama T., Nývlt M. & Suzuki Y. *Perpendicular Magnetic Anisotropy Caused by Interfacial Hybridization via Enhanced Orbital Moment in Co/Pt Multilayers: Magnetic Circular X-Ray Dichroism Study.* Physical Review Letters **81**, 5229–5232 (1998). [p. 9]

[36] Zeper W. B., Greidanus F. J. A. M., Carcia P. F. & Fincher C. R. *Perpendicular magnetic anisotropy and magneto-optical Kerr effect of vapor-deposited Co/Pt-layered structures.* Journal of Applied Physics **65**, 4971–4975 (1989). [p. 9]

[37] den Broeder F. J. A., Kuiper D., van de Mosselaer A. P. & Hoving W. *Perpendicular Magnetic Anisotropy of Co-Au Multilayers Induced by Interface Sharpening.* Physical Review Letters **60**, 2769–2772 (1988). [p. 9]

[38] Yang H. X., Chshiev M., Dieny B., Lee J. H., Manchon A. & Shin K. H. *First-principles investigation of the very large perpendicular magnetic anisotropy at Fe/MgO and Co/MgO interfaces.* Physical Review B **84**, 054401 (2011). [p. 9]

[39] Dieny B. & Chshiev M. *Perpendicular magnetic anisotropy at transition metal/oxide interfaces and applications.* Reviews of Modern Physics **89**, 025008 (2017). [p. 9]

[40] Mott N. F. & Fowler R. H. *The electrical conductivity of transition metals.* Proceedings of the Royal Society of London. Series A - Mathematical and Physical Sciences **153**, 699–717 (1936). [p. 9]

[41] Sommerfeld A. *Zur Elektronentheorie der Metalle auf Grund der Fermischen Statistik.* Zeitschrift für Physik **47**, 1–32 (1928). [p. 9]

[42] Fert A. & Campbell I. A. *Two-Current Conduction in Nickel.* Physical Review Letters **21**, 1190–1192 (1968). [p. 10]

[43] Fert A. & Campbell I. *Transport properties of ferromagnetic transition metals.* Journal de Physique Colloques **32**, C1–46–C1–50 (1971). [p. 10]

[44] Fert A. & Campbell I. A. *Electrical resistivity of ferromagnetic nickel and iron based alloys.* Journal of Physics F: Metal Physics **6**, 849–871 (1976). [p. 10]

[45] Thomson W. *XIX. On the electro-dynamic qualities of metals:—Effects of magnetization on the electric conductivity of nickel and of iron.* Proceedings of the Royal Society of London **8**, 546–550 (1857). [p. 10]

[46] McGuire T. & Potter R. *Anisotropic magnetoresistance in ferromagnetic 3d alloys.* IEEE Transactions on Magnetics **11**, 1018–1038 (1975). [pp. 10, 30, 52]

[47] Ramirez A. P. *Colossal magnetoresistance.* Journal of Physics: Condensed Matter **9**, 8171–8199 (1997). [p. 10]

[48] *Enhanced Room-Temperature Geometric Magnetoresistance in Inhomogeneous Narrow-Gap Semiconductors — Science.* [p. 10]

[49] Baibich M. N., Broto J. M., Fert A., Van Dau F. N., Petroff F., Etienne P., Creuzet G., Friederich A. & Chazelas J. *Giant Magnetoresistance of (001)Fe/(001)Cr Magnetic Superlattices.* Physical Review Letters **61**, 2472–2475 (1988). [p. 10]

[50] Binasch G., Grünberg P., Saurenbach F. & Zinn W. *Enhanced magnetoresistance in layered magnetic structures with antiferromagnetic interlayer exchange.* Physical Review B **39**, 4828–4830 (1989). [p. 10]

[51] Parkin S. S. P., More N. & Roche K. P. *Oscillations in exchange coupling and magnetoresistance in metallic superlattice structures: Co/Ru, Co/Cr, and Fe/Cr.* Physical Review Letters **64**, 2304–2307 (1990). [p. 11]

[52] Camley R. E. & Barnaś J. *Theory of giant magnetoresistance effects in magnetic layered structures with antiferromagnetic coupling.* Physical Review Letters **63**, 664–667 (1989). [p. 12]

[53] Barnaś J., Fuss A., Camley R. E., Grünberg P. & Zinn W. *Novel magnetoresistance effect in layered magnetic structures: Theory and experiment.* Physical Review B **42**, 8110–8120 (1990). [p. 12]

[54] Levy P. M., Zhang S. & Fert A. *Electrical conductivity of magnetic multilayered structures.* Physical Review Letters **65**, 1643–1646 (1990). [p. 12]

[55] Dieny B., Humbert P., Speriosu V. S., Metin S., Gurney B. A., Baumgart P. & Lefakis H. *Giant magnetoresistance of magnetically soft sandwiches: Dependence on temperature and on layer thicknesses.* Physical Review B **45**, 806–813 (1992). [p. 12]

[56] Dieny B., Speriosu V. S., Parkin S. S. P., Gurney B. A., Wilhoit D. R. & Mauri D. *Giant magnetoresistive in soft ferromagnetic multilayers.* Physical Review B **43**, 1297–1300 (1991). [p. 12]

[57] Julliere M. *Tunneling between ferromagnetic films.* Physics Letters A **54**, 225–226 (1975). [p. 12]

[58] Miyazaki T. & Tezuka N. *Giant magnetic tunneling effect in Fe/Al2O3/Fe junction.* Journal of Magnetism and Magnetic Materials **139**, L231–L234 (1995). [p. 12]

[59] Moodera J. S., Kinder L. R., Wong T. M. & Meservey R. *Large Magnetoresistance at Room Temperature in Ferromagnetic Thin Film Tunnel Junctions.* Physical Review Letters **74**, 3273–3276 (1995). [p. 12]

[60] Tsunoda M., Nishikawa K., Ogata S. & Takahashi M. *60% magnetoresistance at room temperature in Co–Fe/Al–O/Co–Fe tunnel junctions oxidized with Kr–O2 plasma.* Applied Physics Letters **80**, 3135–3137 (2002). [p. 13]

[61] Wang D., Nordman C., Daughton J., Qian Z. & Fink J. *70% TMR at room temperature for SDT sandwich junctions with CoFeB as free and reference Layers.* IEEE Transactions on Magnetics **40**, 2269–2271 (2004). [p. 13]

[62] Sousa R. C., Sun J. J., Soares V., Freitas P. P., Kling A., da Silva M. F. & Soares J. C. *Large tunneling magnetoresistance enhancement by thermal anneal.* Applied Physics Letters **73**, 3288–3290 (1998). [p. 13]

[63] Teresa J. M. D., Barthélémy A., Fert A., Contour J. P., Montaigne F. & Seneor P. *Role of Metal-Oxide Interface in Determining the Spin Polarization of Magnetic Tunnel Junctions.* Science **286**, 507–509 (1999). [p. 13]

[64] Bowen M., Bibes M., Barthélémy A., Contour J.-P., Anane A., Lemaitre Y. & Fert A. *Nearly total spin polarization in La2/3Sr1/3MnO3 from tunneling experiments.* Applied Physics Letters **82**, 233–235 (2003). [p. 13]

[65] Faure-Vincent J., Tiusan C., Jouguelet E., Canet F., Sajieddine M., Bellouard C., Popova E., Hehn M., Montaigne F. & Schuhl A. *High tunnel magnetoresistance in epitaxial Fe/MgO/Fe tunnel junctions.* Applied Physics Letters **82**, 4507–4509 (2003). [p. 13]

[66] Parkin S. S. P., Kaiser C., Panchula A., Rice P. M., Hughes B., Samant M. & Yang S.-H. *Giant tunnelling magnetoresistance at room temperature with MgO (100) tunnel barriers.* Nature Materials **3**, 862–867 (2004). [p. 13]

[67] Djayaprawira D. D., Tsunekawa K., Nagai M., Maehara H., Yamagata S., Watanabe N., Yuasa S., Suzuki Y. & Ando K. *230% room-temperature magnetoresistance in CoFeB/MgO/CoFeB magnetic tunnel junctions.* Applied Physics Letters **86**, 092502 (2005). [p. 13]

[68] Ikeda S., Hayakawa J., Ashizawa Y., Lee Y. M., Miura K., Hasegawa H., Tsunoda M., Matsukura F. & Ohno H. *Tunnel magnetoresistance of 604% at 300K by suppression of Ta diffusion in CoFeB/MgO/CoFeB pseudo-spin-valves annealed at high temperature.* Applied Physics Letters **93**, 082508 (2008). [p. 13]

[69] Mavropoulos P., Papanikolaou N. & Dederichs P. H. *Complex Band Structure and Tunneling through Ferromagnet/ Insulator /Ferromagnet Junctions.* Physical Review Letters **85**, 1088–1091 (2000). [p. 13]

[70] Mathon J. & Umerski A. *Theory of tunneling magnetoresistance in a junction with a nonmagnetic metallic interlayer.* Physical Review B **60**, 1117–1121 (1999). [p. 13]

[71] Butler W. H., Zhang X.-G., Schulthess T. C. & MacLaren J. M. *Spin-dependent tunneling conductance of Fe/MgO/Fe sandwiches.* Physical Review B **63**, 054416 (2001). [p. 13]

[72] Mathon J. & Umerski A. *Theory of tunneling magnetoresistance of an epitaxial Fe/MgO/Fe(001) junction.* Physical Review B **63**, 220403 (2001). [p. 13]

[73] Slonczewski J. *Current-driven excitation of magnetic multilayers.* Journal of Magnetism and Magnetic Materials **159**, L1–L7 (1996). [pp. 14, 43]

[74] Berger L. *Emission of spin waves by a magnetic multilayer traversed by a current.* Physical Review B **54**, 9353–9358 (1996). [p. 14]

[75] Apalkov D. M. & Visscher P. B. *Spin-torque switching: Fokker-Planck rate calculation.* Physical Review B **72**, 180405 (2005). [p. 14]

[76] Oh S.-C., Park S.-Y., Manchon A., Chshiev M., Han J.-H., Lee H.-W., Lee J.-E., Nam K.-T., Jo Y., Kong Y.-C., Dieny B. & Lee K.-J. *Bias-voltage dependence of perpendicular spin-transfer torque in asymmetric MgO-based magnetic tunnel junctions.* Nature Physics **5**, 898–902 (2009). [p. 14]

[77] Timopheev A. A., Sousa R., Chshiev M., Buda-Prejbeanu L. D. & Dieny B. *Respective influence of in-plane and out-of-plane spin-transfer torques in magnetization switching of perpendicular magnetic tunnel junctions.* Physical Review B **92**, 104430 (2015). [p. 14]

[78] Li Z., Zhang S., Diao Z., Ding Y., Tang X., Apalkov D. M., Yang Z., Kawabata K. & Huai Y. *Perpendicular Spin Torques in Magnetic Tunnel Junctions.* Physical Review Letters **100**, 246602 (2008). [p. 14]

[79] Huai Y. *Spin-Transfer Torque MRAM (STT-MRAM): Challenges and Prospects* 8 . [p. 14]

[80] Chshiev M., Manchon A., Kalitsov A., Ryzhanova N., Vedyayev A., Strelkov N., Butler W. H. & Dieny B. *Analytical description of ballistic spin currents and torques in magnetic tunnel junctions.* Physical Review B **92**, 104422 (2015). [p. 14]

[81] Tsoi M., Jansen A. G. M., Bass J., Chiang W.-C., Seck M., Tsoi V. & Wyder P. *Excitation of a Magnetic Multilayer by an Electric Current.* Physical Review Letters **80**, 4281–4284 (1998). [p. 14]

[82] Katine J. A., Albert F. J., Buhrman R. A., Myers E. B. & Ralph D. C. *Current-Driven Magnetization Reversal and Spin-Wave Excitations in Co /Cu /Co Pillars.* Physical Review Letters **84**, 3149–3152 (2000). [p. 15]

[83] Huai Y., Albert F., Nguyen P., Pakala M. & Valet T. *Observation of spin-transfer switching in deep submicron-sized and low-resistance magnetic tunnel junctions.* Applied Physics Letters **84**, 3118–3120 (2004). [p. 15]

[84] Diao Z., Apalkov D., Pakala M., Ding Y., Panchula A. & Huai Y. *Spin transfer switching and spin polarization in magnetic tunnel junctions with MgO and AlOx barriers.* Applied Physics Letters **87**, 232502 (2005). [p. 15]

[85] Kubota H., Fukushima A., Ootani Y., Yuasa S., Ando K., Maehara H., Tsunekawa K., Djayaprawira D. D., Watanabe N. & Suzuki Y. *Evaluation of Spin-Transfer Switching in CoFeB/MgO/CoFeB Magnetic Tunnel Junctions.* Japanese Journal of Applied Physics **44**, L1237 (2005). [p. 15]

[86] Hayakawa J., Ikeda S., Lee Y. M., Sasaki R., Meguro T., Matsukura F., Takahashi H. & Ohno H. *Current-Driven Magnetization Switching in CoFeB/MgO/CoFeB Magnetic Tunnel Junctions.* Japanese Journal of Applied Physics **44**, L1267 (2005). [p. 15]

[87] Landau L. & Lifshits E. *On the theory of the dispersion of magnetic permeability in ferromagnetic bodies* **53**, 9 (1935). [p. 15]

[88] Gilbert T. *A phenomenological theory of damping in ferromagnetic materials.* IEEE Transactions on Magnetics **40**, 3443–3449 (2004). [p. 15]

[89] Azzawi S., Hindmarch A. T. & Atkinson D. *Magnetic damping phenomena in ferromagnetic thin-films and multilayers.* Journal of Physics D: Applied Physics **50**, 473001 (2017). [p. 15]

[90] Apalkov D., Dieny B. & Slaughter J. M. *Magnetoresistive Random Access Memory.* Proceedings of the IEEE **104**, 1796–1830 (2016). [p. 17]

[91] Tehrani S., Slaughter J., Deherrera M., Engel B., Rizzo N., Salter J., Durlam M., Dave R., Janesky J., Butcher B., Smith K. & Grynkewich G. *Magnetoresistive random access memory using magnetic tunnel junctions.* Proceedings of the IEEE **91**, 703–714 (2003). [p. 17]

[92] Savtchenko L., Korkin A., Engel B., Rizzo N., Deherrera M. & Janesky J. *Method of writing to scalable magnetoresistance random access memory element* (2003). [p. 17]

[93] *4-Mbit Device Is First Commercially Available MRAM* (2006). [p. 17]

[94] Andre T., Nahas J., Subramanian C., Garni B., Lin H., Omair A. & Martino W. *A 4-Mb 0.18-/spl mu/m 1T1MTJ toggle MRAM with balanced three input sensing scheme and locally mirrored unidirectional write drivers.* IEEE Journal of Solid-State Circuits **40**, 301–309 (2005). [p. 17]

[95] Engel B., Akerman J., Butcher B., Dave R., DeHerrera M., Durlam M., Grynkewich G., Janesky J., Pietambaram S., Rizzo N., Slaughter J., Smith K., Sun J. & Tehrani S. *A 4-Mb toggle MRAM based on a novel bit and switching method.* IEEE Transactions on Magnetics **41**, 132–136 (2005). [p. 17]

[96] Sousa R. C. & Prejbeanu I. L. *Non-volatile magnetic random access memories (MRAM).* Comptes Rendus Physique **6**, 1013–1021 (2005). [p. 18]

[97] Prejbeanu I., Kula W., Ounadjela K., Sousa R., Redon O., Dieny B. & Nozieres J.-P. *Thermally assisted switching in exchange-biased storage layer magnetic tunnel junctions.* IEEE Transactions on Magnetics **40**, 2625–2627 (2004). [p. 18]

[98] Worledge D. C., Hu G., Abraham D. W., Sun J. Z., Trouilloud P. L., Nowak J., Brown S., Gaidis M. C., O'Sullivan E. J. & Robertazzi R. P. *Spin torque switching of perpendicular Ta|CoFeB|MgO-based magnetic tunnel junctions.* Applied Physics Letters **98**, 022501 (2011). [p. 18]

[99] Rizzo N. D., Houssameddine D., Janesky J., Whig R., Mancoff F. B., Schneider M. L., DeHerrera M., Sun J. J., Nagel K., Deshpande S., Chia H.-J., Alam S. M., Andre T., Aggarwal S. & Slaughter J. M. *A Fully Functional 64 Mb DDR3 ST-MRAM Built on 90 nm CMOS Technology.* IEEE Transactions on Magnetics **49**, 4441–4446 (2013). [p. 18]

[100] Jan G., Thomas L., Le S., Lee Y.-J., Liu H., Zhu J., Tong R.-Y., Pi K., Wang Y.-J., Shen D., He R., Haq J., Teng J., Lam V., Huang K., Zhong T., Torng T. & Wang P.-K. *Demonstration of fully functional 8Mb perpendicular STT-MRAM chips with sub-5ns writing for non-volatile embedded memories.* In *2014 Symposium on VLSI Technology (VLSI-Technology): Digest of Technical Papers*, 1–2 (2014). [p. 18]

[101] Thomas L., Jan G., Zhu J., Liu H., Lee Y.-J., Le S., Tong R.-Y., Pi K., Wang Y.-J., Shen D., He R., Haq J., Teng J., Lam V., Huang K., Zhong T., Torng T. & Wang P.-K. *Perpendicular spin transfer torque magnetic random access memories with high spin torque efficiency and thermal stability for embedded applications (invited).* Journal of Applied Physics **115**, 172615 (2014). [p. 18]

[102] *Samsung reaffirms 2018 target for STT-MRAM mass production — MRAM-Info.* [p. 18]

[103] Patrigeon G., Benoit P., Torres L., Senni S., Prenat G. & Di Pendina G. *Design and Evaluation of a 28-nm FD-SOI STT-MRAM for Ultra-Low Power Microcontrollers.* IEEE Access **7**, 58085–58093 (2019). [p. 18]

[104] Lee K., Bak J. H., Kim Y. J., Kim C. K., Antonyan A., Chang D. H., Hwang S. H., Lee G. W., Ji N. Y., Kim W. J., Lee J. H., Bae B. J., Park J. H., Kim I. H., Seo B. Y., Han S. H., Ji Y., Jung H. T., Park S. O., Kwon O. I., Kye J. W., Kim Y. D., Pae S. W., Song Y. J., Jeong G. T., Hwang K. H., Koh G. H., Kang H. K. & Jung E. S. *1Gbit High Density Embedded STT-MRAM in 28nm FDSOI Technology.* In *2019 IEEE International Electron Devices Meeting (IEDM)*, 2.2.1–2.2.4 (2019). [p. 18]

[105] Aggarwal S., Almasi H., DeHerrera M., Hughes B., Ikegawa S., Janesky J., Lee H. K., Lu H., Mancoff F. B., Nagel K., Shimon G., Sun J. J., Andre T. & Alam S. M. *2.1 Demonstration of a Reliable 1 Gb Standalone Spin-Transfer Torque MRAM For Industrial Applications* 4 . [p. 18]

[106] Honjo H., Nguyen T. V. A., Watanabe T., Nasuno T., Zhang C., Tanigawa T., Miura S., Inoue H., Niwa M., Yoshiduka T., Noguchi Y., Yasuhira M., Tamakoshi A., Natsui M., Ma Y., Koike H., Takahashi Y., Furuya K., Shen H., Fukami S., Sato H., Ikeda S., Hanyu T., Ohno H. & Endoh T. *28.5 First Demonstration of Field-Free SOT-MRAM with 0.35 ns Write Speed and 70 Thermal Stability under 400°C Thermal Tolerance by Canted SOT Structure and its Advanced Patterning/SOT Channel Technology* 4 . [p. 19]

[107] Peng S. Z., Lu J. Q., Li W. X., Wang L. Z., Zhang H., Li X., Wang K. L. & Zhao W. S. *Field-Free Switching of Perpendicular Magnetization through Voltage-Gated Spin-Orbit Torque* 4 . [p. 19]

[108] Kevin Garello, Yasin F., Couet S. & Souriau L. *SOT-MRAM 300mm integration for low power and ultrafast embedded memories* (2018). [p. 19]

[109] Strukov D. B., Snider G. S., Stewart D. R. & Williams R. S. *The missing memristor found.* Nature **453**, 80–83 (2008). [p. 20]

[110] Locatelli N., Cros V. & Grollier J. *Spin-torque building blocks.* Nature Materials **13**, 11–20 (2014). [p. 20]

[111] Locatelli N., Mizrahi A., Accioly A., Querlioz D., Kim J., Cros V. & Grollier J. *Spin torque nanodevices for bio-inspired computing.* In *2014 14th International Workshop on Cellular Nanoscale Networks and Their Applications (CNNA)*, 1–2 (2014). [p. 20]

[112] Romera M., Talatchian P., Tsunegi S., Abreu Araujo F., Cros V., Bortolotti P., Trastoy J., Yakushiji K., Fukushima A., Kubota H., Yuasa S., Ernoult M., Vodenicarevic D., Hirtzlin T., Locatelli N., Querlioz D. & Grollier J. *Vowel recognition with four coupled spin-torque nano-oscillators.* Nature **563**, 230–234 (2018). [p. 20]

[113] Torrejon J., Riou M., Araujo F. A., Tsunegi S., Khalsa G., Querlioz D., Bortolotti P., Cros V., Yakushiji K., Fukushima A., Kubota H., Yuasa S., Stiles M. D. & Grollier J. *Neuromorphic computing with nanoscale spintronic oscillators.* Nature **547**, 428–431 (2017). [p. 20]

[114] Nafea S. F., Dessouki A. A. S., El-Rabaie S., Elnaghi B. E., Ismail Y. & Mostafa H. *An accurate model of domain-wall-based spintronic memristor.* Integration **65**, 149–162 (2019). [p. 20]

[115] Lequeux S., Sampaio J., Cros V., Yakushiji K., Fukushima A., Matsumoto R., Kubota H., Yuasa S. & Grollier J. *A magnetic synapse: Multilevel spin-torque memristor with perpendicular anisotropy.* Scientific Reports **6**, 31510 (2016). [pp. 20, 80]

[116] Kim Y.-U., Kwon J., Hwang H.-K., Purnama I. & You C.-Y. *Multi-level anomalous Hall resistance in a single Hall cross for the applications of neuromorphic device.* Scientific Reports **10**, 1285 (2020). [p. 20]

[117] Azam M. A., Bhattacharya D., Querlioz D., Ross C. A. & Atulasimha J. *Voltage control of domain walls in magnetic nanowires for energy-efficient neuromorphic devices.* Nanotechnology **31**, 145201 (2020). [p. 21]

[118] Cui C., Akinola O. G., Hassan N., Bennett C., Marinella M., Friedman J. & Incorvia J. A. C. *Maximized Lateral Inhibition in Paired Magnetic Domain Wall Racetracks for Neuromorphic Computing.* Nanotechnology (2020). [p. 21]

[119] Shibata T., Shinohara T., Ashida T., Ohta M., Ito K., Yamada S., Terasaki Y. & Sasaki T. *Linear and symmetric conductance response of magnetic domain wall type spin-memristor for analog neuromorphic computing.* Applied Physics Express **13**, 043004 (2020). [p. 21]

[120] Chanthbouala A., Garcia V., Cherifi R. O., Bouzehouane K., Fusil S., Moya X., Xavier S., Yamada H., Deranlot C., Mathur N. D., Bibes M., Barthélémy A. & Grollier J. *A ferroelectric memristor.* Nature Materials **11**, 860–864 (2012). [p. 21]

[121] Yamada H., Garcia V., Fusil S., Boyn S., Marinova M., Gloter A., Xavier S., Grollier J., Jacquet E., Carrétéro C., Deranlot C., Bibes M. & Barthélémy A. *Giant Electroresistance of Super-tetragonal $BiFeO_3$ -Based Ferroelectric Tunnel Junctions.* ACS Nano **7**, 5385–5390 (2013). [p. 21]

[122] Boyn S., Girod S., Garcia V., Fusil S., Xavier S., Deranlot C., Yamada H., Carrétéro C., Jacquet E., Bibes M., Barthélémy A. & Grollier J. *High-performance ferroelectric memory based on fully patterned tunnel junctions.* Applied Physics Letters **104**, 052909 (2014). [p. 21]

[123] Boyn S., Grollier J., Lecerf G., Xu B., Locatelli N., Fusil S., Girod S., Carrétéro C., Garcia K., Xavier S., Tomas J., Bellaiche L., Bibes M., Barthélémy A., Saïghi S. & Garcia V. *Learning through ferroelectric domain dynamics in solid-state synapses.* Nature Communications **8**, 14736 (2017). [p. 21]

[124] Fukami S., Zhang C., DuttaGupta S., Kurenkov A. & Ohno H. *Magnetization switching by spin–orbit torque in an antiferromagnet–ferromagnet bilayer system.* Nature Materials **15**, 535–541 (2016). [pp. 21, 22]

[125] Kurenkov A., DuttaGupta S., Zhang C., Fukami S., Horio Y. & Ohno H. *Artificial Neuron and Synapse Realized in an Antiferromagnet/Ferromagnet Heterostructure Using Dynamics of Spin–Orbit Torque Switching.* Advanced Materials **31**, 1900636 (2019). [pp. 21, 22]

[126] Jo S. H., Chang T., Ebong I., Bhadviya B. B., Mazumder P. & Lu W. *Nanoscale Memristor Device as Synapse in Neuromorphic Systems.* Nano Letters **10**, 1297–1301 (2010). [p. 21]

[127] Zhang Y., Cai W., Kang W., Yang J., Deng E., Zhang Y.-G., Zhao W. & Ravelosona D. *Demonstration of Multi-State Memory Device Combining Resistive and Magnetic Switching Behaviors.* IEEE Electron Device Letters **39**, 684–687 (2018). [pp. 21, 22]

[128] Krzysteczko P., Münchenberger J., Schäfers M., Reiss G. & Thomas A. *The Memristive Magnetic Tunnel Junction as a Nanoscopic Synapse-Neuron System.* Advanced Materials **24**, 762–766 (2012). [p. 22]

[129] Raymenants E., Vaysset A., Wan D., Manfrini M., Zografos O., Bultynck O., Doevenspeck J., Heyns M., Radu I. P. & Devolder T. *Chain of magnetic tunnel junctions as a spintronic memristor.* Journal of Applied Physics **124**, 152116 (2018). [pp. 22, 23]

[130] Ostwal V., Zand R., DeMara R. & Appenzeller J. *A Novel Compound Synapse Using Probabilistic Spin–Orbit-Torque Switching for MTJ-Based Deep Neural Networks.* IEEE Journal on Exploratory Solid-State Computational Devices and Circuits **5**, 182–187 (2019). [p. 22]

[131] Song K. M., Jeong J.-S., Pan B., Zhang X., Xia J., Cha S., Park T.-E., Kim K., Finizio S., Raabe J., Chang J., Zhou Y., Zhao W., Kang W., Ju H. & Woo S. *Skyrmion-based artificial synapses for neuromorphic computing.* Nature Electronics **3**, 148–155 (2020). [p. 23]

[132] Luo S., Xu N., Guo Z., Zhang Y., Hong J. & You L. *Voltage-Controlled Skyrmion Memristor for Energy-Efficient Synapse Applications.* IEEE Electron Device Letters **40**, 635–638 (2019). [p. 23]

[133] Yu Z., Shen M., Zeng Z., Liang S., Liu Y., Chen M., Zhang Z., Lu Z., You L., Yang X., Zhang Y. & Xiong R. *Voltage-controlled skyrmion-based nanodevices for neuromorphic computing using a synthetic antiferromagnet.* Nanoscale Advances **2**, 1309–1317 (2020). [p. 23]

[134] Slonczewski J. C. *Conductance and exchange coupling of two ferromagnets separated by a tunneling barrier.* Physical Review B **39**, 6995–7002 (1989). [p. 24]

[135] Jaffrès H., Lacour D., Nguyen Van Dau F., Briatico J., Petroff F. & Vaurès A. *Angular dependence of the tunnel magnetoresistance in transition-metal-based junctions.* Physical Review B **64**, 064427 (2001). [pp. 24, 59]

[136] Ebels U., Houssameddine D., Firastrau I., Gusakova D., Thirion C., Dieny B. & Buda-Prejbeanu L. D. *Macrospin description of the perpendicular polarizer-planar free-layer spin-torque oscillator.* Physical Review B **78**, 024436 (2008). [pp. 24, 43, 44, 45]

[137] Vincent A. F., Locatelli N., Klein J.-O., Zhao W. S., Galdin-Retailleau S. & Querlioz D. *Analytical Macrospin Modeling of the Stochastic Switching Time of Spin-Transfer Torque Devices.* IEEE Transactions on Electron Devices **62**, 164–170 (2015). [p. 25]

[138] Parker M. *The Kerr magneto-optic effect (1876–1976).* Physica B+C **86-88**, 1171–1176 (1977). [p. 29]

[139] Nguyen Van Dau F., Schuhl A., Childress J. & Sussiau M. *Magnetic sensors for nanotesla detection using planar Hall effect.* Sensors and Actuators A: Physical **53**, 256–260 (1996). [pp. 31, 52]

[140] Zuo C., Chen Q. & Asundi A. *Transport of intensity equation: A new approach to phase and light field.* In *Holography, Diffractive Optics, and Applications VI*, vol. 9271, 92710H (International Society for Optics and Photonics, 2014). [pp. 32, 54]

[141] *ACCUFLO® Technical Data Sheets.* [p. 34]

[142] *PTA — Upstream Technological Platform.* [p. 34]

[143] Buda-Prejbeanu L. D. *Micromagnetism Applied to Magnetic Nanostructures.* In *Introduction to Magnetic Random-Access Memory*, 55–78 (John Wiley & Sons, Ltd, 2016). [p. 40]

[144] Kittel C. & Galt J. K. *Ferromagnetic Domain Theory.* In Seitz F. & Turnbull D. (eds.) *Solid State Physics*, vol. 3, 437–564 (Academic Press, 1956). [p. 40]

[145] Malozemoff A. P. & Slonczewski J. C. *Magnetic Domain Walls in Bubble Materials: Advances in Materials and Device Research* (Academic Press, 2016). [p. 40]

[146] Baltensperger W. & Helman J. *Dry friction in micromagnetics.* IEEE Transactions on Magnetics **27**, 4772–4774 (1991). [p. 40]

[147] Hołyst J., Baltensperger W. & Helman J. *Influence of dry magnetic friction on the ferromagnetic resonance.* Solid State Communications **82**, 763–765 (1992). [p. 40]

[148] Visintin A. *Modified Landau-Lifshitz equation for ferromagnetism.* Physica B: Condensed Matter **233**, 365–369 (1997). [p. 40]

[149] Magiera M. P., Angst S., Hucht A. & Wolf D. E. *Magnetic friction: From Stokes to Coulomb behavior.* Physical Review B **84**, 212301 (2011). [p. 40]

[150] Consolo G., Currò C., Martinez E. & Valenti G. *Mathematical modeling and numerical simulation of domain wall motion in magnetic nanostrips with crystallographic defects.* Applied Mathematical Modelling **36**, 4876–4886 (2012). [p. 40]

[151] Redon O., Dieny B. & Rodmacq B. *Magnetic spin polarization and magnetization rotation device with memory and writing process, using such a device* (2003). [p. 43]

[152] Kent A., Gonzalez G. E. & Ozyilmaz B. *High speed low power magnetic devices based current induced spin-momentum transfer* (2005). [p. 43]

[153] Slonczewski J. C. *Electronic device using magnetic components* (1997). [p. 43]

[154] Papusoi C., Delaët B., Rodmacq B., Houssameddine D., Michel J.-P., Ebels U., Sousa R. C., Buda-Prejbeanu L. & Dieny B. *100 ps precessional spin-transfer switching of a planar magnetic random access memory cell with perpendicular spin polarizer.* Applied Physics Letters **95**, 072506 (2009). [p. 43]

[155] Marins de Castro M., Sousa R. C., Bandiera S., Ducruet C., Chavent A., Auffret S., Papusoi C., Prejbeanu I. L., Portemont C., Vila L., Ebels U., Rodmacq B. & Dieny B. *Precessional spin-transfer switching in a magnetic tunnel junction with a synthetic antiferromagnetic perpendicular polarizer.* Journal of Applied Physics **111**, 07C912 (2012). [p. 43]

[156] Houssameddine D. *Dynamique de l'aimantation de nano-oscillateurs micro-ondes à transfert de spin* 194 (2009). [p. 49]

[157] Dieny B., Barbara B., Fillion G., Maeder M. & Michelutti B. *Hysteresis loop and torque experiments on a random anisotropy system.* Journal de Physique **48**, 1741–1749 (1987). [p. 51]

[158] Baltensperger W. & Helman J. S. *A model that gives rise to effective dry friction in micromagnetics.* Journal of Applied Physics **73**, 6516–6518 (1993). [p. 51]

[159] Baltz V., Rodmacq B., Zarefy A., Lechevallier L. & Dieny B. *Bimodal distribution of blocking temperature in exchange-biased ferromagnetic/antiferromagnetic bilayers.* Physical Review B **81**, 052404 (2010). [p. 51]

[160] Berkowitz A. E. & Takano K. *Exchange anisotropy * a review.* Journal of Magnetism and Magnetic Materials 19 (1999). [p. 51]

[161] Nogués J. & Schuller I. K. *Exchange bias.* Journal of Magnetism and Magnetic Materials **192**, 203–232 (1999). [p. 51]

[162] Ali M., Marrows C. H., Al-Jawad M., Hickey B. J., Misra A., Nowak U. & Usadel K. D. *Antiferromagnetic layer thickness dependence of the IrMn/Co exchange-bias system.* Physical Review B **68**, 214420 (2003). [p. 51]

[163] Baltz V. & Dieny B. *Influence of Pt as Mn diffusion barrier on the distribution of blocking temperature in Co/(Pt)/IrMn exchange biased layers.* Journal of Applied Physics **109**, 066102 (2011). [p. 53]

[164] Min H., McMichael R. D., Donahue M. J., Miltat J. & Stiles M. D. *Effects of Disorder and Internal Dynamics on Vortex Wall Propagation.* Physical Review Letters **104**, 217201 (2010). [p. 55]

[165] Chatterjee J. *Engineering of magnetic tunnel junction stacks for improved STT-MRAM performance and development of novel and cost-effective nano-patterning techniques* 180 (2018). [p. 56]

[166] Delille F., Manchon A., Strelkov N., Dieny B., Li M., Liu Y., Wang P. & Favre-Nicolin E. *Thermal variation of current perpendicular-to-plane giant magnetoresistance in laminated and nonlaminated spin valves.* Journal of Applied Physics **100**, 013912 (2006). [p. 57]

[167] Deac A., Lee K. J., Liu Y., Redon O., Li M., Wang P., Nozières J. P. & Dieny B. *Current-induced magnetization switching in exchange-biased spin valves for current-perpendicular-to-plane giant magnetoresistance heads.* Physical Review B **73**, 064414 (2006). [p. 57]

[168] Xu F., Liao Z., Huang Q., Phuoc N. N., Ong C. K. & Li S. *Influence of Thickness on Magnetic Properties and Microwave Characteristics of NiFe/IrMn/NiFe Trilayers.* IEEE Transactions on Magnetics **47**, 3486–3489 (2011). [p. 60]

[169] McCord J. *Magnetization Dynamics of Coupled Ferromagnetic-Antiferromagnetic Thin Films.* In Haug R. (ed.) *Advances in Solid State Physics*, vol. 48, 157–170 (Springer Berlin Heidelberg, Berlin, Heidelberg, 2009). [p. 60]

[170] Spenato D., Pogossian S. P., Dekadjevi D. T. & Youssef J. B. *Study of dynamic properties and magnetic anisotropies of NiFe/MnPt in the critical thickness range.* Journal of Physics D: Applied Physics **40**, 3306–3313 (2007). [p. 60]

[171] Lombard L., Gapihan E., Sousa R. C., Dahmane Y., Conraux Y., Portemont C., Ducruet C., Papusoi C., Prejbeanu I. L., Nozières J. P., Dieny B. & Schuhl A. *IrMn and FeMn blocking temperature dependence on heating pulse width.* Journal of Applied Physics **107**, 09D728 (2010). [p. 64]

[172] Prejbeanu I. L., Kerekes M., Sousa R. C., Sibuet H., Redon O., Dieny B. & Nozières J. P. *Thermally assisted MRAM.* Journal of Physics: Condensed Matter **19**, 165218 (2007). [pp. 64, 83]

[173] Sun J. Z., Brown S. L., Chen W., Delenia E. A., Gaidis M. C., Harms J., Hu G., Jiang X., Kilaru R., Kula W., Lauer G., Liu L. Q., Murthy S., Nowak J., O'Sullivan E. J., Parkin S. S. P., Robertazzi R. P., Rice P. M., Sandhu G., Topuria T. & Worledge D. C. *Spin-torque switching efficiency in CoFeB-MgO based tunnel junctions.* Physical Review B **88**, 104426 (2013). [p. 65]

[174] Daniel E. D., Mee C. D. & Clark M. H. *Magnetic Recording the First 100 Years* (IEEE, New York, 2009). [p. 73]

[175] Moser A., Takano K., Margulies D. T., Albrecht M., Sonobe Y., Ikeda Y., Sun S. & Fullerton E. E. *Magnetic recording: Advancing into the future.* Journal of Physics D: Applied Physics **35**, R157–R167 (2002). [p. 73]

[176] Doerner M., Bian X., Madison M., Tang K., Peng Q., Polcyn A., Arnoldussen T., Toney M., Mirzamaani M., Takano K., Fullerton E., Margulies D., Schabes M., Rubin K., Pinarbasi M., Yuan S., Parker M. & Weller D. *Demonstration of 35 Gbits/in/sup 2/ in media on glass substrates.* IEEE Transactions on Magnetics **37**, 1052–1058 (2001). [p. 73]

[177] Takano H., Nishida Y., Kuroda A., Sawaguchi H., Hosoe Y., Kawabe T., Aoi H., Muraoka H., Nakamura Y. & Ouchi K. *Realization of 52.5Gb/in2 perpendicular recording.* Journal of Magnetism and Magnetic Materials **235**, 241–244 (2001). [p. 73]

[178] Fullerton E. E., Margulies D. T., Schabes M. E., Carey M., Gurney B., Moser A., Best M., Zeltzer G., Rubin K., Rosen H. & Doerner M. *Antiferromagnetically coupled magnetic media layers for thermally stable high-density recording.* Applied Physics Letters **77**, 3806–3808 (2000). [p. 73]

[179] Abarra E. N., Inomata A., Sato H., Okamoto I. & Mizoshita Y. *Longitudinal magnetic recording media with thermal stabilization layers.* Applied Physics Letters **77**, 2581–2583 (2000). [p. 73]

[180] Carey M. J., Fullerton E. E., Gurney B. A., Rosen H. J. & Schabes M. E. *Magnetic recording media with antiferromagnetically coupled ferromagnetic films as the recording layer* (2001). [p. 73]

[181] Piramanayagam S. N. *Perpendicular recording media for hard disk drives.* Journal of Applied Physics **102**, 011301 (2007). [p. 73]

[182] A. Thompson D. *THE ROLE OF PERPENDICULAR RECORDING IN THE FUTURE OF HARD DISK STORAGE.* Journal of the Magnetics Society of Japan **21**, S2_9–15 (1997). [p. 73]

[183] Oshiki M. *Review of perpendicular magnetic recording research at Fujitsu.* Journal of Magnetism and Magnetic Materials **324**, 351–354 (2012). [p. 73]

[184] Ruigrok J. J. M., Coehoorn R., Cumpson S. R. & Kesteren H. W. *Disk recording beyond 100 Gb/in.2: Hybrid recording? (invited).* Journal of Applied Physics **87**, 5398–5403 (2000). [p. 73]

[185] Alex M., Tselikov A., McDaniel T., Deeman N., Valet T. & Chen D. *Characteristics of thermally assisted magnetic recording.* IEEE Transactions on Magnetics **37**, 1244–1249 (2001). [p. 73]

[186] Sun n., Murray n., Weller n., Folks n. & Moser n. *Monodisperse FePt nanoparticles and ferromagnetic FePt nanocrystal superlattices.* Science (New York, N.Y.) **287**, 1989–1992 (2000). [p. 73]

[187] Yu M., Liu Y., Moser A., Weller D. & Sellmyer D. J. *Nanocomposite CoPt:C films for extremely high-density recording.* Applied Physics Letters **75**, 3992–3994 (1999). [p. 73]

[188] Weller D., Parker G., Mosendz O., Champion E., Stipe B., Wang X., Klemmer T., Ju G. & Ajan A. *A HAMR Media Technology Roadmap to an Areal Density of 4 Tb/in2.* IEEE Transactions on Magnetics **50**, 1–8 (2014). [p. 73]

[189] Andreenko A. S., Berezovets V. A., Granovskii A. B., Zolotukhin I. V., Inoue M., Kalinin Y. E., Sitnikov A. V., Stognei O. V. & Palevski T. *Inverse magnetoresistance in (FeCoB)-(Al2O3) magnetic granular composites.* Physics of the Solid State **45**, 1519–1522 (2003). [p. 74]

[190] Lesnik N. A., Gontarz R., Kakazei G. N., Kravets A. F., Wigen P. E. & Dubowik J. *Magnetic structure in FeCo–Al2O3 granular films studied by the ferromagnetic resonance.* physica status solidi (a) **196**, 157–160 (2003). [p. 74]

[191] Rylkov V. V., Sitnikov A. V., Nikolaev S. N., Demin V. A., Taldenkov A. N., Presnyakov M. Y., Emelyanov A. V., Vasiliev A. L., Kalinin Y. E., Bugaev A. S., Tugushev V. V. & Granovsky A. B. *Properties of granular (CoFeB)x(Al2O3)100-x and (CoFeB)x(LiNbO3)100-x nanocomposites: Manifestation of superferromagnetic ordering effects.* Journal of Magnetism and Magnetic Materials **459**, 197–201 (2018). [p. 74]

[192] Sato H., Chureemart P., Matsukura F., Chantrell R. W., Ohno H. & Evans R. F. L. *Temperature-dependent properties of CoFeB/MgO thin films: Experiments versus simulations.* Physical Review B **98**, 214428 (2018). [pp. 81, 82]

[193] Evans R. F. L., Atxitia U. & Chantrell R. W. *Quantitative simulation of temperature-dependent magnetization dynamics and equilibrium properties of elemental ferromagnets.* Physical Review B **91**, 144425 (2015). [pp. 81, 82]

[194] Callen H. B. & Callen E. *The present status of the temperature dependence of magnetocrystalline anisotropy, and the l(l+1)2 power law.* Journal of Physics and Chemistry of Solids **27**, 1271–1285 (1966). [p. 81]

[195] Kou X., Schmalhorst J., Thomas A. & Reiss G. *Temperature dependence of the resistance of magnetic tunnel junctions with MgO barrier.* Applied Physics Letters **88**, 212115 (2006). [pp. 81, 82]

Abstract

In the context of a technological era in which the amount of data is exponentially increasing, the development of brain-inspired softwares allows a fast and smart management of information. However, the massive parallelization of neurons interconnected through synapses, emulated by these approaches, leads to a drastic power consumption when runned on conventional computers. From this, it arises the need of dedicated hardwares that, contrarily to the Von Neumann architecture, interconnect at large scale processing units and memory units as, respectively, neurons and synapses. For this reason, the realization of nano-sized devices able to mimic the functionalities of neurons and synapses represents the main challenge for the integration of large scale neuromorphic chips. The purpose of this work is to realize memristive devices, i.e. non-volatile multilevel memories that play the role of synapses, exploiting the advantages of the MRAM technology. In this thesis two main concepts have been proposed, realized and characterized. The first device investigated in this thesis is based on the conductance variation of an in-plane magnetized magnetic tunnel junction as function of the relative direction of the magnetizations of the storage and reference layers. Being able to stabilize intermediate resistance states between the minimum and maximum resistance values of the magnetic tunnel junction requires the realization of a medium able to stabilize its magnetization along different in-plane directions. We obtain such isotropic properties using a ferromagnet/antiferromagnet/ferromagnet structure in which the antiferromagnetic layer thickness is chosen low enough to not provide any exchange bias but rather enhanced coercivity. We integrated this composite layer in an in-plane magnetic tunnel junction and, after a nano-patterning process, we retrieved the same property of isotropic coercivity. The device is able to monotonously increase or decrease its resistance in response to positive or negative voltage pulses (in ns range) because of the spin transfer torque coming from an additional out-of-plane polarizer. We demonstrate the stabilization of at least 21 resistance levels in devices of 100nm of diameter. We also model the device with a macrospin code implementing the Landau Lifshitz Gilbert equation with an additional dissipative term analog to a dry friction term in the Newton's law. With this, we retrieve all the results obtained experimentally with quite good agreement. The second concept investigated in this work is based on a perpendicularly magnetized tunnel junction whose free layer presents a granular structure similar to the one used for recording media. The realization of such layer led to the realization of grains with a diameter around 3nm and, therefore, paramagnetic at room temperature. Such layer is integrated in magnetic tunnel junctions with diameters between 100nm and 300nm. The electrical measurements performed at 150K demonstrate that a very large number of resistance states can be achieved with a gradual field-driven switching of such grains. Moreover, the use of voltage pulses confirms that the spin transfer effect can be exploited for the probabilistic reversal of the grains magnetization.

Résumé

Dans le contexte d'une ère technologique où la quantité de données augmente de façon exponentielle, le développement de logiciels inspirés du fonctionnement du cerveau permet une gestion rapide et intelligente de l'information. Cependant, la parallélisation massive de neurones interconnectés via des synapses, émulée par ces approches, conduit à une consommation d'énergie drastique lorsqu'ils sont exécutés sur des ordinateurs conventionnels. De là, naît le besoin de matériels dédiés qui, contrairement à l'architecture de Von Neumann, permettent d'interconnecter à grande échelle des unités de traitement et des unités de mémoire représentant respectivement les neurones et les synapses. Pour cette raison, la réalisation de dispositifs de taille nanométrique capables de mimer les fonctionnalités des neurones et des synapses représente le principal défi pour l'intégration de puces neuromorphiques à grande échelle. Le but de ce travail est de réaliser des dispositifs memristifs, c'est-à-dire des mémoires multiniveaux non volatiles qui jouent le rôle de synapses, exploitant les avantages de la technologie MRAM. Deux concepts de memristor spintronique à base de jonctions tunnel magnétiques ont été proposés, réalisés et caractérisés. Le premier concept fonde ses principes de fonctionnement sur la variation de conductance d'une jonction tunnel magnétique aimantée dans le plan, en fonction de la direction relative des aimantations des couches de stockage et de référence. La clé de ce concept repose sur la mise au point d'un matériau magnétique capable de stabiliser son aimantation selon différentes directions dans le plan menant ainsi à une multitude d'états de résistance intermédiaires. On obtient de telles propriétés isotropes en utilisant une structure ferromagnet / antiferromagnet / ferromagnet dans laquelle l'épaisseur de la couche antiferromagnétique est choisie suffisamment faible pour ne pas conduire à l'existence d'une anisotropie d'échange mais plutôt d'une coercivité accrue. Nous avons intégré cette couche composite dans une jonction tunnel magnétique dans le plan et, après un processus de nanostructuration, nous avons conservé la même propriété de coercivité isotrope. Dans une telle jonction tunnel, on peut augmenter ou diminuer de manière monotone la résistance en réponse à des impulsions de tension positives ou négatives (dans la gamme ns) grâce au couple de transfert de spin provenant d'un polariseur suuplémentaire aimanté hors plan. Nous démontrons la stabilisation d'au moins 21 niveaux de résistance dans des jonctions tunnel de taille latérale de 100nm. Nous modélisons également le fonctionnement du dispositif avec un code macrospin implémentant l'équation de Landau Lifshitz Gilbert avec un terme dissipatif supplémentaire analogue à un terme de frottement solide dans la loi de Newton. Par ces simultations, nous interprétons tous les résultats obtenus expérimentalement avec un bon accord. Le deuxième concept étudié dans ce travail est basé sur une jonction tunnel aimantée perpendiculairement dont la couche libre présente une structure granulaire similaire à celle utilisée pour les supports d'enregistrement magnétique. La réalisation d'une telle couche a conduit à la formation de grains d'un diamètre d'environ 3nm et donc paramagnétiques à température ambiante. De telles couches ont été déposées et intégrées dans des jonctions tunnel de taille latérale de 100nm à 300nm. Les mesures électriques effectuées à 150K démontrent qu'un très grand nombre d'états de résistance peut être obtenu avec une commutation graduelle par champ de ces grains. De plus, l'utilisation d'impulsions de tension confirme que l'effet de transfert de spin peut être exploité pour l'inversion probabiliste de l'aimantation des grains.